Observation and Modeling of Biological Colloids with Neutron Scattering Techniques and Monte Carlo Simulations

L.F. van Heijkamp

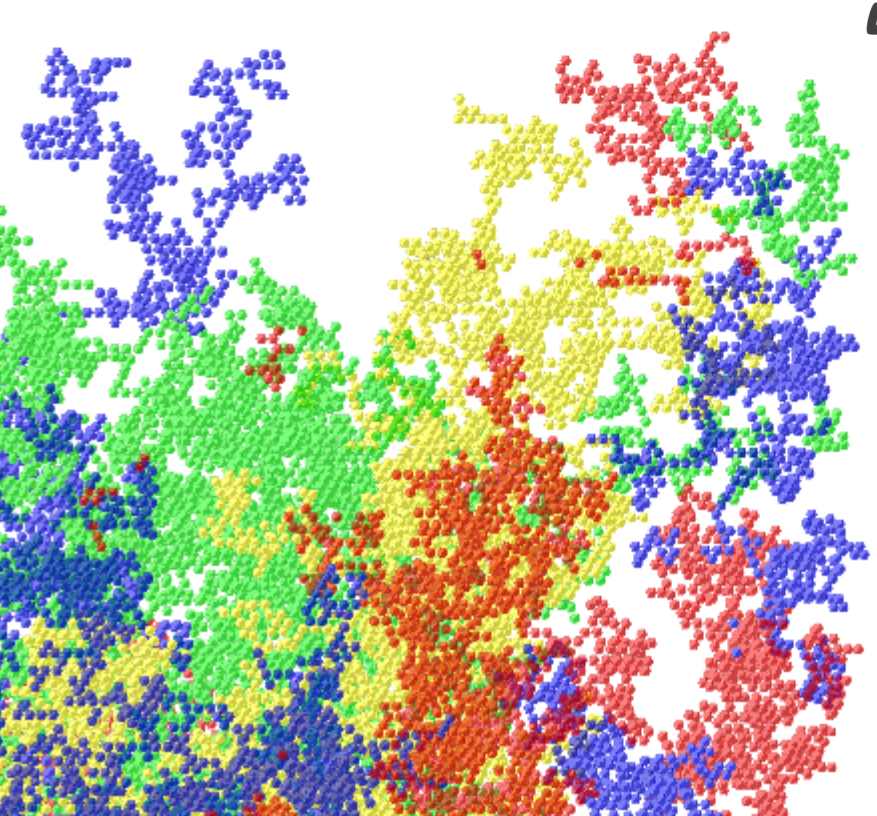

Observation and Modeling of Biological Colloids with Neutron Scattering Techniques and Monte Carlo Simulations

PROEFSCHRIFT

ter verkrijging van de graad van doctor
aan de Technische Universiteit Delft,
op gezag van de Rector Magnificus prof. ir. K.C.A.M. Luyben,
voorzitter van het College voor Promoties,
in het openbaar te verdedigen op donderdag 13 januari 2011 om 12.30 uur

door

Léon Ferdinand van Heijkamp

scheikundig ingenieur

geboren te Amersfoort.

Dit proefschrift is goedgekeurd door de promotor:
Prof. dr. I.M. de Schepper

Toegevoegd promotor:
Dr. ir. W.G. Bouwman

Samenstelling promotiecommissie:

Rector Magnificus	*voorzitter*
Prof. dr. I.M. de Schepper	Technische Universiteit Delft, *promotor*
Dr. ir. W.G. Bouwman	Technische Universiteit Delft, *copromotor*
Prof. dr. C. Pappas	Technische Universiteit Delft
Prof. dr. H.Th. Wolterbeek	Technische Universiteit Delft
Dr. ing. G.J.M. Koper	Technische Universiteit Delft
Prof. dr. W.J. Briels	Universiteit Twente
Dr. R.H. Tromp	NIZO Food Research, Ede

ISBN 978-90-5335-360-8

Keywords: Neutron scattering, SESANS, USANS, simulations, 3D Monte Carlo, colloids, aggregation, DLCA, RLCA, gelation, liposomes, *E. coli*, hollow sphere, correlation length

Ridderprint Offsetdrukkerij BV
Pottenbakkerstraat 17
2984 AX RIDDERKERK
The Netherlands
Telephone: +31 180 463962
Telefax: +31 180 415471
E-mail: info@proefschriftdrukken.nl

Stellingen

Stellingen behorende bij het proefschrift *Observation and Modeling of Biological Colloids with Neutron Scattering Techniques and Monte Carlo simulations* door Léon Ferdinand van Heijkamp, 2010.

I. De geleidelijke destabilisatie van een colloïdale suspensie tijdens gelatie kan gemodelleerd worden als een overgang van reactie-gelimiteerde naar diffusie-gelimiteerde aggregatie van clusters van deeltjes.

II. Er is een duidelijk verschil in fractale dimensionaliteit en typische lengteschalen van caseïnegels wanneer deze langzaam gevormd worden door een geleidelijk toenemende zuurtegraad en wanneer deze gevormd worden door een plotselinge toevoeging van zuur.

III. Het wiskundig vatten van de ruimtelijke verdeling van een structuur in een getal genaamd fractale dimensie, doet geen recht aan de complexe aard hiervan.

IV. De dichtheids-autocorrelatiefunctie van een holle bol is het duidelijkst te onderscheiden van die van een massieve bol van gelijke grootte, als de wanddikte 10% van de diameter bedraagt.

V. De dichtheids-autocorrelatiefunctie van een ui brengt tranen in de ogen.

VI. Nieuwe stralingstechnieken met neutronen en protonen, zoals SESANS en protonradiotherapie, herbergen nog onverkende mogelijkheden voor diagnostiek en behandeling binnen de oncologie.

VII. De grote toename van wetenschappelijke publicaties gedurende de recente decennia wordt steeds meer een obstakel in plaats van een voordeel voor het verwerven van kennis.

VIII. De *Impact Factor* van wetenschappelijke tijdschriften zou logaritmisch herschaald moeten worden en worden hernoemd tot *Relevancy Factor*.

IX. Publieke weerstand tegen nucleaire energie biedt een gezond tegenwicht aan lobbyisten en verhoogt de aandacht voor veiligheidaspecten.

X. Het is beter om het wiel opnieuw uit te vinden, dan klakkeloos aan te nemen dat het vierkant moet zijn.

Deze stellingen worden opponeerbaar en verdedigbaar geacht en zijn als zodanig goedgekeurd door de promotor, prof. dr. I.M. de Schepper.

Propositions

Propositions accompanying the thesis *Observation and Modeling of Biological Colloids with Neutron Scattering Techniques and Monte Carlo simulations* by Léon Ferdinand van Heijkamp, 2010.

I. The gradual destabilization of a colloidal suspension during gelation, can be modeled as a transition from reaction limited to diffusion limited aggregation of clusters of particles.

II. The fractal dimensionality and typical length scales of casein gels are distinctly different when formed slowly through a gradual increase in acidity, as opposed to when formed through a step-wise acidification.

III. Capturing structural information mathematically into the single number called fractal dimension, does not do justice to the complex nature of these structures.

IV. The density auto-correlation function of a hollow sphere is most clearly distinguishable from that of a solid sphere of equal size, when the thickness of the shell is 10% of the diameter.

V. The density auto-correlation function of an onion brings tears to the eyes.

VI. Novel radiation techniques employing neutrons and protons, like SESANS and proton radiotherapy, still have unexplored capabilities for diagnostic and therapeutic cancer treatment.

VII. The large growth in scientific publications over recent decades is starting to become more of an obstacle than an advantage for gaining knowledge.

VIII. The *Impact Factor* of scientific journals should be rescaled logarithmically and renamed *Relevancy Factor*.

IX. Public opposition to nuclear power provides a healthy counterweight to lobbyists and increases the focus on industrial safety.

X. It is better to reinvent the wheel than to unquestioningly agree it should be square.

These propositions are regarded as opposable and defendable, and have been approved by the supervisor, prof. dr. I.M. de Schepper.

Dedicated to my wife Li Mei,
my parents Fred and Margriet
and my sister Caroline.

Contents

1 Introduction **3**
- 1.1 Preface . . . 3
- 1.2 Materials . . . 4
- 1.3 Processes . . . 4
- 1.4 Optics . . . 5
- 1.5 Techniques . . . 7
- 1.6 Thesis overview . . . 8

2 SESANS analysis of liposomes and bacteria **9**
- 2.1 Introduction . . . 10
- 2.2 Biological background . . . 12
  - 2.2.1 Liposomes . . . 12
  - 2.2.2 *Escherichia coli* . . . 12
  - 2.2.3 Contrast of lipid bilayers . . . 13
- 2.3 Experimental . . . 14
  - 2.3.1 Sample preparation . . . 14
  - 2.3.2 The SESANS Technique . . . 15
  - 2.3.3 SESANS Experiments . . . 20
- 2.4 Results . . . 21
  - 2.4.1 Characterization of liposomes with DLS . . . 21
  - 2.4.2 SESANS Results . . . 22
- 2.5 Discussion . . . 25
  - 2.5.1 Measurement results . . . 25
  - 2.5.2 Outlook . . . 26
- 2.6 Conclusions . . . 28

3 Milk gelation studied with neutron scattering and simulations **31**
- 3.1 Introduction . . . 32
- 3.2 Theory . . . 33
  - 3.2.1 The SESANS Measurement Technique . . . 33
  - 3.2.2 The USANS Measurement Technique . . . 40
  - 3.2.3 Simulation Model . . . 43
- 3.3 Experimental . . . 48
  - 3.3.1 Sample preparation . . . 48
  - 3.3.2 SESANS measurements . . . 48

3.3.3 USANS measurements . . . 49
3.3.4 Simulations . . . 49
3.4 Results . . . 50
3.4.1 SESANS Results . . . 50
3.4.2 USANS Results . . . 52
3.4.3 Simulation Results . . . 54
3.5 Discussion . . . 58
3.5.1 Measurements . . . 58
3.5.2 Simulations . . . 61
3.6 Conclusions . . . 62

4 From RLCA to DLCA in 3D Monte Carlo **65**
4.1 Introduction . . . 66
4.2 Simulation . . . 68
4.2.1 Chemistry . . . 68
4.2.2 Model . . . 68
4.2.3 Algorithm . . . 70
4.2.4 Code speed-ups . . . 72
4.2.5 Predictions . . . 74
4.2.6 Approach . . . 75
4.3 Results . . . 76
4.3.1 Aggregation . . . 76
4.3.2 Cluster mass . . . 80
4.3.3 Reactivity . . . 82
4.3.4 Structure . . . 85
4.4 Discussion . . . 89
4.5 Conclusions . . . 91

5 Sample thickness optimization for SESANS **93**
5.1 Introduction . . . 93
5.2 Formalism . . . 95
5.2.1 Relations . . . 95
5.3 Discussion and conclusions . . . 102

A Appendix **103**
A.1 $G(z)$ with a size distribution . . . 103
A.2 Determination of the USANS resolution function . . . 105
A.3 Simulation cycles . . . 106

List of Publications **113**

Summary **115**

Samenvatting **121**

Words of gratitude **127**

Curriculum vitæ **129**

CHAPTER 1

Introduction

1.1 Preface

ARTICLES are the backbone of science. The book before you attempts to sensibly combine three publications dealing with colloidal aggregation, neutron scattering and computer simulations. This rich tapestry of subjects has a motive, which is woven by the theme of spherical particles floating through water. These particles are solid or hollow, sometimes of different sizes and they may stick together over time. Exposing specimens to a beam of neutrons, causes some neutrons to scatter over small angles. These signals are measured with scattering techniques and described using mathematical models. If the structure in a sample changes, the scattered neutron signal changes accordingly. Depending on the length scales involved and the interaction between the substances and neutrons, varying particle composition, such as light–heavy water exchange, or changes in mutual distance between the particles, such as aggregation, are observable. Colloidal aggregation can be modeled using simulation techniques to gain insight into the process and resulting structures.

The colloidal particles under investigation here, are smaller than a micrometer. Their aggregation results in the formation of a gel structure, which can take rather long in microscopic terms. This is a plus point when using relatively weak neutron sources, compared to for example the number of photons in X-ray techniques, but long time scales are a drawback for computer simulations. Part of the significance of this work lies in how neutron signals of different, but complementary, techniques should be interpreted and reconciled. Other new aspects involve the modifications made to an existing simulation model, in order to describe the slow aggregation of colloids at low reaction speeds. This study may expand the techniques available to biology, contribute to innovations in food industry and improve simulation work on the formation of non-analytical materials.

1.2 Materials

Colloids consist of particles substantially larger than atoms or ordinary molecules but too small to be visible to the unaided eye. Colloidal systems may exist as dispersions of one substance in another, like mayonnaise which consists of oil droplets in vinegar, or as single materials, such as rubber or the membrane of a biological cell. Generally at least one dimension of the colloidal particle has a size ranging from 1 nm to 10 µm, including thin films and fibers. Many colloids fall into the soft condensed matter category. Colloidal dispersions are classified by their two phases. The categories divide all combinations of solid, liquid and gaseous phase except gas–gas, which mixes on a molecular level. Systems of solid particles suspended in a solid or liquid medium are called sols. Suspensions of a liquid in a solid are called gels and emulsions when dispersed in another liquid. Microscopic gas bubbles in a solid or a liquid are called foams. Solid and liquid particles suspended in a gas, like smoke and clouds, are called aerosols.

Suspended colloidal particles do not precipitate under standard conditions. In solid media, they are fixed in a matrix. In liquids and gases, the thermal motion of the molecules counters the force gravity exerts on the much larger particles. These random collisions result in Brownian motion of the particles. In stable colloidal suspensions, the forces between particles are mostly short-range and repulsive. Hard sphere colloids can therefore be modeled using the same techniques used to describe the behavior of ideal gases. To remain suspended, particle sizes are limited by the difference in weight between particle and medium; for common densities these sizes are too small to be observed with a normal microscope. Particles may be separated from the medium using an ultra-filtration membrane or deposited on a surface using an ultra-centrifuge. Colloid formation occurs spontaneously in systems through attractive physical forces between molecules, such as the Van der Waals force, or through minimization of the Gibbs free energy, where the self-organizing processes are driven by reduction of the chemical potential at constant pressure and temperature. Colloidal particles can also be created using techniques involving high shear, which finely distributes one phase throughout another in a composition of two non-mixable states.

1.3 Processes

Understanding the clustering behavior of randomly distributed components has many applications in science, industry and everyday life. Cluster analysis is a common statistical technique, used for pattern recognition in artificial intelligence and neural networking in bio-informatics, but also for social network analysis in sociology and to study group disease cases in epidemiology. Physics

examines the clustering behavior of many natural phenomena. The clustering of stellar material is studied in astrophysics to understand the gravitational collapse within giant molecular clouds, which leads to the formation of stars, star clusters and galaxies. In statistical thermodynamics clustering can explain phase transitions of matter. The Ising model for example, describes the behavior of ferromagnets near the Curie point, but also of fluids at the vapor/liquid critical point. Insight into clustering processes allows the prediction of network structure, denseness, cohesion and average path length. Phase transitions caused by clustering of matter are studied in physical chemistry. The sol–gel transition occurs when suspensions of solid particles in a liquid aggregate into a solid matrix that encapsulates the liquid. Gelation changes many properties, such as a drastic increase in viscosity, as a liquid-like system becomes solid-like.

To study the sol–gel phase transition of colloids, a sticky sphere model is used in a Monte Carlo scheme to simulate the aggregation of the particles into clusters and of these clusters into a network. This is usually done for the case of immediate bonding when particles touch. However, actual aggregation processes do not necessarily occur under high reactivity conditions. When the reactivity is very low compared to particle diffusion, a great many more particle collisions is required for bonding, which does not only take much more time, but also results in different structures. Many clustering processes also show an increase in reactivity throughout aggregation. During the gelation of milk to yogurt for example, the pH in milk starts roughly neutral, but decreases as bacterial cultures increase the acidity. The milk micelles therefore aggregate with an increasing reactivity.

1.4 Optics

Neutrons are uncharged mass particles with a magnetic moment, which exist bound in the nuclei of all atomic elements and isotopes, except hydrogen $\left({}^{1}\mathrm{H}\right)$. Free neutrons have a mean life-time of about 15 minutes and, being sub-atomic particles, propagate as waves according to quantum mechanics. Having no charge, neutrons have little interaction with electrons, but they do interact with the atomic nuclei. This strong force interaction is very short ranged, so that neutrons have to pass close to a nucleus to feel it. Since the nucleus is so much smaller than the atom's electron cloud, neutrons can travel considerable distances in matter. Because of their different interaction with matter, beams of neutrons have different diffraction properties than X-rays.

Diffraction is an interference phenomenon of waves. It occurs whenever a wave encounters an obstacle of comparable size. The size of a wave is given by its wavelength, which for radiation is determined by its energy. The angle of

diffraction is determined by the ratio of the wavelength of the wave and the size of the obstacle. Enlarging the object decreases the diffraction angle. A wave can bend around smaller objects or create a wide pattern when leaving larger openings. Such openings are called apertures when used for beams of radiation. The diffraction pattern is inversely related to the shape of the aperture. Figure 1.1 shows an example for a circular or spherical object, such as a disk or a sphere. Multiple closely-spaced openings provide a complex pattern of varying intensities, from which the geometry of the obstructing object can be inferred. Radiation with wavelengths in the range of Å can be used to investigate the structure of crystals.

Scattering is a type of diffraction where non-uniformities in a medium cause a beam of radiation to deviate from a straight trajectory. Scattering techniques are applied to materials with length scales larger than the unit cells of crystals. These length scales are determined by the sizes of the inhomogeneities, usually particles, or the distances separating them. Scattered intensity patterns provide information about sizes that occur in materials. The mathematical description of how a material scatters incident radiation uses the product of a form factor and a structure factor. These are basically Fourier transforms of the internal and external structure of the particles. The structure factor is a particularly useful tool in the interpretation of interference patterns obtained in X-ray, electron and neutron diffraction experiments. If the kinetic energy of the photons, electrons or neutrons is not conserved, scattering is inelastic. Energy-resolved techniques measure the dynamic structure factor, whereas elastic scattering techniques measure the static structure factor.

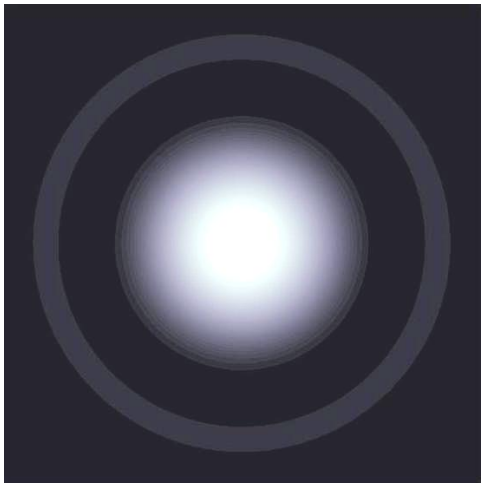

Figure 1.1: Computer generated image of the Airy diffraction pattern, which is observed when waves exit a circular aperture with a diameter in the order of the wavelength. The intensities of the pattern are by determined by a Fourier transform of the shape of the aperture, which yields a damped first order Bessel function. The bright central region, called the Airy disk, is surrounded by weak concentric rings of decreasing intensity.

1.5 Techniques

The Spin-Echo Small Angle Neutron Scattering (SESANS) machine is a correlometer for density fluctuations that scatter neutrons elastically over small angles. It probes these density separations in one direction in real-space using a polarized neutron beam, magnets and flippers to encode the scattered intensity as loss in polarization. Structures with typical lengths between 10 nm and 10 µm can be observed. The measured signal consists of the scattered neutron intensity and a projection of the density correlation function, describing the structure of the sample. The resolution function of SESANS is given by the empty beam polarization as a function of spin-echo length and can simply be divided out of the signal. The loss of empty beam polarization at large spin-echo lengths is the main limiting factor for the resolvable length scale range. A good signal-to-noise ratio in SESANS requires relatively large amounts of coherent scattering, compared to similar techniques. Ideal samples have sufficiently high neutron transmission and a large scattering contrast. In colloidal suspensions the contrast is between the small particles and the surrounding homogeneous liquid and for dilute cases the scattering power is roughly linear with concentration. See § 3.2.1 for a more detailed description of the technique.

Ultra Small Angle Neutron Scattering (USANS) is a neutron diffraction machine that measures scattered intensity at very small angles. This high resolution in reciprocal space makes USANS sensitive to a large range in length scale, comparable to the resolving range of SESANS. The measured signal consists of a projection of the scattered intensity in momentum-space, convoluted with the USANS resolution function. The USANS setup uses a monochromator and an analyzer crystal, which is either constantly bent or continuously rocked during measurement. The length scale range is limited both by the crystal's fixed curvature respectively range of rotation-angle, as well as by the resolution of the detector. §3.2.2 provides further details on the technique and the data treatment.

Monte Carlo (MC) simulations are a stochastic method for exploring the phase-space of a system by random sampling of a quantity that drives the simulation. In this study MC is used to model the aggregation of colloids in order to study gelation. In this case the random sampling involves displacing single and clustered particles in a box as opposed to their simultaneous movement, and to a variable degree the random formation of bonds between particles. This variable degree provides control of the clustering mechanism. § 4.2.2 offers the particulars of the model.

1.6 Thesis overview

This study focuses on spherical particles suspended in water as sols, emulsions and gels. Of interest are both the internal structure of the spherical colloids and the external structure formed by the aggregation of homogeneous colloids. SESANS and USANS are the primary and secondary experimental methods that have been employed to observe structures and the kinetics of their formation. Dynamic Light Scattering has also been used to obtain *a priori* knowledge and to verify results. Measurements have been described by modeling systems and curve fitting the model parameters to the experimental data. MC simulations in 3D of adhesive spheres have been performed in order to gain better insight into the process of gelation, which is not yet well understood.

Chapter 2 deals with observations on and modeling of the internal structure of biological colloids by means of SESANS and includes some DLS measurements. A detailed comparison is made between predicted signals from solid, hollow and filled spheres with SESANS measurements on liposomes and *Escherichia coli* bacteria. A numerical outlook is provided for the usefulness of SESANS in drug targeting studies for cancer treatment.

Chapter 3 studies the kinetics of the gelation of milk to yoghurt using SESANS and USANS observations and MC simulations. The size distribution of casein micelles in milk is observed, as well as the increase in length scales and change in dimensionality when milk gelates to yoghurt are observed, along with the time scale of the process. The MC simulations describe gelation as clustering of monodisperse spheres, producing a numerical density correlation function, which is compared to neutron scattering data.

Chapter 4 deals exclusively with the MC simulations on a 3D lattice, studying the effect of varying reactivity with monomer concentrations varying from dilute to concentrated. A numerical recipe is given to model the sol–gel transition of monodisperse hard spheres using a time-dependent reactivity. This allows for a range of regimes to be explored from Reaction Limited Cluster–cluster Aggregation (RLCA) at extremely low reactivity to Diffusion Limited Cluster–cluster Aggregation at maximum reactivity. New algorithms are described to speed up the code when motion becomes sporadic and for when bonding is scarce.

Chapter 5 shows the derivation of the optimal sample thickness for SESANS experiments. This is achieved by defining the quantity that expresses signal quality, expressing the measurement error in the signal as a function of the sample thickness and finding the minimal value as a function of known parameters.

CHAPTER 2

SESANS analysis of liposomes and bacteria

Léon F. van Heijkamp, Ana-Maria Sevcenco, Diane Abou, Remko van Luik, Gerard C. Krijger, Peter-Leon Hagedoorn, Ignatz M. de Schepper, Bert Wolterbeek, Gerben A. Koning and Wim G. Bouwman, 'Spin-Echo Small Angle Neutron Scattering analysis of liposomes and bacteria', J. Phys. Conf. Ser. **247** (2010) 012016.

Abstract

Two types of liposomes, commonly used in drug delivery studies, and *E. coli* bacteria, all prepared in H_2O, were resuspended in D_2O and measured with Small Angle Spin-Echo Neutron Scattering (SESANS). Modeling was performed using correlation functions for solid spheres and hollow spheres. The signal strength and curve shape were more indicative of hollow particles, indicating that the H_2O–D_2O exchange occurred too fast to be observed with the available time resolution. Fitting the particle diameter and membrane thickness of the hollow sphere model to the data, gave results which were in good agreement with Dynamic Light Scattering (DLS) data and literature, showing as a proof-of-principle that SESANS is able to investigate such systems.

SESANS may become a good alternative to conventional tritium studies or a tool with which to study intracellular vesicle transport phenomena, with possible *in vivo* applications. Calculations show that a substantial change in numbers of a mixed system of small and large biological particles should be observable. A possible application is the destruction by external means of great numbers of liposomes in the presence of tumor cells for triggered drug release in cancer treatment. Since SESANS is both non-invasive and non-destructive and can handle relatively thick samples, it could be a useful addition to more conventional techniques.

2.1 Introduction

DELIVERY of drugs or contrast agents to tumors and their uptake by tumor cells is of great interest to the medical community to aid the diagnosis and treatment of cancer [1–5]. In order to develop improved methods to identify and destroy malignant tumor tissue, research has focused on the transport of substances across the bi-lipid layer using encapsulation by liposomes [1, 6–10]. These lipid vesicles have a similar composition to cellular mebranes and are therefore also used as a model in transport studies. The cellular transport of water is an important quantity for medical diagnostic tools using cellular contrast agents. Much work has been done studying two key processes: the internalization of small cells and particles by larger cells [11–14] and the rate at which water can diffuse in and out of cells [15–17]. For the development of cancer treatment it is desirable to be able to observe both liposomal uptake by tumor cells and cellular water exchange as directly as possible in living patients, using non-invasive methods. Many observations can be done down to the cellular level in a laboratory or inside living patients, using methods as Dynamic Light Scattering (DLS) and Magnetic Resonance Imaging (MRI).

Water transport is often studied using tritiated water (T_2O, HTO) as a tracer. Changing concentrations of this isotope produce local changes in levels of radioactivity. This technique is used to observe metabolic processes in laboratory animals [11], but not generally applied *in vivo* to larger organisms because of its radioactivity, which increases the chance of cancer when applied internally. For water transport studies with liposomes, the tritiated liposomes have to be separated from the medium. Since it is a weak β-particle emitter, experiments require either large quantities or the very sensitive liquid scintillation detectors. All this makes it unsuitable for *in vivo* application, whereas SESANS does not have these limitations. Furthermore, the exchange rate of this super-heavy water with normal, light water (H_2O) provides little information on cellular structure.

Small Angle Neutron Scattering has been employed in the past to study cellular components, such as ribosomes [12], DNA (including helical structure) [13], protein [14] and lipid structures [18, 19] and protein hydration [20]. Using Spin-Echo Small Angle Neutron Scattering (SESANS) microstructures of 20 nm to 20 µm can be observed, corresponding to sub-cellular and cellular sizes. The sample thickness depends on the neutron transmission of the investigated substance. The sensitivity of neutron scattering experiments to the hydrogen-deuterium contrast is often exploited in watery samples. Typical sample thicknesses in SESANS are one centimeter when containing mostly light water, and up to several centimeters when using mostly heavy water, or deuterium oxide

(D_2O, HDO). Neutron scattering is non-invasive and a SESANS measurement exposes samples only to small doses of radiation, because it requires limited neutron intensities with moderate wavelengths. For stable biological samples, this technique can be easily applied *in vitro* when containing either light or heavy water or both. SESANS can in principle also be applied to organisms *in vivo* without deuterating, if there is enough contrast and no more than a few centimeters of water in the beam. Water transport across cell membranes can be studied *in vitro* with SESANS by observing changes in contrast, due to local changes in light and heavy water concentration. Although deuterium is a non-radioactive isotope, large amounts of this heavy water can still be harmful to organisms. Some normal reactions in cells, especially cell division, are disrupted by the stronger hydrogen bonds formed. Toxic levels of deuteration range from around 30% to 50% for rodents and large mammals respectively [21, 22]. Since it is not possible to replace large amounts of water with D_2O without any harmful effects, an *in vivo* SESANS study focussing on water exchange in human cells will be difficult.

SESANS experiments were performed on liposomes and bacteria, as prototypes for small and large cells. The aim was to observe both as whole cells and investigate water transport through the membranes. All samples were prepared or grown in H_2O-based buffers or growth media and finally resuspended in D_2O. The liposomal polydispersity was determined using DLS. Fitting the measurement data showed the average cell diameters[I], cell-wall thicknesses and the inner contrast with respect to the medium, which were in good agreement with expected values from other techniques and literature. The rate of hydrogen–deuterium exchange could only be observed if the timescale was within the temporal resolution of the technique, which was not the case for any of the measured liposomes. A neutron source with a higher flux and larger wavelength should significantly increase the temporal resolution of the SESANS setup. Anticipating future developments, time-dependent measurements may become possible so that water exchange may be observed as well.

Model calculations predicted that large-scale removal of liposomes from a sample, through destruction by external means or biological process, should be observable with SESANS. A large drop in the liposome population of an investigated system would result in a change of curve shape and more noticeably, a change in the polarization saturation level, due to a change in the scattering power of the whole sample. SESANS measurements performed so far on small amounts of tumor cells exhibited too little scattering for a significant signal. Measurements on combined systems of liposomes with much higher concentrations of tumor cells are to be performed in the future.

[I] To our knowledge, the first time observing entire cells using neutrons.

The aim of this paper is to show as a proof of principle that SESANS has the potential to contribute to studies on biological bulk-phenomena, without disturbing the investigated systems. It may therefore become a useful addition to the broad range of techniques already available, with possible applications in the field of cancer research.

2.2 Biological background

2.2.1 Liposomes

A liposome is a spherical vesicle that consists of a bilayered phospholipid membrane, entrapping an aqueous phase. In this study the lipid vesicles only contain H_2O or D_2O or both. The membrane is made of natural substances: lipids and cholesterol that confer biocompatibility, non-toxicity, and biodegradable properties. The phospholipids are amphiphilic, consisting of a hydrophilic phosphate head group and two hydrophobic tails, which causes them to self-organize into lipid bilayers in an aqueous environment. Over the last decade, liposomes have largely been used in the medical field as a tool for drug delivery for therapeutic purposes and, more recently, for molecular imaging in disease diagnoses.

Liposomes are classified as Large Multilamellar Vesicles (LMV) or as Large and Small Unilamellar Vesicles (LUV and SUV). The SUV is the main interest of the present study, because it is the most used type of liposome in the medical field. The optimum liposome diameter for an efficient extravasation out of the blood into a tumor is known to be around 100 nm. This is an important property for passive drug-targeting of the diseased area, especially for tumor-targeting of multiple types of cancers. Stealth® liposomes are grafted with PolyEthylene Glycol (PEG)-chains and offer additional advantages, such as avoiding self-aggregation of the particles and enhancing the in vivo half-life by reducing the interaction with the blood plasma proteins. For this study, DSPC and DPPC SUV PEGylated liposomes have been synthesized with a diameter D of about 100 nm and a membrane thickness T of about 5 nm [23] and characterized using DLS and SESANS. DSPC and DPPC liposomes posses different membrane rigidity and therefore different water exchange properties.

2.2.2 *Escherichia coli*

The microorganism *Escherichia coli* (*E. coli*) is a well known species of bacterium, discovered by German pediatrician and bacteriologist Theodor Escherich in 1885. *E. coli* is placed on the bacteria branch in the phylogenetic tree of life as a gram negative bacterium, and can grow easily under both aerobic and anaerobic conditions and by fermentation. Optimal growth occurs at 37°C, but

Molecule	Formula	b [fm]	V_m [Å^3]	ρ_s [nm^{-2}]
DPPC	$C_{40}H_{80}NO_8P$	27.63	1,232	$2.2{\cdot}10^{-5}$
head	$C_{10}H_{18}NO_8P$	60.1	326	$18.4{\cdot}10^{-5}$
tails	$C_{30}H_{62}$	32.4	891	$-3.6{\cdot}10^{-5}$
Cholesterol	$C_{27}H_{46}O$	13.25	629	$2.1{\cdot}10^{-5}$

Table 2.1: Coherent neutron scattering lengths, component volumes and scattering length densities for DPPC, its head and tails, and cholesterol [25]. By comparison, DSPC consists of $C_7H_{16}NO_4P$ (head group) and $C_{37}H_{72}O_4$ (tails), giving $C_{44}H_{88}NO_8P$.

Phases	$\lvert\Delta\rho_\mathrm{s}\rvert$ [nm^{-2}]
$H_2O - D_2O$	$6.89{\cdot}10^{-4}$
lipid $- H_2O$	$0.76{\cdot}10^{-4}$
lipid $- D_2O$	$6.13{\cdot}10^{-4}$

Table 2.2: Absolute differences in scattering length density of phases under consideration.

in some cases multiplication occurs at temperatures below 25°C and up to 49°C. The cells may have flagella and are about 2 µm long and 0.8 µm in diameter [24], with a volume of 0.6–0.7 µm^3. Strains that possess flagella can swim and are motile. There are many different types of *E. coli* based on the antigen type: the somatic (O) antigen, the capsular (K) antigens and the flagellar (H) antigen. There are over 170 O antigens, over 100 K antigens and over 50 H antigens.

Bacteria do not posses a cell nucleus or any other large structures, but have their components scattered throughout the cytoplasm. Since none of these are observable with the techniques used in this study, *E. coli* will also be considered as empty vesicles. The strain K12 was selected, since it is safe to handle and easy to grow, with cell division occurring every 20 minutes under absolutely optimal conditions. It is also easily-manipulated, making it one of the most-studied prokaryotic model organisms, and an important species in biotechnology.

2.2.3 Contrast of lipid bilayers

Coherent neutron scattering occurs in materials due to fluctuations in scattering length density (SLD), defined as the total bound coherent scattering length b divided by the occupied volume V_m. In this system, the largest SLD-difference arises between either H_2O inside and D_2O outside the liposomes and bacteria, or between their lipid bilayers and the D_2O medium. For the lipid bilayers the average SLD is taken, so that the SLD-profile over the membrane is represented by a constant. Using the chemical formulas and the mass or number densities of the compounds, the overall SLD of lipid bilayers can be calculated according to

$$\rho_\mathrm{s} = \frac{\sum_i n_i\, b_i}{\sum_i n_i\, V_{\mathrm{m},i}}. \tag{2.1}$$

Estimating the mass densities of the organic compounds to be between 0.8 and 1.0 kg/m^3 and using tabulated scattering lengths [26], yields values around

ρ_s=2·10^{-5} nm^{-2} for both liposomes[II]. This result is irrespective of the $\frac{1}{3}$ molar cholesterol, since it has a similar SLD. The few molar % contributions of the PEG chains are neglected. Literature values [25] of molecular volumes for DPPC and cholesterol support these assertions, giving ρ_s=2.2·10^{-5} nm^{-2} and ρ_s=2.1·10^{-5} nm^{-2} using eq. 2.1, as summarized in table 2.1. Lacking the necessary data to calculate the SLD for the membrane of *E. coli*, the lipsome values have been used under the assumption that both membranes have an SLD of the same order of magnitude. H_2O and D_2O have similar mass densities of ρ=1.0 and 1.1 kg/m^3 respectively, but massively different scattering length densities of ρ_s=−5.6·10^{-5} and +6.33·10^{-4} nm^{-2}. The resulting SLD-differences between the lipid membrane, H_2O and D_2O are listed in table 2.2.

2.3 Experimental

2.3.1 Sample preparation

Liposomes

List of chemicals. — *1,2-distearoyl-sn-glycero-3-phosphorylcholine* (DSPC, with chemical formula $C_{44}H_{88}NO_8P$), *1,2-dipalmitoyl-sn-glycero-3-phosphocholine* (DPPC with formula $C_{40}H_{80}NO_8P$) and *1,2-distearoyl-sn-glycero-3-phosphoethanolamine-N-[methoxy-(polyethylene glycol)-2000]* (DSPE-PEG2000 -OMe) were supplied by Lipoid AG, Cham, Switzerland. Cholesterol ($C_{27}H_{46}O$) was purchased from Avanti polar Inc., Alabaster, AL, USA.

Formulation. — DSPC and DPPC liposome batches were prepared independently. The first batch consisted of 200 µmol total compound amount with DSPC:cholesterol:DSPE-PEG2000-OMe ratios of 1.75:1:0.25 dissolved 1:1 in chloroform ($CHCl_3$) and methanol (MeOH). The second batch consisted of 100 µmol with DPPC:cholesterol:DSPE-PEG2000-OMe ratios of 1.85:1:0.15, which were dissolved 1:1 in dichloromethane (CH_2Cl_2) and MeOH. Both mixtures were vacuum-dried to obtain thin lipidic films, which were hydrated and resuspended in MilliQ. These mixtures were subsequently extruded through polycarbonate membrane filters with a pore size of 200 nm (ten times) and 100 nm (ten times), using Lipofast extruder (Avestin, Canada). The temperature during the extrusion was set around 50°C. The extruded solution was ultra-centrifuged for 60 minutes at 4°C at 45 krpm (0.30 Mg) and at 40 krpm (0.23 Mg) respectively for both batches, using an ultracentrifuge Beckman L7, rotor 50 Ti. The pellets were separated from the supernatant and injected into cuvettes with 5 ml D_2O.

[II] Ranging from 1.5·10^{-5} to 1.9·10^{-5} nm^{-2}(DSPC) and from 1.8·10^{-5} to 2.3·10^{-5} nm^{-2}(DPPC).

E. coli

Wild-type *E. coli* K12 strains were grown at 37°C overnight in 200 ml Luria Bertani medium in 500 ml Erlenmeyer flasks under shaking conditions until a standard optical density was reached (O.D.=2 using a wavelength of 600 nm). The cells were spun down using a Jouan CR 4.11 centrifuge at 3.5 krpm at 4°C for 60 minutes. Wet pellets were re-suspended in D_2O after washing with 10 ml D_2O to eliminate the excess of water in between the cells. Centrifugation was repeated and the obtained new pellets were re-suspended in 2 ml D_2O each after vortexing with a home-made bead beater at 2.5 krpm at 4°C for 30 minutes. Four homogeneous pellets totaling 0.4 g were injected into a cuvet with 4 ml D_2O.

2.3.2 The SESANS Technique

Principles

Spin-Echo Small Angle Neutron Scattering (SESANS) is a non-destructive technique that probes density correlations in real space directly from 20 nm up to 20 µm. SESANS uses spin-echo to encode small scattering angles of neutrons when traversing a sample and it measures the effective loss of polarization of a neutron beam as a function of spin-echo length. This method is used to study the structure of suspensions of mesoscopic particles and its range of accessible length scales makes it suitable for a variety of materials, including large colloids [27] and granular matter [28]. The used SESANS setup consists of a monochromatic, polarized neutron beam traveling in the horizontal x-direction through two magnetic field regions, in between which a sample is placed. Experiments are performed by varying the magnetic field strength to probe correlations along the vertical spin-echo length z. The technique is not sensitive to the y-direction and can be described classically, as the net Larmor precession of neutrons of a polarized neutron beam [29], or quantum-mechanically, as the vertical splitting and recombination of two neutron eigenstates, due to their different interaction with a magnetic field [30, 31]. The polarization P of the beam, normalized with the empty beam polarization P_0, depends on the scattered fraction of the beam $\Sigma\,\ell$ and on the normalized, dimensionless function $G(z)$:

$$\frac{P}{P_0}(z) = \mathrm{e}^{\,\Sigma\,\ell\,[G(z)-1]} \tag{2.2}$$

where ℓ is the neutron path length through the sample, i.e., the sample thickness, Σ is the average number of times a neutron scatters per unit length and $G(z)$ is a measure of the microstructure. It is the projection along the neutron beam of the density auto-correlation function, which correlates SLD-

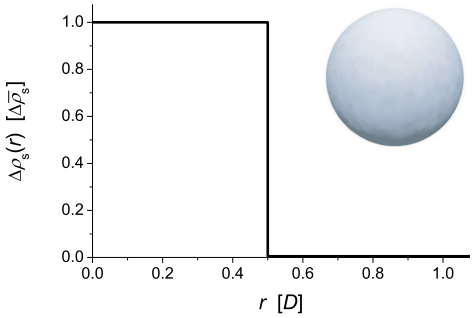

Figure 2.1: A solid sphere of diameter D has a homogeneous SLD-distribution $\rho_s(r)$ inside the sphere, where the average difference $\overline{\Delta\rho_s}$ is with respect to the SLD of the medium outside the sphere.

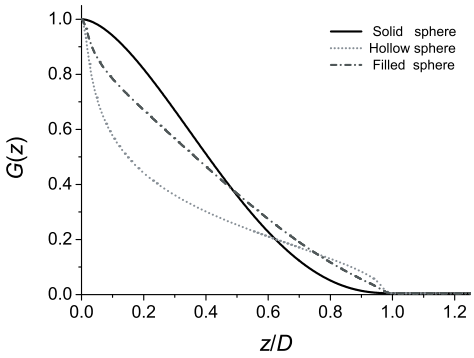

Figure 2.2: Examples of the projected correlation functions for solid, hollow and filled spheres, using $T = \frac{1}{10}D$ for the shell thickness and $s = 0.1$ for the core contrast. See the text for further details.

fluctuations throughout the sample and is denoted $\gamma(r)$ for isotropic systems, such as here. Long-range correlations disappear beyond distances z_{sat}, so that $G(z \geq z_{\mathrm{sat}}) = 0$, causing the polarization signal to saturate. The amount of scattering Σ depends on beam and sample properties:

$$\Sigma = \lambda^2 \left\langle \Delta\rho_s^2 \right\rangle \xi \overset{\text{binary}}{=} \lambda^2 \, \phi_V (1-\phi_V) \, \overline{\Delta\rho_s}^2 \, \xi \tag{2.3}$$

with neutron wavelength λ, SLD-variance $\left\langle \Delta\rho_s^2 \right\rangle$ and correlation length ξ. For a two-phase system the mean-squared SLD-difference can be expressed as the squared average difference $\overline{\Delta\rho_s}^2$ (contrast) between the two phases, multiplied with the volume fraction ϕ_V of the suspended phase and the medium. The correlation length ξ is defined as the integral over $\gamma(r)$ along x at $z = 0$ and can be interpreted as the average length that neutrons travel through one phase before encountering another phase, making ξ a measure of typical length scale.

Correlation Functions

For dilute systems, the auto-correlation function $\gamma(r)$ gives the shared volume fraction of an object with an overlapping copy of itself. Analytical expressions for $\gamma(r)$ and its projection $G(z)$ have been derived for several dilute, monodisperse [32] and polydisperse [33] model systems such as solid and multi-layered spheres, using geometry and calculus.

Solid spheres. — A solid sphere of diameter D has a constant density distribution $\rho_s(r)$ inside volume $V_{\mathrm{sphere}} = \frac{1}{6}\pi D^3$. The density correlation function is equal to the shared volume fraction of two identical spheres when separated by a distance $0 \leq r \leq D$ from center to center. This lens shaped volume consists of

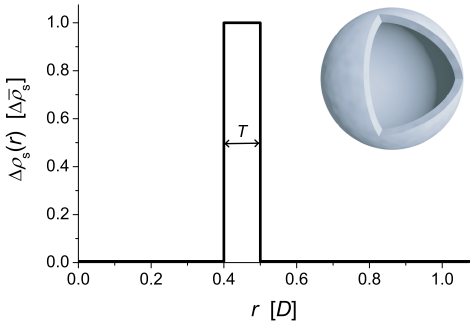

Figure 2.3: A hollow sphere of diameter D and shell thickness T has a constant SLD-difference $\overline{\Delta\rho_s}$ distributed over a spherical shell, with respect to the medium on the inside and the outside.

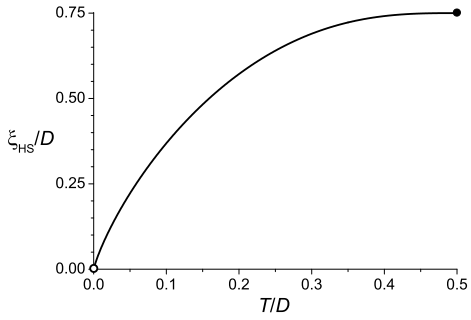

Figure 2.4: The hollow sphere correlation length $\xi_{\rm HS}$ of diameter D as a function of shell thickness T, between the limits of an infinitely thin shell ($T\downarrow 0$) and a solid sphere ($T=\frac{1}{2}D$).

two equal sphere caps, so that $\gamma_{\rm SS}(r)=1-1\frac{1}{2}\frac{r}{D}+\frac{1}{2}\left(\frac{r}{D}\right)^3$ is readily derived. The analytical expression for the projected correlation function is

$$G_{\rm SS}(z) = \Re\left\{\sqrt{1-\left(\frac{z}{D}\right)^2}\left[1+\tfrac{1}{2}\left(\frac{z}{D}\right)^2\right] + 2\left(\frac{z}{D}\right)^2\left[1-\tfrac{1}{4}\left(\frac{z}{D}\right)^2\right]\ln\frac{\frac{z}{D}}{1+\sqrt{1-\left(\frac{z}{D}\right)^2}}\right\}, \tag{2.4}$$

where $\Re$ denotes the real part. The correlation length of a solid sphere is

$$\xi_{\rm SS} = \tfrac{3}{4}D. \tag{2.5}$$

Hollow spheres. — A hollow sphere of outer diameter D and shell thickness T has its density homogeneously distributed in a spherical shell of volume $V_{\rm shell}=\pi D^2T-2\pi DT^2+\frac{4}{3}\pi T^3$ and is obtained by subtracting the density distribution of a sphere from that of a larger sphere. The elaborate expression for the correlation function (not shown) has been derived analytically by auto-convolution of the density distribution of the hollow sphere [32]. The projected correlation function is given by

$$G_{\rm HS}(z;D,T) = \tfrac{2}{3}\ F(\tfrac{2}{D}z, \tfrac{D-2T}{D})/f(\tfrac{D-2T}{D})\ . \tag{2.6}$$

The normalization of $G_{\rm HS}(z)$ is performed by the smooth dimensionless function

$$f(\sigma) = (1-\sigma)\left(1-\sigma^3\right) + \tfrac{1}{2}\left(1-\sigma^2\right)^2\ln\frac{1+\sigma}{1-\sigma}. \tag{2.7}$$

with argument $0\le\sigma<1$, where $\sigma=\frac{D-2T}{D}$ is the ratio between inner and outer diameter. When considering a fixed diameter D, then for an infinitely thin shell $T\downarrow 0$ gives $\lim f(\sigma\uparrow 1)=0$, and for $T=\frac{1}{2}D$ the shell fills the sphere, so that

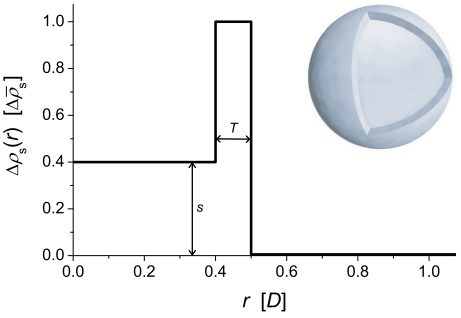

Figure 2.5: A filled sphere has two values $\Delta\rho_s(r)$ characterized by the parameter s, as the core and the shell have separate SLD-differences with the medium. It is equal to a hollow sphere for $s=0$ and to a solid sphere for $s=1$.

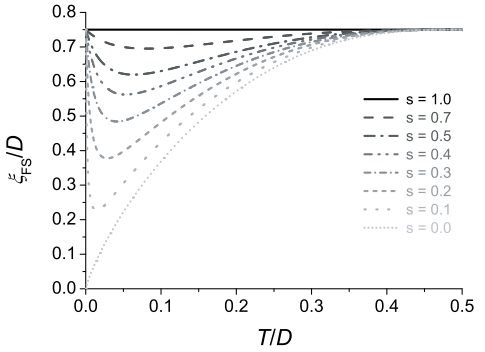

Figure 2.6: The correlation length ξ_{FS} of a filled sphere of diameter D as a function of shell thickness T, with s ranging from a hollow sphere (s=0) to a solid sphere (s=1). For infinitely thin shells ($T \downarrow 0$) only the core remains if $s > 0$, giving $\xi_{\mathrm{FS}} = \xi_{\mathrm{SS}}$.

$f(\sigma=0) = 1$. From this function the correlation length has been derived, which is given by

$$\xi_{\mathrm{HS}} = \frac{2T}{D}\left(1 + \tfrac{2}{3}\frac{D^2 - 2DT + T^2}{D^2 - 2DT + \tfrac{4}{3}T^2}\,\ln\frac{D-T}{T}\right)\tfrac{3}{4}D. \tag{2.8}$$

For the limiting case of a shell of half the diameter ξ_{HS} becomes equal to ξ_{SS} in nearly constant fashion, and for a hollow sphere with an infinitely thin membrane ξ_{HS} can be shown to approach zero nearly linearly. Figure 2.4 shows the dependency of the correlation length of a hollow sphere on the relative shell thickness.

$F(\zeta,\sigma)$ expresses the correlations between different parts of the geometry of a hollow sphere in a dimensionless function

$$\begin{aligned} F(\zeta,\sigma) = {} & H(2,\zeta) - H(1{+}\sigma,\zeta) + H(1{-}\sigma,\zeta) \\ & + \sigma^4 H(2,\tfrac{\zeta}{\sigma}) + \sigma^4 H(\tfrac{1-\sigma}{\sigma},\tfrac{\zeta}{\sigma}) - \sigma^4 H(\tfrac{1+\sigma}{\sigma},\tfrac{\zeta}{\sigma}) \\ & - 2\sigma^3 h_1(1{-}\sigma,\zeta) + \tfrac{3}{8}\left(1{-}\sigma^2\right)^2\left[h_2(1{+}\sigma,\zeta) - h_2(1{-}\sigma,\zeta)\right]. \end{aligned} \tag{2.9}$$

which is constructed from

$$\begin{aligned} h_1(\alpha,\zeta) &= 2\Re\left\{\sqrt{\alpha^2-\zeta^2}\right\} \\ h_2(\alpha,\zeta) &= \Re\left\{\ln\frac{2\alpha + h_1(\alpha,\zeta)}{2\alpha - h_1(\alpha,\zeta)}\right\} \\ H(\alpha,\zeta) &= \left(1 - \tfrac{3}{8}\alpha + \tfrac{1}{64}\alpha^3 + \tfrac{3}{128}\alpha\zeta^2\right) h_1(\alpha,\zeta) - \tfrac{3}{8}\zeta^2\left(1 - \tfrac{1}{16}\zeta^2\right) h_2(\alpha,\zeta) \end{aligned} \tag{2.10}$$

using the dimensionless spin-echo length σ and inner–outer diameter ratio ζ

$$\sigma = \frac{D - 2T}{D}$$
$$\zeta = \frac{2z}{D}$$

as short-hand symbols.

Filled spheres. — An intermediate model is that of the filled sphere, which has a solid spherical core with a shell around it. A filled sphere has the density distribution of a hollow sphere filled with a third phase. The corresponding correlation function is constructed from the hollow sphere model by addition of a dimensionless parameter s, defined as the ratio between differences in SLD of core and shell with the medium:

$$s = \frac{\rho_{\mathrm{s}}^{\mathrm{core}} - \rho_{\mathrm{s}}^{\mathrm{medium}}}{\rho_{\mathrm{s}}^{\mathrm{shell}} - \rho_{\mathrm{s}}^{\mathrm{medium}}} = \frac{\Delta\rho_{\mathrm{s}}^{\mathrm{core}}}{\Delta\rho_{\mathrm{s}}^{\mathrm{shell}}}. \tag{2.11}$$

The projected correlation function for a filled sphere then becomes

$$G_{\mathrm{FS}}(z; D, T, s) = \tfrac{2}{3}\, \frac{F\left(\frac{2z}{D}, \frac{D-2T}{D}\right) + \frac{s}{1-s} H\left(2, \frac{2z}{D}\right) - s\left(\frac{D-2T}{D}\right)^4 H\left(2, \frac{2z}{D-2T}\right)}{f\left(\frac{D-2T}{D}\right) + \frac{s}{1-s} - s\left(\frac{D-2T}{D}\right)^4}. \tag{2.12}$$

The behaviour of this correlation function is very close to that of hollow spheres and solid spheres, when s is close to 0 and 1 respectively. How quickly it deviates with s from these two cases, depends on the value of T. The difference between a filled sphere and a hollow sphere is negligable for $0 \leq s \lesssim \frac{2T}{D}$. The correlation length of a filled sphere is

$$\xi_{\mathrm{FS}} = \frac{(1-s)\, f\left(\frac{D-2T}{D}\right) + s - s(1-s)\left(\frac{D-2T}{D}\right)^4}{1 - (1-s^2)\left(\frac{D-2T}{D}\right)^3}\, \tfrac{3}{4} D. \tag{2.13}$$

An example of the projected correlation functions for dilute, monodisperse solid, hollow and filled spheres is shown in figure 2.2, using a shell thickness $T = \frac{1}{10} D$ for the hollow and filled spheres and a value of $s = \frac{1}{10}$ for the filled spheres, giving their core 10% of the $\Delta\rho_{\mathrm{s}}$ between shell and medium.

2.3.3 SESANS Experiments

Experiments & Sample stability

SESANS measurements were performed with a neutron wavelength λ=2.09 Å on the DSPC and DPPC batches of liposomes and on *E. coli*. All samples were measured in quartz cuvettes of thickness ℓ=1.00 cm, with volume fractions of respectively ϕ_{V}=0.02 and ϕ_{V}=0.09 for the liposome and *E. coli* samples. The DSPC liposome concentration was found by phosphate determination according to Rouser; the *E. coli* concentration was calculated from the pellet mass, assuming weight densities equal to H_2O and assuming no losses during the final suspension. Repeat measurements and DLS showed the liposome samples to remain stable for several days. An onset of sedimentation was observed for the *E. coli* after one day, most likely because of cell death as the D_2O environment contained no nutrients. Measurements with lower *E. coli* concentrations provided similar data with regards to particle dimensions.

Modeling

Two cases were considered for curve fitting: no H_2O–D_2O exchange versus full exchange. All fits were performed using non-linear least-squares regression with 95% confidence bounds. The first case could be represented by droplets of H_2O in a D_2O environment, since the effect of the cell membrane on the neutron signal would then be negligible. This model consisted of the projected correlation function $G(z)$ for dilute, monodisperse solid spheres and curve fitting was performed for the amount of scattering and particle size, i.e., the saturation level P_{sat} and diameter D. In the second case, the H_2O would be extremely diluted throughout the D_2Oinside and outside the cells, making the cell membrane contribute significantly to the signal. This system was modeled as hollow spheres filled with D_2O using the $G(z)$ for dilute, monodisperse spherical shells. Fitting was performed for saturation level P_{sat}, outer diameter D and membrane thickness T.

Assumptions

All samples were treated as isotropic systems and modeled with analytical expressions for monodisperse spherical particles. Since the concentrations used were dilute to semi-dilute, excluded volume effects were insignificant. Samples without sedimentation were isotropic suspensions, since all particles had rotational freedom. Particle size distributions were not considered to have a substantial effect and not included in the modeling, based on the very small degree of liposomal polydispersity as observed with DLS and the fact that *E. coli* multiply through cell-division, causing a uniform and highly monodisperse population under standard conditions.

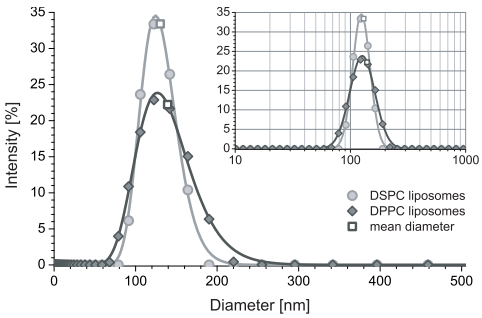

Figure 2.7: Distribution of DSPC and DPPC liposome diameters acquired by DLS. The inset shows approximately normal size distributions on a log-scale. Curves were fit using a lognormal distribution of arbitrary amplitude. Mean liposomal diameters are shown for comparison.

In order to avoid over-parameterization certain assumptions were made. The liposomes were assumed to be spherical since there was no cause for deformation. As a first approximation, the aspect ratio of the *E. coli* cells was disregarded. However, *E. coli* are more rod-like than spherical with an aspect ratio of 2.5. The correlation function of a rod differs from that of a sphere, although arguably less for a hollow body than for a solid one.

2.4 Results

2.4.1 Characterization of liposomes with DLS

To confirm the consistency of the two liposome formulations, dynamic light scattering was used to establish their size distributions in order to characterize them by their average diameter and polydispersity. Due to faster degradation, there was not enough *E. coli* material available to use DLS to confirm their monodispersity. Both liposome size distributions had modes (peak-positions) around 125 nm with an approximately normal distribution of diameters on a logarithmic scale, as shown in the inset of figure 2.7.

The average diameter and distribution width were acquired by fitting a log-normal distribution of diameters to the DLS data, using arbitrary amplitude

Parameter	Meaning	DSPC liposomes	DPPC liposomes
μ	fit value	4.854 ± 0.004	4.905 ± 0.006
σ	fit value	0.174 ± 0.004	0.251 ± 0.005
D_{mode} [nm]	peak	124.4 ± 0.5	126.7 ± 0.8
D_{median} [nm]	middle	128.3 ± 0.5	135.0 ± 0.8
D_{mean} [nm]	average	130.2 ± 0.5	139.3 ± 0.9
PDI [–]	width	0.094 ± 0.002	0.138 ± 0.003

Table 2.3: Log-normal fit results of the size distribution of DSPC and DPPC liposomes acquired by DLS. Fit parameters μ and σ were converted to a mean diameter and polydispersity index.

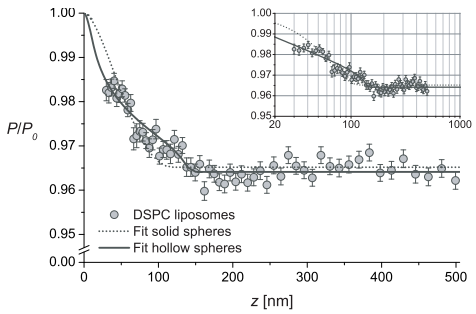

Figure 2.8: SESANS data of DSPC liposomes.

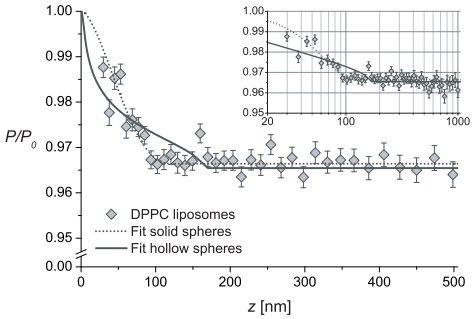

Figure 2.9: SESANS data of DPPC liposomes.

Both figures include log-scale insets. The curves are fits for the solid and hollow sphere models.

and obtaining parameters μ and σ, see Table 2.3. The distribution width was expressed by the polydispersity index (PDI), where a large PDI would cause the mean and median (the diameter halving the population) to shift away from the mode. The median and mean diameters of the DSPC liposomes were close to the mode and with a PDI just below 0.1, the DSPC liposomes were effectively monodisperse particles with a diameter of 130 nm. The DPPC liposomes had a slightly wider distribution with a PDI of 0.14, resulting in an average size of 140 nm.

2.4.2 SESANS Results

Liposomes

Less than 4% scattering was observed for the liposome suspensions in D_2O, requiring more than half a day of measurement time to reach an acceptable signal quality such as shown in figures 2.8 and 2.9. For both the DSPC and the DPPC batch, the polarization saturated at spin-echo lengths z_{sat} above 150 nm and at a saturation level P_{sat}=0.965, where both quantities contained length scale information. Since the liposomes were approximately monodisperse, z_{sat} corresponded to the diameter of the liposomes, which also determined the saturation level through the correlation length (see eq. 2.3 and eq. 2.2 for $G(z)$=0). The amount of scattering provided a constant for the product of contrast and correlation length $\overline{\Delta\rho_{\mathrm{s}}}^2\xi$, where ξ_{SS} and ξ_{HS} were calculated according to eq. 2.5 and eq. 2.8 for the solid and hollow sphere models. The difference in SLD between particle and medium was retrieved as

$$|\Delta\rho_{\mathrm{s}}| = \sqrt{\frac{-\ln P_{\mathrm{sat}}}{\ell\,\lambda^2\,\phi_{\mathrm{V}}\,(1-\phi_{\mathrm{V}})\,\xi}} \tag{2.14}$$

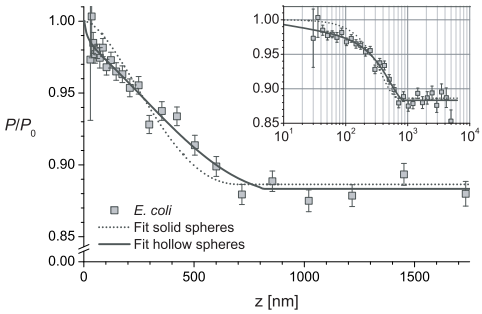

Figure 2.10: SESANS measurement of *E. coli* and fit curves for solid and hollow spheres. The inset shows the same data on a log-scale.

For solid spherical particles of ≈150 nm the correlation length was ξ_{SS}=110 nm, yielding $|\Delta\rho_{\mathrm{s}}|$=1.9·$10^{-4}$ nm^{-2}, which was a factor 3.6 smaller than the H_2O–D_2O SLD-difference. For hollow spheres of outer diameter ≈150 nm and shell thickness ≈5 nm, the correlation length $\xi_{\mathrm{HS}} \approx 25$ nm, which gave $|\Delta\rho_{\mathrm{s}}|$=4.1·$10^{-4}$ nm^{-2}, a factor 1.5 smaller than calculated between membrane and D_2O. The scattered intensity therefore supported the notion that liposomes were better described as hollow than as solid spheres.

E. coli

About four times more concentrated than the liposome samples, the *E. coli* suspension in D_2O exhibited an equally larger scattering power. In spite of only six hours measurement time, an adequate SESANS signal quality could therefore be reached. The polarization saturated around 88% at spin-echo lengths above 700 to 800 nm, as shown in figure 2.10. Considering the *E. coli* as solid spherical particles of ≈750 nm gave a correlation length ξ_{SS} ≈560 nm, yielding $|\Delta\rho_{\mathrm{s}}|$=0.80·$10^{-4}$ nm^{-2}, which was a factor 8.6 smaller than the H_2O–D_2O SLD-difference. For hollow spheres of outer diameter ≈750 nm and shell thickness ≈5 nm, the correlation length ξ_{HS} ≈35 nm, which gave $|\Delta\rho_{\mathrm{s}}|$=3.3·$10^{-4}$ nm^{-2}, a factor 1.8 smaller than calculated between membrane and D_2O. The amount of scattering therefore indicated that modeling *E. coli* as hollow spheres was more appropriate than as solid spheres.

Curve fitting

Describing the SESANS liposome data with the solid sphere model gave reasonable fits, yielding an effective size of 120 nm for both batches with a relative error of 8%, see table 2.4. Fitting the hollow sphere model to the data produced an apparently better fit for DSPC and worse for DPPC liposomes, with diameters of 150 and 170 nm and shell thicknesses around 10 nm, as shown in table 2.4. The relative errors were 7% and 15% for the diameters and 40% and 90% for the shell thicknesses, showing that the data were not very sensitive for T. This was supported by the small correlations of T with the other param-

Parameter	DSPC liposomes		DPPC liposomes		*E. coli*	
	Solid sphere	Hollow sphere	Solid sphere	Hollow sphere	Solid sphere	Filled sphere
P_{sat} [%]	96.5 ± 0.1	96.4 ± 0.1	96.6 ± 0.1	96.5 ± 0.1	86.6 ± 0.9	88.3 ± 0.5
D [nm]	122 ± 9	152 ± 11	121 ± 11	169 ± 25	718 ± 106	818 ± 98
T [nm]	–	13 ± 5	–	10 ± 11	–	8 ± 44
s [–]	–	–	–	–	–	0.06 ± 0.26
g.o.f.	${\chi_{58}}^2 = 2.27$	${\chi_{57}}^2 = 1.37$	${\chi_{48}}^2 = 1.38$	${\chi_{47}}^2 = 2.08$	${\chi_{28}}^2 = 3.22$	${\chi_{26}}^2 = 0.97$

Table 2.4: Fit results of SESANS measurements of liposomes and *E. coli*, modeled as solid, hollow and filled spheres. Parameters are the polarization saturation level (scattering power) and particle dimensions. Filled sphere *E. coli* values were obtained in the hollow sphere limit, with s approaching zero. Goodness-of-fit indications are given by χ^2_k, where k equals the number of measured points minus the number of fitted parameters.

eters, as seen in table 2.5, which also shows that cross correlations between parameters were acceptably low for both models. The largest interdependency was observed between the saturation level P_{sat} and the particle diameter D, which were connected through the correlation length.

Modeling the *E. coli* data as monodisperse, solid spheres produced a diameter of 720 nm with a relative error of 15%, but did not capture the initial decay of the measured data, see figure 2.10. The hollow sphere model seemed to produce better fits, with a sharper initial decay. Minimizing ${\chi_{27}}^2$ to 1.51 produced a saturation level P_{sat}=0.885±0.007, an outer diameter D=815±133 nm, but an unphysical shell thickness of T=120±30 nm. These hollow sphere values are not shown in table 2.4. Using the filled sphere model helped to avoid this pitfall, producing the same saturation level and outer diameter, as well as a realistic shell thickness. The extra degree of freedom in this model was parameter s, the ratio between the $\Delta\rho_{\mathrm{s}}$ values of the core and the shell, both with respect to the medium. A jump in the value for T to the unphysical range appeared when s<0.0735, which was established by fitting with s fixed increasingly closer to zero.

As shown in table 2.4, fitting with filled spheres without constraints produced a physical but imprecise value of T=7.7±43.5 nm. The value s=0.064 was small enough to effectively represent a hollow sphere, as the core–medium contrast had a negligible contribution to the overall 3-phase contrast, corresponding to a mere 3.6‰ of the shell–medium contrast. Since the hollow and filled sphere models gave identical curves at these parameter values, these *E. coli* dimensions were taken as an appropriate fit. Relative errors of the diameter and shell thickness were 12% and 565%, with small correlations between T and the rest of the model. The very large uncertainty for T meant, that even though T could be established to be small compared to D, it could not be quantified

Parameter	DSPC liposomes					DPPC liposomes					*E. coli*				
	Solid sphere		Hollow sphere			Solid sphere		Hollow sphere			Solid sphere		Hollow sphere		
	P_{sat}	D	P_{sat}	D	T	P_{sat}	D	P_{sat}	D	T	P_{sat}	D	P_{sat}	D	T
P_{sat}	1	0.4	1	0.5	0.2	1	0.4	1	0.4	0.3	1	0.5	1	0.6	0.2
D	0.4	1	0.5	1	0.0	0.4	1	0.4	1	0.2	0.5	1	0.6	1	0.1
T	–	–	0.2	0.0	1	–	–	0.3	0.2	1	–	–	0.2	0.1	1

Table 2.5: Correlations between parameters of solid and hollow sphere models fitted to SESANS data of DSPC and DPPC liposomes and *E. coli* bacteria. P_{sat} is the polarisation saturation level, D is the particle diameter and T the shell thickness for hollow spheres.

accurately from this data. The cross correlations between all parameters were similar to those of the liposome fits, see table 2.5.

2.5 Discussion

2.5.1 Measurement results

The DSPC and DPPC liposomes gave close to identical fit results using the solid sphere model and similar, but less accurate fit results for the hollow sphere model. The hollow sphere model exhibited a larger sensitivity to the shorter spin-echo lengths within the resolvable range, than the solid sphere model. Therefore the differences between the hollow sphere results of DSPC and DPPC were attributed to the number of sampled spin-echo points below 150 nm. The statistical quality of the measurements did not allow for any extension of the modeling to include concentration effects, anisotropy, aspect ratios or polydispersity. The amounts of scattering from the DSPC and DPPC liposomes and from the *E. coli* cells suggested that these samples with D_2O medium were better described by hollow spheres than by solid spheres. The SESANS observations were in better agreement with the contrast between lipid membranes and D_2O than with the contrast between H_2O and D_2O. The shells with mostly hydrogen-atoms were therefore more likely enclosing D_2O-cores than H_2O-cores.

Results of curve fitting of the liposome data were ambiguous, finding a better hollow sphere fit for DSPC and a better solid sphere fit for DPPC, despite the strong similarities between the raw data of both samples. Comparison with DLS results showed best agreement between solid spheres, with diameters of 120 nm, and the modes of the size distribution at 125 nm. The hollow sphere models produced 15% and 20% larger particle sizes of 150 and 170 nm for DSPC and DPPC than the mean diameters of 130 and 140 nm as observed by DLS. However, since the DLS characterisations were performed after the SESANS measurements and liposome samples are only semi-stable, it is possible that the size distributions had shifted to somewhat smaller averages. The shell thicknesses of the hollow spheres were determined to be between

0 and 20 nm by fitting, where the data did not allow for a more accurate assessment. The findings were nevertheless in reasonable agreement with the expected value of 5 nm, which is commonly reported for the thickness of a lipid bilayer membrane without PEGylation, and with the expected value of about 10 nm for a membrane with PEG-brushes grafted to each side. *E. coli* cells are known to have a cell length of 2 µm, a diameter of 0.8 µm and a cell wall thickness of about 5 nm. The filled sphere model agreed best with these expected values close to the limit of a hollow sphere, i.e., near zero contrast between inside and outside, finding a diameter of 820±100 nm and a thickness of 8±40 nm. The large uncertainties found in the diameter and thickness were due to the aspect ratio of the rod-like bacteria and because the cell wall is sandwiched between a thin plasma membrane and a thick outer membrane capsule. Since *E. coli* multiply through cell-division, a high degree of monodispersity was expected, but this could not be confirmed with DLS due to lacking supplies of the fast degrading bacteria and their shape, which complicated analysis.

2.5.2 Outlook

When a change in SESANS curve shape and/or polarization saturation level is observed in experiments, a change in structure, concentration or contrast can in principle be deduced. It is therefore worthwhile to investigate if SESANS could be applied to study such a change in a biological system.

Liposomes can be destroyed by external factors, such as ultrasound, or taken up and broken down through endocytosis by much larger cells, such as tumor and white blood cells, or macrophages. Typical diameters of tumor cells are $5 \leq D \leq 7$ µm in rats and $10 \leq D \leq 20$ µm in humans, whereas macrophages are about 13 µm in rats and about 21 µm in humans. SESANS measurements have already been performed on tumor cells from the rat pancreatic CA20948 tumor cell line with an approximate diameter of 6 µm, but only low concentrations were available, causing too little scattering for a significant signal to be discerned. However, we can still show through a simple calculation that a change in liposome population *in situ* may constitute a noticeable signal change.

Consider a dilute system of small liposomal vesicles and of much larger cells, so it can be considered a bimodal distribution of spherical particles, say types A and B. Take their size distributions as approximately monodisperse and let A and B have similar contrasts with respect to the medium. The shape and level of a SESANS curve then depend only on whether these particles are solid or hollow in nature and on the two scattering contributions. If these contributions are not comparable, then the curve will merely show the signal of the particles which scatter the most: the presence or absence of the other particles cannot

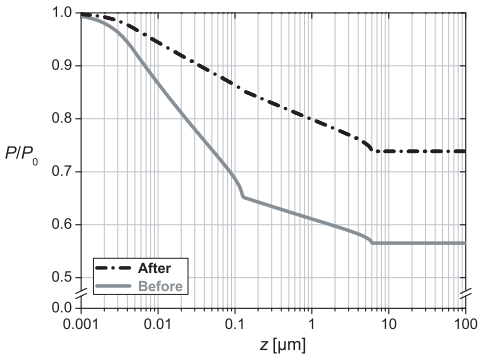

Figure 2.11: Predictive calculation of the SESANS signal of a mixed liposome and a rat tumor cell system, both modeled as hollow spheres. Signals are shown before and after decimating the liposome population, and consist of scattering contributions of both particles as well as the correlations up to spin-echo lengths z of 0.13 µm and 6.0 µm, which are the diameters used for the liposomes and the tumor cells. Further details are given in the text.

be observed. If the amounts of scattering are comparable, then the measured signal is sensitive to the removal of smaller particles from the system. This can affect both the shape of the curve, through the disappearance of a kink at the diameter of the smaller particle, and the saturation level, as the total amount of scattering is altered.

The scattering contributions for both types A and B depend on the two correlation lengths and volume fractions, and will be comparable for similar products $\phi_{\mathrm{V}}\,(1-\phi_{\mathrm{V}})\cdot\xi$. In the dilute regime cross-correlations can be neglected, which gives a simple description of the signal as

$$\frac{P}{P_0}(z) = \exp\left\{\ell\,\lambda^2\,\overline{\Delta\rho_{\mathrm{s}}}^2\left[\phi_{\mathrm{V,A}}\,\xi_{\mathrm{A}}\,(G_{\mathrm{A}}(z)-1) + \phi_{\mathrm{V,B}}\,\xi_{\mathrm{B}}\,(G_{\mathrm{B}}(z)-1)\right]\right\} \quad (2.15)$$

For solid spheres the correlation length scales with the diameter and is therefore much larger for the large particles. The correlation length of large hollow spheres is however much smaller than of small hollow spheres with the same shell thickness. An example calculation is shown in figure 2.11 for a system of 50 mg liposomes, 25 mg rat tumor cells and 5.5 grams of D_2O, corresponding to volume fractions of 1.0% and 0.5% for the liposomes and tumor cells. This gave a total sample volume of 5.0 ml. A standard sample thickness of ℓ=1.00 cm was used for the calculation and a wavelength λ=6 Å, was taken to increase signal strength. Liposomes and tumor cells were modeled as hollow spheres of 130 nm and 6 µm with a lipid bilayer membrane thickness of 5 nm, giving correlation lengths of 24 nm and 43 nm respectively. For the $\overline{\Delta\rho_{\mathrm{s}}}$ between membrane and D_2O the value $6.13{\cdot}10^{-4}$ nm^{-2} from table 2.2 was used.

The situation afterwards was calculated by removal of 90% of the liposomes, corresponding to exactly $1.8{\cdot}10^{5}$ liposomes per tumor cell. The tumor cell and D_2O fractions (mole, mass and volume), as well as the total sample volume were hardly affected with less than 1% difference and were therefore neglected. In the unlikely case of massive endocytosis by tumor cells, the tu-

mor cell volume would only change significantly when internalizing more than ~10,000 liposomes. When modelling with solid spheres about 100 times less liposomal and tumor material was required for good signal strength, but the differences before and after were much less pronounced.

2.6 Conclusions

Liposomal vesicles and *E. coli* bacteria have been observed in their entirety by SESANS. Samples have been prepared in H_2O and resuspended in D_2O; a state of relative neutron invisibility for the membrane and other cellular components, leaving solid spherical droplets of H_2O in D_2O. However, the liposomes and *E. coli* data from SESANS are better described with the projected correlation function for a hollow sphere, as they exhibit little scattering and a sharp initial decay of the polarization curves. It is therefore evident that the H_2O/D_2O-exchange has occurred before or during the initial stages of the SESANS measurements, i.e., within at most half an hour. To observe H_2O/D_2O-exchange measurement times need to be reduced drastically, requiring higher neutron fluxes, preferably in combination with a larger wavelength than available for this study. Fulfilling these prerequisites should make SESANS a viable alternative to *in vitro* tritium studies, since tritiated water has more undesirable properties than deuterated water.

Fit results using the hollow sphere model are in reasonable agreement with DLS for liposomes and in good agreement with literature on *E. coli*, but better statistics are required for accurate quantitative fitting, especially in the low spin-echo range. Although no new insights have been obtained on liposomes and *E. coli* themselves, the results constitute a proof-of-principle that SESANS is able to non-invasively observe entire microscopic biological entities with typical sizes between 50 nm and 20 µm in bulk. Under the right conditions it may be possible to observe changes in a system composed of two different biological species, as has been shown for a mix of small particles (e.g., liposomes) and large cells (e.g., tumor cells). Considerable change in signal requires great numbers of small particles to disappear per large cell. Here SESANS may be an additional tool for drug delivery studies, where liposomes are destroyed by external means to release drugs at the tumor site.

Acknowledgments

The authors thank Chris Duif (NPM^2/R^3, TU Delft, The Netherlands) for assisting with the SESANS measurements, Ulla Woroniecka (RIH/R^3, TU Delft, The Netherlands) for synthesizing liposomes, Krishna Kowlgi (DCT, TU Delft, The Netherlands) for assisting with DLS measurements and Jeroen Plomp (NPM^2/R^3, TU Delft, The Netherlands & ISIS, Oxford, United Kingdom) for checking the formula's.
This work is part of the research programme of the *Stichting voor Fundamenteel Onderzoek der Materie (FOM), which is financially supported by the Nederlandse Organisatie voor Wetenschappelijk Onderzoek (NWO).*

CHAPTER 3

Milk gelation studied with neutron scattering and simulations

Léon F. van Heijkamp, Ignatz M. de Schepper, Markus Strobl, R. Hans Tromp, Jouke R. Heringa, Wim G. Bouwman, 'Milk gelation studied with Small Angle Neutron Scattering techniques and Monte Carlo simulations', J. Phys. Chem. A **114** (2010) 2412-2426.
The symbol ϖ in this chapter corresponds to θ in the original publication.

Abstract

The sol–gel transition of fat-free milk by acidification was studied with neutron scattering experiments and Monte Carlo simulations. Spin Echo Small Angle Neutron Scattering (SESANS) and Ultra Small Angle Neutron Scattering (USANS) experiments were performed to measure the static structure of milk and yoghurt, as well as the aggregation kinetics. Colloidal gelation was simulated from a reaction limited domain (RLCA) to the diffusion limited regime (DLCA) as cluster–cluster aggregation of adhesive, hard spheres on a 3D lattice. Comparisons were drawn between experimental and numerical correlation functions. Milk was modeled as a suspension of casein micelles in water and its structure was described as a a dilute log-normal size distribution of solid spheres. The structure and formation of yoghurt were described with a self-affine model, used for systems containing heterogeneities with a wide range of sizes.

Observations by SESANS and USANS of milk particle sizes and yoghurt length scales were consistent and agreed well with literature. Kinetic USANS data yielded reliable information about the growth of typical length scale during aggregation. The simulation model predicted the measurement data qualitatively best staying close to the RLCA-regime until large structures had formed. Correlation lengths were in good quantitative agreement, but longest simulated length scales were a factor $2\frac{1}{2}$ below experimental findings. We conclude that small, mobile aggregates are formed during the first three hours, mostly influencing the dimensionality of the system and that large, inert structures are formed from two up to eight hours, which determine the typical length scale.

3.1 Introduction

It can be a challenging endeavour to observe the bulk structure of colloidal dispersions in biology and industry. Many health care and food products consist of, or are prepared from, colloids. Typical materials are often concentrated and opaque and may contain particle sizes over several orders of magnitude. Milk is such a colloidal suspension, and the formation of yoghurt from milk is hard to observe in bulk using conventional methods, such as microscopy or light scattering. Yoghurt is formed by the aggregation of milk particles suspended in water [34, 35]. Its texture is determined by the mechanism and kinetics in which the structure is formed. A gradual increase of acidity from pH=6.8 to pH≈4.5 causes the casein micelles to aggregate into large clusters, which subsequently form a percolating network [36]. Figure 3.1 depicts two casein micelles in contact. After about a half to a full day all large clusters have aggregated, forming a gel.

The aggregation of milk particles can be studied using image analysis of optical microscopy, but not inside the sample and only for a limited number of particles [37]. Conventional light scattering is also widely employed, but on extensively diluted samples. Glatter *et al.* have measured the gelation of milk by means of Dynamic Light Scattering (DLS) on very thin samples [38], which could be disputed to contain bulk information [39]. Gel formation can be measured using rheology, even though applied mechanical stress and strain disturb the developing gel [40].

Small Angle Neutron Scattering (SANS) is widely employed as a non-destructive method to measure the form factors of suspensions of mesoscopic particles. However, the scattering from particles larger than 100 nm falls within the beam stop and cannot be observed [41]. Ultra Small Angle Neutron Scattering (USANS) and Spin-Echo Small Angle Neutron Scattering (SESANS) are more suitable than SANS to study such large structures as certain colloids, gels, foams and granular matter [27, 28]. SESANS uses spin echo to encode the scattering angle. It probes density correlations in real space directly from 20 nm up to 20 µm, overlapping the resolved SANS range, but observing much larger particles. USANS provides a resolution in reciprocal space of the order of 10^{-5} Å^{-1} , which is much higher than SANS, so that intensities can be measured corresponding to µrad in scattering angles and to µm structures in real space [42]. SESANS does not suffer from the inverse relationship between measured intensity and resolution, as opposed to SANS and USANS, nor does it require beam collimation, as opposed to traditional SANS [43, 44].

Aggregation of colloidal particles can be numerically simulated in 3D as random movements on a grid of clusters of hard spheres, which may bond

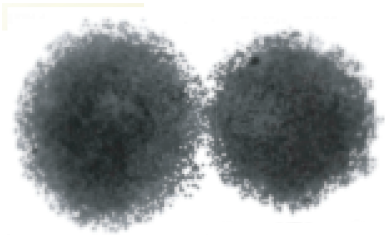

Figure 3.1: Cartoon of two casein micelles coming into contact. Because of a short-range repulsive interaction, these micelles behave like hard spheres. An increase in acidity, heat or enzymatic activity can destabilize the micelles, weakening their repulsion. Mutual contact then leads to bonding, causing aggregation and eventually flocculation of the suspension.

when occupying neighboring positions. Much work has been done on Diffusion Limited Cluster–cluster Aggregation (DLCA)[45–48] by means of Monte Carlo, simulating systems with very high reactivity with respect to the particle diffusion. During yoghurt formation however, the reactivity of the casein micelles is initially negligible and increases over time as the pH decreases. A Monte Carlo simulation of this gelation process should therefore commence in the Reaction Limited Cluster–cluster Aggregation (RLCA) domain with a time-dependent reactivity.

In this paper we present SESANS and USANS observations of the gelation of milk and Monte Carlo simulations to numerically model these observations. The bulk microstructure of casein micelles, as well as the structure and formation kinetics of yoghurt are determined experimentally, to which a log-normal distribution of solid spheres and a self-affine model are fitted respectively. An increasing reaction rate simulates the production process of actual yoghurt and the calculation of numerical correlation functions at various stages allows for comparison to the experiments.

3.2 Theory

3.2.1 The SESANS Measurement Technique

Principles

Spin-Echo Small Angle Neutron Scattering is a real space technique that measures length scales by encoding small angle scattering as depolarization. The method can be described classically by the net Larmor precession $\Delta\varphi$ [29] as figure 3.2 shows, or quantum-mechanically, by the splitting and recombination along the vertical spin-echo length z of two neutron eigenstates, due to their different interaction with a magnetic field [30, 31]. The SESANS setup consists of a monochromatic, polarized neutron beam traveling in the horizontal x-direction through two magnetic field regions, in between which a sample is

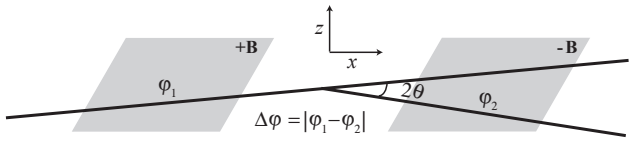

Figure 3.2: Side view schematic of the SESANS setup, consisting of two identical magnetic fields with inclined faces but opposing field-strengths **B**, through which neutrons will precess with angles φ_1 and φ_2. Diffraction of the polarized neutron beam over a sample in between the two regions over a small angle 2θ will result in $\Delta\varphi \neq 0$, measured as depolarization.

placed. Experiments are performed by varying the magnetic field strength to probe correlations along z from 20 nm up to 20 µm . The technique is not sensitive to correlations in the y-direction. When neutrons are scattered over small angles by a sample, the polarization encoded by the first magnetic region cannot be fully restored by the second, resulting in apparent depolarization of the beam. The measured polarization P is normalized with the empty beam polarization P_0. The normalized polarization depends on the coherently scattered fraction $\Sigma\,\ell$ of the beam when traversing a path length ℓ equal to the sample thickness, and on the normalized, dimensionless function $G(z)$:

$$\frac{P}{P_0}(z) = \mathrm{e}^{\,\Sigma\,\ell\,\left(G(z)-1\right)}. \tag{3.1}$$

The polarization signal saturates when long-range correlations in a sample disappear beyond distances z_{sat}, with $G(z \geq z_{\mathrm{sat}}) = 0$. Here the beam fraction retaining polarization is equal to the probability for a neutron not to scatter:

$$P_{\mathrm{sat}} \equiv \lim_{z\to\infty} \frac{P}{P_0}(z) = \frac{P}{P_0}(z_{\mathrm{sat}}) = \mathrm{e}^{\,-\Sigma\,\ell}. \tag{3.2}$$

$G(z)$ is a measure of the microstructure. It can be shown that $G(z)$ is the projection along the neutron beam of the correlation function of the sample densities [32, 49]. Since these are commutative operations, $G(z)$ is also the projection of the density auto-correlation function $\gamma(x, y, z)$. This correlation function is symmetric by definition and the SESANS technique is not sensitive to the y-component, so that

$$G(z) = \frac{2}{\xi}\int_0^\infty \gamma(x, 0, z)\,\mathrm{d}x, \tag{3.3}$$

where $G(z)$ is normalized with the correlation length ξ

$$\xi \equiv 2\int_0^\infty \gamma(x, 0, 0)\,\mathrm{d}x. \tag{3.4}$$

The correlation length can be interpreted as the chord length of a phase, i.e., the average length that neutrons travel through a phase of a structure before encountering another phase. Since movements of large colloidal particles in a solute are negligible with respect to neutron speeds, we assume that the density correlation function is independent of time [50]. The scattering length density ρ_s (SLD) has units of inverse area and is defined as the total coherent scattering length of a phase divided by its volume, so that $\rho_\mathrm{s} = N\, b_\mathrm{coh}$ with number density N and coherent scattering length b_coh. Scattering occurs at inhomogeneities of materials, due to their difference in ρ_s. Correlations between the SLD fluctuations in volume V at all points separated by the vector $\vec{r} = (x, y, z)$ are described by the normalized, dimensionless function $\gamma(\vec{r})$:

$$\begin{aligned}\gamma(\vec{r}) &= \frac{1}{\left\langle \Delta\rho_\mathrm{s}^2 \right\rangle} \Big\langle \Delta\rho_\mathrm{s}(0)\, \Delta\rho_\mathrm{s}(\vec{r}) \Big\rangle_V \\ &= \frac{1}{\left\langle \Delta\rho_\mathrm{s}^2 \right\rangle V} \int_V \Delta\rho_\mathrm{s}(\vec{r}\,')\, \Delta\rho_\mathrm{s}(\vec{r}\,' + \vec{r})\, \mathrm{d}\vec{r}\,'. \end{aligned} \tag{3.5}$$

The coherently scattered fraction of the beam per unit of sample thickness is

$$\Sigma = -\frac{\ln P_\mathrm{sat}}{\ell} = \lambda^2 \left\langle \Delta\rho_\mathrm{s}^2 \right\rangle \xi \tag{3.6}$$

with neutron wavelength λ and SLD variance $\left\langle \Delta\rho_\mathrm{s}^2 \right\rangle$. This variance of the density inhomogeneities is equal to the mean squared SLD fluctuation $\left\langle \rho_\mathrm{s}^2 \right\rangle - \left\langle \rho_\mathrm{s} \right\rangle^2$, which is related to the chemical composition. In binary systems, solely to be considered henceforth, it reduces to $\left\langle \Delta\rho_\mathrm{s}^2 \right\rangle \overset{\text{binary}}{=} \phi_\mathrm{V}(1-\phi_\mathrm{V})\, \overline{\Delta\rho_\mathrm{s}}^2$ with volume fraction ϕ_V and contrast $\overline{\Delta\rho_\mathrm{s}}^2$, which is the squared average SLD-difference. For isotropic systems, $\vec{r}$ reduces to the scalar distance $r = |\vec{r}|$ and the projection of $\gamma(r)$ is performed by the Abel transform:

$$G(z) \overset{\text{isotropic}}{=} \frac{2}{\xi} \int_z^\infty \frac{r}{\sqrt{r^2 - z^2}}\, \gamma(r)\, \mathrm{d}r, \tag{3.7}$$

$$\xi \overset{\text{isotropic}}{=} 2 \int_0^\infty \gamma(r)\, \mathrm{d}r. \tag{3.8}$$

In the case of dilute, monodisperse solid spheres of radius R, the correlation function $\gamma_\mathrm{SS}(r; R)$ is a third-degree polynomial [32] for $0 \leqslant r \leqslant 2R$ and zero

elsewhere:

$$\gamma_{\mathrm{SS}}(r;R) = \begin{cases} 1 - \frac{3}{2}\left(\frac{r}{2R}\right) + \frac{1}{2}\left(\frac{r}{2R}\right)^3 & \text{if } 0 \leqslant r \leqslant 2R \\ 0 & \text{if } \quad r > 2R. \end{cases} \tag{3.9}$$

The projection of $\gamma_{\mathrm{SS}}(r;R)$ is given by

$$G_{\mathrm{SS}}(z;R) = \Re\left[\left(1+\tfrac{1}{2}\zeta^2\right)\sqrt{1-\zeta^2} - 2\zeta^2\left(1-\tfrac{1}{4}\zeta^2\right) \ln\frac{1+\sqrt{1-\zeta^2}}{\zeta} \right], \tag{3.10}$$

where $\zeta = \frac{z}{2R}$. This system has a correlation length of $\xi = \frac{3}{2}R$.

Log-normal Distributions

In the case of polydisperse particles a size distribution has to be applied to either $\gamma(r;R)$ or $G(z;R)$, preferably to the latter for numerical convenience. The logarithm of the casein micelle sizes can be accurately described with a normal distribution [34] with mean μ and standard deviation σ. Applying the log-normal probability distribution function (eq. A.1) to the projected correlation function for a solid sphere (eq. 3.10) gives

$$G_{\mathrm{LN}}(z;\mu,\sigma) = \frac{1}{\sigma\sqrt{2\pi}} \int_0^{R_{\max}} \frac{G_{\mathrm{SS}}(z;R)}{R} \exp\left[-\left(\frac{\ln R - \mu}{\sigma\sqrt{2}} \right)^2 \right] \mathrm{d}R, \tag{3.11}$$

with correlation length $\xi = \frac{3}{2}\langle R\rangle$. The average radius of a log-normal distribution is $\langle R\rangle = R_0\, \mathrm{e}^{\sigma^2/2}$, with median radius $R_0 = \mathrm{e}^{\mu}$. When applying this distribution, integration must be performed up to a variable integration limit $R_{\max}$, which should be large enough to ensure that the most relevant sizes are included. $R_{\max}$ can be established from the inverse of the cumulative distribution function (see the appendix). Eq. 3.11 can be used for systems ranging from nearly monodisperse to very polydisperse, but computations can become too slow for fitting purposes. For SESANS measurements this approach works for average radii up to only several micrometers.

A more robust expression can be derived to tackle the problem of the variable integration limit. Substitution of R by $\frac{z}{2\zeta}$ gives:

$$G_{\mathrm{LN}}(z:\mu,\sigma) = \frac{1}{\sigma\sqrt{2\pi}} \int_{\zeta_{\min}}^{1} G_{\mathrm{SS}}(2\zeta;1) \exp\left\{ -\left[\left(\frac{\ln\frac{z}{2\zeta} - \mu}{\sigma\sqrt{2}} \right)^2 + \ln\zeta \right] \right\} \mathrm{d}\zeta, \tag{3.12}$$

thereby reducing the integration range and the effect of the singularity at $R{=}0$ (see the appendix). The lower integration limit $\zeta_{\min} \neq 0$ may be as small as 10^{-307}, depending on available numerical accuracy. Not only is this method

faster, it can also handle an extremely wide range of distributions, from atomic to macroscopic, with half-widths at half-maximum from 0.05 Å to ~1 cm. For SESANS purposes this is anything wider than a δ-peak.

Self-affine materials

Yoghurt is a bi-continuous gel with both solid and liquid characteristics, as it consists of a continuous water phase and a continuous solid phase. It is formed by acidification of milk, which causes aggregation of the milk protein micelles. During flocculation, large micelle clusters form in the continuous water phase, which grow and attach to one another without sedimentation. At a certain point, a percolating network forms, causing a phase inversion as the solid phase becomes continuous. Finally, all remaining clusters will attach to the network to form a jammed configuration and complete the sol-gel transition. On a macroscopic scale yoghurt appears to be a homogeneous substance.

However, Confocal Scanning Laser Microscopy reveals the microstructure of yoghurt to be strongly inhomogeneous, consisting of branched chains. Figure 3.3 shows the continuous protein network to resemble a sponge with pores of many sizes, encapsulating the water-phase. Casein micelles are transported by Brownian motion and need to come into contact in order to cluster. The speed of the aggregation process depends on the number of collisions and the amount required for clustering. The gel time is therefore determined by reactivity and diffusion. Considering constant temperature, and thus fixed viscosity of water, and assuming equal composition for all micelles, the transport of a casein micelle is determined by its mass.

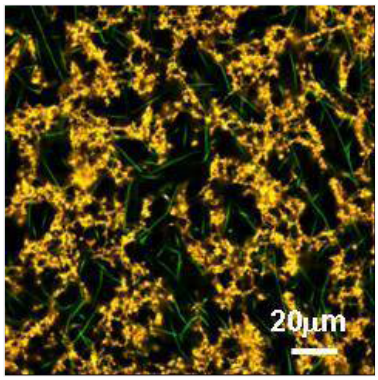

Figure 3.3: Yoghurt as seen through a Confocal Scanning Laser Microscope. The solid phase is a sponge-like protein network, constructed out of clusters of casein micelles. The continuous water phase is contained in the pores of the solid framework, creating a bi-continuous gel with both solid and liquid characteristics.

Colloidal particles can aggregate through nucleation into fractals. These structures have a non-Euclidean geometry and are self-similar, meaning that for a wide range of length scales their pieces can be rescaled and reoriented to resemble the larger whole. Because of this scale-invariance, the mass of these fractals propagates as a powerlaw through the enveloping space. The density of clusters formed from micelle monomers is therefore $\rho(r) \propto r^{d_F - d_E}$ with Hausdorff dimension d_F inside envelope space d_E. The Hausdorff dimension is $0 \leq d_F \leq d_E$ and not necessarily integer, hence the name fractal dimension. The fractal dimension d_F can be obtained from the number of self-similar structures

$N(\varepsilon)$ of linear size ε needed to cover the whole structure:

$$d_F = -\lim_{\varepsilon \to 0} \frac{\log N(\varepsilon)}{\log \varepsilon} \tag{3.13}$$

This opposed to the enveloping space, which has integer dimensionality $d_E \in \{0, 1, 2, 3\}$, analogous to the Euclidean objects dots, needles, membranes and spheres. To obtain bulk information on aggregating structures, 3D systems need to be considered, thus henceforth $d_E = 3$.

Self-affine materials have less stringent criteria for self-similarity. Systems containing heterogeneities with a wide range of sizes can be described with self-affine models. The density distribution of such a system is self-similar in overall appearance, but the scaling is not necessarily identical in different directions. It is nevertheless statistically identical to itself within a certain range of sizes and can therefore be described as a powerlaw with cut-offs. Cluster–cluster aggregation produces a network of clusters and pores, both of many sizes, and is thus more likely to create random self-affine structures, than the more isotropic fractal structures seen in large single clusters produced by aggregating monomers only.

The microstructure of yoghurt is formed through aggregation of clusters of micelles, which have a certain compactness and size. The dimensionality d_F of the aggregates is determined by the diffusion versus the reactivity regime. Two regimes can be distinguished:

- Diffusion Limited Aggregation (DLA) [46, 51], which forms open, tree-like structures with $d_F = 2.5$
- Reaction Limited Aggregation (RLA) [52], which forms more dense, cloud-like structures with $d_F \approx 2$,

where both values apply to 3D systems. The actual dimensionality for RLA clusters depends on how small the reactivity of monomers is compared to their diffusion, reaching Brownian diffusion trajectories with $d_F \equiv 2$ in the limit for zero reactivity. RLA clusters are more dense than DLA clusters and therefore leave larger cavities, when considering equal average densities, i.e., equal amounts of particles aggregating in equal volumes of space. RLA clusters from equal concentrations of particles are therefore overall less space filling, in spite of their higher local densities, and consequently have a lower dimensionality than DLA clusters.

Analogous to DLA and RLA, two regimes are distinguished for cluster–cluster aggregation: DLCA and RLCA, which respectively correspond to high and low reactivity for equal cluster mobility. The reactivity and initial concentration

of suspended monomers determine the distribution of cluster shapes and sizes formed during the flocculation stage and the time scale of the process. The particles are assumed to have a constant density, i.e., not to overlap when aggregating. A minimal concentration is required for a percolating structure to form; RLCA requires more monomers for percolation than DLCA, since low reactivity induces compactness of the aggregates. Conversely, at high volume fractions the configuration might already be jammed, giving an upper-limit to the suspendable concentration and drastically reducing gel time. Gimel *et al.* [46] observed this in simulations at volume fractions of monomers above 31%. A constant volume fraction in the mid-range of 10% will be assumed from now on.

No analytical expression has been derived for the correlation function $\gamma(r)$ or the projected correlation function $G(z)$ of such a system. For a pure fractal the correlation function $\gamma(r)$ is described by a powerlaw of r with power $d_F - d_E$. Self-affine systems resemble themselves on different length scales and also show a powerlaw behaviour. These media contain heterogeneities with a wide range of sizes. A self-affine model might be appropriate to model yoghurt as an isotropic random network of fractal entities. The Von Kármán correlation function describes density distributions of random self-affine media [53, 54] as

$$\gamma_{\mathrm{SA}}(r;a,H) = \frac{2}{\Gamma(H)}\left(\frac{r}{2a}\right)^{H} K_H\left(\frac{r}{a}\right) \tag{3.14}$$

with typical length a and Hurst exponent H, where K_n is the modified Bessel function of the second kind and Γ is the Gamma function. The correlation length ξ depends on a and H [32]:

$$\xi_{\mathrm{SA}} = 2\sqrt{\pi}a\,\frac{\Gamma(H+\frac{1}{2})}{\Gamma(|H|)}. \tag{3.15}$$

The Hurst exponent is half the difference between fractal dimension d_F and Euclidean dimension d_E, describing the dimensionality of 3D-systems as

$$H \overset{3\mathrm{D}}{=} \tfrac{1}{2}\,(d_F - 3)\,. \tag{3.16}$$

The analytical projection of the isotropic Von Kármán correlation function [32] is

$$G_{\mathrm{SA}}(z;a,H) = \gamma_{\mathrm{SA}}(z;a,H+\tfrac{1}{2}). \tag{3.17}$$

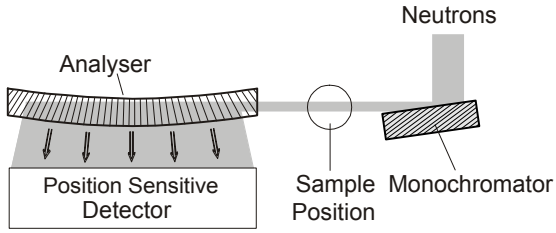

Figure 3.4: Top view schematic of the V12a USANS setup, consisting of an asymmetric perfect Silicium crystal monochromator and a completely asymmetric Silicium bent-crystal analyzer. The curvature of the analyzer causes slightly differing Bragg conditions along the crystal and therefore the neutrons are reflected with respect to their $\vec{Q}$-values. The corresponding coordinates in k-space relate to different positions in real space in the analyzer.

3.2.2 The USANS Measurement Technique

Principles

When neutrons scatter, they undergo a momentum transfer $\hbar\,\vec{Q}$. In Ultra Small Angle Neutron Scattering on an isotropic sample, the scattering is observed as broadening of the direct beam peak. Intensities are measured as a function of the wavevector transfer $\vec{Q}$ of the scattered neutrons, i.e., the resultant between the incident and scattered wavevectors. Its modulus is proportional to the sine of half the scattering angle θ

$$Q = \left|\vec{Q}\right| \equiv \left|\vec{k}_{out} - \vec{k}_{in}\right| = \frac{4\pi}{\lambda}\,\sin\frac{\theta}{2} \tag{3.18}$$

and by applying Bragg's law of diffraction to neutrons, i.e., $\lambda = 2d\,\sin\frac{\theta}{2}$ with distance d, it is evident that $Q = \frac{2\pi}{d}$ corresponds to the inverse of a typical length scale in the sample.

Figure 3.4 illustrates the V12a USANS setup, which consists of two single crystal slabs. The first is a monochromator, which reflects a wavelength symmetrically. The larger analyzer crystal is asymmetric and bent in order to reflect the intensity onto a 2-dimensional position sensitive detector (PSD). Conventional USANS setups rotate the analyzer to obtain a rocking curve. The advantage of this setup is its use of the full neutron bundle exiting the sample, thereby gaining in intensity. The instrumental resolution in $\vec{Q}$ is tunable by the curvature of the analyzer at the expense of its $\vec{Q}$-range. The disadvantages of the relatively long analyzer crystal are that it is limited to single reflections and that it induces asymmetries in the signal, mainly due to attenuation. For a monochromatic neutron beam, the intensity scattered onto the detector depends on the

microscopic differential cross-section $\frac{\mathrm{d}\sigma}{\mathrm{d}\Omega}(\vec{Q})$ [42]

$$I_{\mathrm{s}}(\vec{Q}) = c\,\frac{\mathrm{d}\sigma}{\mathrm{d}\Omega}(\vec{Q}) \tag{3.19}$$

where c is a scaling constant containing properties of the neutron beam and the sample. The cross-section is the property under investigation for any scattering experiment, giving information about the microstructure, usually by means of expressions for form and structure factors. It is also the Fourier transform of the density correlation function:

$$\frac{\mathrm{d}\sigma}{\mathrm{d}\Omega}(\vec{Q}) = \left| \int_V \Delta\rho_{\mathrm{s}}(\vec{r})\, \mathrm{e}^{\mathrm{i}\vec{Q}} \mathrm{d}\vec{r} \right|^2 = V \left\langle \Delta\rho_{\mathrm{s}}^2 \right\rangle \int_V \gamma(\vec{r})\, \mathrm{e}^{\mathrm{i}\vec{Q}} \mathrm{d}\vec{r} \tag{3.20}$$

Since USANS involves a projection of $I_{\mathrm{s}}(\vec{Q})$ and SESANS involves a projection of $\gamma(\vec{r})$, USANS measurements yield the inverse-space equivalent of the projected density correlation function $G(z)$.

Measured intensity

In USANS, the scattered intensity contains information in one direction perpendicular to the beam, with a resolved range roughly identical to SESANS. For elastic scattering, the momentum transfer is zero in the direction of the beam, so that $\vec{Q} = (Q_y, Q_z)$. The measured intensity $I_{\mathrm{m}}(Q_z)$ consists of a scattered signal, a part of the incident beam and a background contribution I_{b}, with $\Sigma\,\ell$ the scattered fraction of the incoming beam. Due to slit-height smearing, both the direct and scattered beam are projected in the y-direction and subsequently convoluted with the instrumental resolution, yielding the resolution function $R(Q_z)$ for the direct beam and $R(Q_z) \otimes I_{\mathrm{s}}(Q_z)$ for the scattered signal. The measured intensity therefore becomes [42]

$$I_{\mathrm{m}}(Q_z) = \int R(Q_z - q_z) \left[\int I_{\mathrm{s}}(\vec{q})\, \mathrm{d}q_y \right] \mathrm{d}q_z \;+\; (1 - \Sigma\,\ell)\, R(Q_z) \;+\; I_{\mathrm{b}}. \tag{3.21}$$

Scattering function

The Fourier transform of the Von Kármán correlation function (eq. 3.14) is a Lorentzian function, raised to the power $H + \frac{3}{2}$, yielding the isotropic scattering function

$$I_{\mathrm{s}}(Q; a, H) = c\,\frac{4\pi a^3\,(2H+1)}{\left[(aQ)^2 + 1\right]^{H+\frac{3}{2}}}. \tag{3.22}$$

The analytical projection of this function is facilitated by the symmetry of Lorentzians, allowing for a bisection of the integration range:

$$\bar{I}_{\mathrm{s}}(Q_z;a,H) = 2\int_0^\infty I_{\mathrm{s}}(\sqrt{{q_y}^2+{Q_z}^2})\,\mathrm{d}q_y = \frac{\sqrt{\pi}}{a}\,\frac{\Gamma(H+1)}{\Gamma(H+\frac{3}{2})}\,I_{\mathrm{s}}(Q_z;a,H-\tfrac{1}{2}) \quad (3.23)$$

Data analysis

The reduced measured data can be described with a length scale a, dimensionality H and scattered fraction $\Sigma\ell$, the latter which can be (optionally) expressed as function of a and H if the contrast of the sample is known. For a given background level I_{b} and using the convolution of $\bar{I}_{\mathrm{s}}(Q_z;a,H)$ with $R(Q_z)$, the fitting expression becomes:

$$I_{\mathrm{fit}}(Q_z;a,H) = \Sigma\ell\, I_0(a,H)\, I_{\mathrm{conv}}(Q_z;a,H) + (1-\Sigma\ell)\, R(Q_z) + I_{\mathrm{b}}, \quad (3.24)$$

showing the convoluted scattered intensity, part direct beam and background. The prefactor can be calculated from

$$I_0(a,H) = \frac{\int_0^\infty R(Q_z)\,\mathrm{d}Q_z}{\int_0^\infty I_{\mathrm{conv}}(Q_z;a,H)\,\mathrm{d}Q_z} \quad (3.25)$$

where

$$I_{\mathrm{conv}}(Q_z;a,H) = \int_{-\infty}^{\infty} \frac{R(Q_z-q_z)}{\left[(a\,q_z)^2+1\right]^{H+1}}\mathrm{d}q_z \quad (3.26)$$

where $I_0(a,H)$ has replaced $c\,4\pi^{\frac{3}{2}}\,a^2\,(2H+1)\,\Gamma(H+1)/\Gamma(H+\frac{3}{2})$. These prefactors have been expressed in eq. 3.25 as a function of the scattered fraction and the attenuation, which is the loss of total signal intensity as the neutrons pass through the sample. The attenuation is derived by normalization of the measured intensities $I_{\mathrm{sample}}(Q_z)$ with the sample transmission, i.e., $I_{\mathrm{m}}(Q_z) \equiv I_{\mathrm{sample}}(Q_z)/T_{\mathrm{sample}}$. T_{sample} is the ratio between the total intensities of the sample and of the medium only. All this results in equal total intensities for the measured signal and the resolution curve:

$$\int_0^\infty I_{\mathrm{m}}(Q_z)\,\mathrm{d}Q_z = \int_0^\infty R(Q_z)\,\mathrm{d}Q_z. \quad (3.27)$$

By substituting eq. 3.21 into this relation, and using equations 3.22 and 3.23 for the projection of the scattering function, expression eq. 3.25 remained for the prefactors after some rearranging. The Q_z-dependent part of the convolution was written as eq. 3.26 for notational convenience.

3.2.3 Simulation Model

Principles

The gelation process of milk to yoghurt can be described as colloidal aggregation of adhesive hard spheres [55]. A numerical model employing Monte Carlo simulations has been devised by Gimel and co-workers [45–48], in which the reactivity is fixed at a high value compared to diffusion, corresponding to a DLCA regime. Milk gelation does not occur at high reactivity however, as the pH decreases only gradually. Figure 3.5 shows that cluster–cluster aggregation in a reaction limited domain produces a structure, which seems to correspond well with the structure of yoghurt. In doing so, the system evolves initially in an RLCA domain, but can finish up in a DLCA regime at the end of the simulation, having had similar timescales for clustering and cluster transport at some point in between. Figure 3.6 shows two resulting structures using two different conditions for the reactivity.

Density correlation functions can be calculated from the simulated structures for the discrete case in accordance with eq. 3.5, where integration is replaced by summation. These can subsequently be compared to the measured structures and kinetics of the dairy formation. The simulation model consists of N_0 monomer particles, which are randomly placed on a grid with N sites, allowing no overlap. Each monomer is assigned unit scattering length density and the dispersion medium is described as vacuum. The average SLD of the system is then identical to the fraction $\phi_{\mathrm{N}} = N_0/N$ and the density distribution of the simulation box is

$$\rho_{\mathrm{s}}(x,y,z) = \begin{cases} 1 & \text{if occupied (at } N_0 \text{ sites)} \\ 0 & \text{if empty (at } N - N_0 \text{ sites).} \end{cases} \tag{3.28}$$

The simulation box consists of a lattice of $N = L_x \times L_y \times L_z$ sites with Periodic Boundary Conditions (PBC). The correlation function of all directions becomes

$$\gamma(x,y,z) = \frac{1}{1-\phi_{\mathrm{N}}}\left[\frac{1}{N_0}C(x,y,z) - \phi_{\mathrm{N}}\right], \tag{3.29}$$

where $C(x,y,z)$ is evaluated along the discrete grid axes of L sites

$$C(x,y,z) = \frac{1}{V}\sum_{x'=1}^{L_x}\sum_{y'=1}^{L_y}\sum_{z'=1}^{L_z}\rho_{\mathrm{s}}(x',y',z')\rho_{\mathrm{s}}(x'+x,y'+y,z'+z)\Delta x'\Delta y'\Delta z'. \tag{3.30}$$

The system volume is $V = N\Delta x\Delta y\Delta z$, where Δx, Δy and Δz define the grid spacing and are measures of length. For single unit spacings in all three direc-

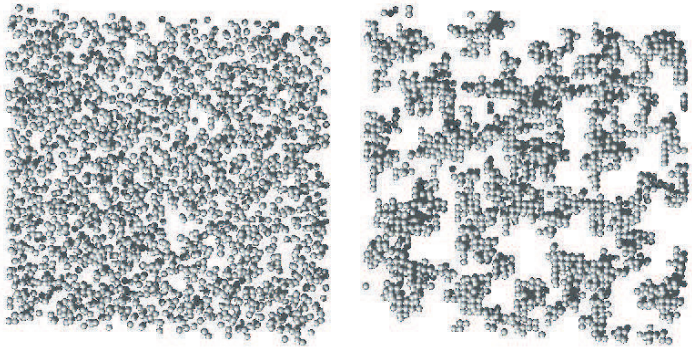

Figure 3.5: Box slabs before and after simulation using $\varpi = 10^6$, showing spatial configurations of the adhesive hard spheres. Compare the simulated structure to figure 3.3.

tions, the system volume V equals the number of sites N and the occupied volume fraction $\phi_{\mathrm{V}} = \phi_{\mathrm{N}}$. The isotropic function $\gamma(r)$ is obtained from a spline fit of the radial average of $\gamma(x, y, z)$, reducing the 3D function to a single curve of much higher resolution, but leaving the error undetermined. This approach assumes very little anisotropy amongst lattice directions, which is reasonable for large systems of many thousands of particles.

In order to compare simulation results with measurements, $\gamma(r)$ is projected and normalized with the correlation length, using equations 3.7 and 3.8, yielding the projected correlation function $G(z)$. Here z no longer represents the vertical direction, but any arbitrary direction, since the orientation of the box in space is undefined. It shows the simulated structure at the time of extraction and can be compared to structural information from SESANS measurements. The error in the simulated $G(z)$-curve is obtained by three separate projections of the correlation function in three orthogonal directions. Summation of $\gamma(x, y, z)$ along x, y and z yields three unique projected correlation functions, of which the normalized average corresponds to $G(z)$ and the root-mean-squared deviation is a measure for the error of $G(z)$.
The correlation length $\xi = \sum_{x=1}^{L_x} \gamma(x, 0, 0)\, \Delta x$ can also be calculated from the fluctuation formula

$$\xi = \frac{1}{N_0} \sum_{y=1}^{L_y} \sum_{z=1}^{L_z} \left\{ \sum_{x=1}^{L_x} \rho_{\mathrm{s}}(x, y, z) - L_x \phi_{\mathrm{N}} \right\}^2 , \tag{3.31}$$

shown here as obtained by projection along the x-direction. The correlation length can also be calculated by projection in the y- and z-directions with analogous expressions. For sufficiently large systems these should produce nearly equal results.

Algorithm

Each simulation cycle one out of N_c clusters is randomly selected and, depending on its size, allowed to move in a random direction. All particles within close proximity to each other are then allowed to bond irreversibly, depending on the global stickiness. Aggregation occurs when particles of different clusters bond, causing the growth of clusters and reducing their number. After that, simulated time is updated and the whole cycle is repeated. Aggregation continues until one super aggregate ($N_\mathrm{c} = 1$) remains, forming a fully gelated network. A fraction ϕ_N of the sites of the initial box is filled with monomers. The monomer diameter is equal to the distance between adjacent sites, to represent monodisperse, adhesive hard spheres. Each monomer has unit mass, so that the cluster mass M_c of a cluster is equal to its number of monomer constituents. Movement is limited to translation to an adjacent site and clustering is restricted to nearest neighbour particles on the lattice.

The dynamics [45] are expressed as the probability Ψ_move for a randomly selected cluster i of M_i monomers to move:

$$\Psi_{\mathrm{move},i} = M_i^{-\alpha}, \tag{3.32}$$

with main parameter $\alpha = \frac{1}{d_F}$, the inverse of the expected fractal dimension of the final structure. If this movement probability exceeds a random number between 0 and 1, the selected cluster will move in a random direction. In total three random numbers are required for the movement procedure: selecting a cluster, deciding if it moves and selecting a direction. On contact, particles can link irreversibly, determined by the probability of bonding Ψ_bond, or stickiness. In reality, the reaction rate depends on the acidity, which increases over time as the pH decreases. We have therefore made the stickiness dependent on simulated time. The rate of increase of stickiness is controlled by the second main parameter ϖ:

$$\Psi_\mathrm{bond}(t) = 1 - \mathrm{e}^{-t/\varpi}. \tag{3.33}$$

The stickiness is set globally for all clusters, but whether or not a pair of adjacent clusters will bond is determined at random. For each pair of neighbours a random number between 0 and 1 is selected and if the global stickiness exceeds this number, bonding will occur. The stickiness can increase from close to Ψ_min =0% (RLCA) to Ψ_max =100% (DLCA), corresponding to reaction times for particle bonding which are respectively much slower and much faster than transport. These limits are adjustable by writing eq. 3.33 as $\Psi_\mathrm{bond}(t) = \Psi_\mathrm{max} + (\Psi_\mathrm{min} - \Psi_\mathrm{max})\ \mathrm{e}^{-t/\varpi}$.

The algorithm for the simulation time t_{sim} uses an increasing time step per simulation cycle, labeled n_{step}

$$\Delta t_{\mathrm{sim}} = \frac{1}{N_{\mathrm{c}}}, \tag{3.34}$$

where N_{c} is the number of clusters present. As the simulation progresses, the number of clusters decreases due to aggregation and each remaining cluster is more frequently selected for movement. The simulation time algorithm takes this into account and compensates by increasing the time step, thus ensuring that clusters of constant size have constant diffusion.

A neighbourhood list, which keeps track of the direct surroundings of each particle, is employed to reduce computational time by one order of magnitude. It eliminates the need to loop over all particle pairs during each step, when investigating if a site is available for movement or occupied with a candidate for bonding. Large clusters have a rather small probability to move. Thus, for a system with relatively large clusters, it may take many evaluated steps before any movement occurs, hence resulting in a large amount of dead time. To save another order of magnitude in computational time, we have devised an additional algorithm to calculate the probability $\Psi_{\mathrm{dead}}(n)$ that in the next n steps no movements occur from the cluster-size distribution. Eq. 3.32 gives the probability for a single cluster to move in any single step, from which it follows that the probability that no clusters move is

$$\Psi_{\mathrm{dead}}(1) \;=\; 1 - \sum_{i=1}^{N_{\mathrm{c}}} \frac{\Psi_{\mathrm{move},i}}{N_{\mathrm{c}}} \;=\; 1 - \sum_{i=1}^{N_{\mathrm{c}}} \frac{M_i^{-\alpha}}{N_{\mathrm{c}}}. \tag{3.35}$$

It follows that the probability that none have moved after n steps is

$$\Psi_{\mathrm{dead}}(n) \;=\; \left(1 - \sum_{i=1}^{N_{\mathrm{c}}} \frac{M_i^{-\alpha}}{N_{\mathrm{c}}}\right)^n. \tag{3.36}$$

Comparing $\Psi_{\mathrm{dead}}(n)$ to a random number $0 \leq Q_1 \leq 1$ yields the number of steps n_{skip} to be skipped, after which the movement of a certain cluster is to be enforced:

$$\Psi_{\mathrm{dead}}(n_{\mathrm{skip}}) \;\geq\; Q_1 \Leftrightarrow n_{\mathrm{skip}} \;=\; \left\lceil \log Q / \log\left(1 - \sum_{i=1}^{N_{\mathrm{c}}} \frac{M_i^{-\alpha}}{N_{\mathrm{c}}}\right) \right\rceil. \tag{3.37}$$

We have imposed that, after skipping n_{skip} steps, the total probability is 100% that a cluster moves. The probability that cluster j moves at that moment, is equal to its probability of moving in a single step, normalized with the total

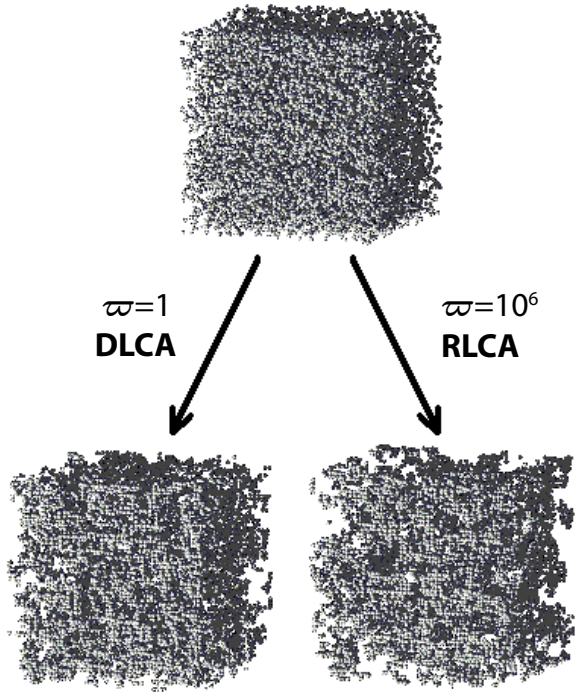

Figure 3.6: Simulation boxes before (top) and after gelation. ϖ = 1 corresponds to Diffusion Limited Cluster Aggregation (bottom left), whilst ϖ =10^6 corresponds to Reaction Limited Cluster Aggregation (bottom right). Notice the larger pores in the RLCA structure.

probability of any cluster moving in a single step:

$$\Psi_{\mathrm{move},j}(n_{\mathrm{skip}}) \;=\; \frac{M_j^{-\alpha}}{\sum_{i=1}^{N_\mathrm{c}} M_i^{-\alpha}}. \tag{3.38}$$

The cluster j to be moved can now be determined by comparison of the cumulative probability over the set of clusters to a second random number $0 \leq Q_2 \leq 1$

$$\sum_{i=1}^{j} \Psi_{\mathrm{move},i}(n_{\mathrm{skip}}) \;\geq\; Q_2 \;\Rightarrow\; j, \tag{3.39}$$

yielding cluster label j. Movement in a random direction requires a third random number, just as in the original cluster movement procedure.

3.3 Experimental

3.3.1 Sample preparation

Deuterated fat-free milk samples were prepared at room temperature by suspending 10.0 wt.% NILAC milk powder in D_2O. The milk powder consisted for 30% out of casein proteins, of which a large majority (80–90%) formed micelles with a hydrated density of about 25 mg/l. The volume fraction of casein micelles in the prepared milk samples was therefore roughly ϕ_V=10%. Cuvettes of 10×18 mm transection were filled up to about 1.5 cm. The biological process of milk to yoghurt coagulation with bacteria did not work well in D_2O. Therefore, coagulation was induced by addition and gentle mixing of 2.5 wt.% glucone-δ-lactone (GDL), which dissociated gradually during a few hours until the acidity (pD) reached ≈4.5, similar to the pH value expected for the same concentration of GDL in H_2O. Due to sample size limitations, it proved difficult to establish the acidity accurately during the process. No data was available on the dissociation of GDL in D_2O, which is less acidic than H_2O, with pD=7.43 [56] at 25°C. The yoghurt samples fully gelated after half a day at room temperature [43]. GDL concentrations of 1.7 and 3.8 wt.% were also used to investigate the sensitivity of the structure for acidity deviations.

3.3.2 SESANS measurements

The bulk structure of milk particles before and after gelation was measured statically with the SESANS setup at the Reactor Institute Delft, The Netherlands. Deuterated milk and yoghurt samples of 18.0 mm thickness were scanned during about a day with a wavelength λ=2.09±0.04 Å at spin-echo lengths of up to 5 µm for the milk and up to 12 µm for the yoghurt. Model parameters were fitted to $\frac{P}{P_0}(z)$measurement data using eq. 3.1 with models for the correlation function $G(z)$. Curve fitting consisted of non-linear least squares regression with 95% confidence bounds, i.e., a likelihood within two standard deviations of the measurement data.

SESANS measurements of milk were described using model correlation functions for a dilute system of homogeneous, solid spheres. Given the typical sizes of the milk micelles, the measurements provided information about the average scattering length density over the space occupied by the micelles. The inhomogeneities in their internal structure were outside the resolvable range of SESANS and excluded from modeling. Both the monodisperse and the polydisperse case were investigated, using $G_{\mathrm{SS}}(z;R)$ for spheres of radius R (eq. 3.10) and $G_{\mathrm{LN}}(z;\mu,\sigma)$ for spheres with a log-normal distribution of sizes, determined by μ and σ (eq. 3.12). The self-affine model $G_{\mathrm{SA}}(z;a,H)$ was fitted to SESANS data on yoghurt, yielding length scale and dimensionality (eq. 3.17).

An attempt was made to follow the coagulation process by time-resolved measurements of the polarisation at z-values of 70 nm, 300 nm, 1000 nm and 3000 nm. The neutron flux of the 2 MW Delft reactor did not provide an acceptable time-resolution however. It was therefore decided to perform the kinetic experiments using the USANS setup at the Helmholtz Centre Berlin, possessing a 10 MW reactor, which assured a large improvement in time-resolution. The SESANS and USANS techniques had roughly identical resolving ranges and yielded the same information on microstructure.

3.3.3 USANS measurements

All USANS measurements were performed on the V12a double crystal diffractometer [57] at the HMI in Berlin, Germany. A sample thickness of ℓ=10.0 mm and a neutron wavelength $\lambda = 4.76$ Å were used. GDL was added at time 0 hours to commence the gelation process and the structure was measured for 10 minutes per snapshot. The bulk structure of the dairy samples was statically measured before and after gelation over periods of 1.0 and 1.5 hours respectively, and scaled afterwards to 10 minute signals.

Raw 2D data was summed along the detector columns and corrected for the transmission profile of the analyzer crystal, after which the background was subtracted. The reduced data curves only contained information in the positive Q_z-range. All curves were normalized with the sample transmission, in order to obtain integral intensities equal to the resolution curve area. A non-scattering reference sample, consisting of 10.0 mm D_2O, was measured for 1 hour and reduced to obtain the resolution curve $R(Q_z)$ and background level I_b, which were needed to evaluate eq. 3.21. The computational shape of $R(Q_z)$ was determined for negative and positive Q_z-range separately (see the appendix). The background $I_\mathrm{b} = 40 \pm 3$ [counts/10min.] was calculated from the average intensity in the tail of the curve, between $0.0050 \leq Q_z \leq 0.0182$ nm^{-1}.

3.3.4 Simulations

The simulation boxes consisted of a distribution of empty and occupied sites. The density correlation function $\gamma(x, y, z)$ was calculated by summation of the product of a box with a copy shifted along (x, y, z) using PBC. The projected correlation function $G(z)$ was extracted from a spline fit through the radial average $\gamma(r)$ and a consecutive Abel transform. The error in $G(z)$ was obtained from the standard deviation of single summations of $\gamma(x, y, z)$ in the x-, y- and z-directions, taking the root-mean-squared deviation of these projections from their average.

Runs were performed on cubic systems of $50 \times 50 \times 50$ grid points, using a particle diameter D of 1 grid unit with 10% of the sites occupied. The start-

ing configurations consisted of a uniform distribution of 12,500 non-overlapping monomers, where the occupied sites were randomly chosen. Initial runs showed that finite size effects did not contribute significantly to the development of structures in systems containing in excess of 10,000 particles. The final structures had dimensionalities around 2 and therefore a fixed value of $\alpha = 0.5$ was used for the parameter controlling the diffusion. In this range, small variations of α have nearly no influence on the kinetics [45, 46, 58].

All simulation runs were performed without any initial reactivity. Three cases were examined for the increase of reactivity from RLCA to DLCA: an instantaneous transition ($\lim \varpi \downarrow 0$), an intermediate transition and the case where the system never left the RLCA regime ($\lim \varpi \to \infty$). For systems above 10,000 particles this transition did not depend on system size and these three cases corresponded to $\varpi \sim 10^0$, $\varpi \sim 10^3$ and $\varpi \sim 10^6$. Figure 3.6 shows the initial box and two configurations resulting from the smallest and largest ϖ value used. The influence of the degrees of freedom for movement and bonding on the structures were also investigated. Several smaller runs were performed with both parameters varied between $\{6, 18, 26\}$ directions and $\{\sqrt{1}, \sqrt{2}, \sqrt{3}\}$ bond lengths respectively, corresponding to the nearest neighbours in body-centered cubic stackings. These simulations will be discussed in more detail in a future publication by this author.

3.4 Results

3.4.1 SESANS Results

Static measurements

Figure 3.7 shows SESANS polarization data and fitted curves, revealing the structure of deuterated milk and yoghurt samples. Both measured curves had approximately equal initial slopes. The amount of scattering Σ increased by a factor 3.2, easily calculated from the drop in saturation level P_{sat}. However the spin-echo lengths z_{sat}, where the polarization signals began to saturate, increased from 250 nm to ~5 µm, indicating that the largest sizes with a relevant contribution to the signal increased by a factor 20.

The slope of the approximately linearly decaying part of a SESANS curve can be shown to be proportional to Σ/ξ [32]. Since SESANS uses a monochromatic neutron beam, this part of the curve relies on the chemical composition $\left\langle \Delta\rho_{\mathrm{s}}^2 \right\rangle$. The measurements therefore indicate a similarity in the overall composition of the isolated casein micelles in milk and the aggregated micelles in yoghurt, from which it follows that the correlation lengths ξ are directly proportional to the

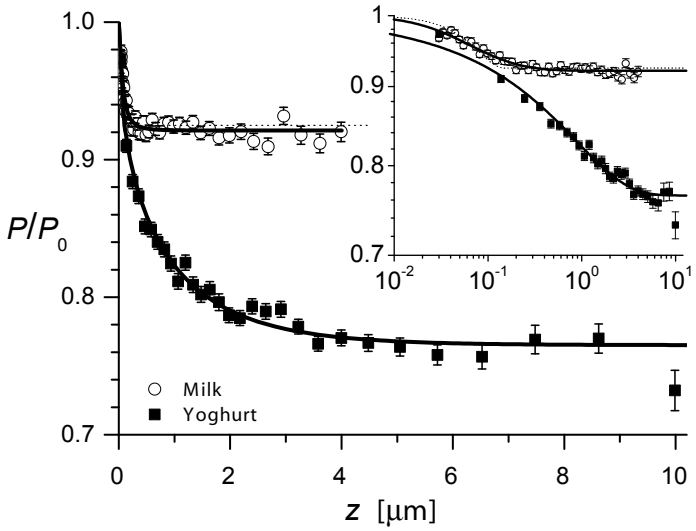

Figure 3.7: Static measurements on deuterated milk and yoghurt. Top dotted and solid lines are the solid sphere and log-normal fit for milk; bottom solid line the self-affine model for yoghurt. The inset shows the same data on a log-log scale. The initial decay shows similar behaviour in both curves.

amount of scattering. This typical length scale merely increases by a factor 3.2, as opposed to the factor 20 for largest sizes present in the samples.

Log-normal fit of milk measurements

The correlation function of dilute, solid spheres (eq. 3.10) was fit to measurement data for radius R and saturation level P_{sat}. These two parameters determined the width and the height of the curve respectively, and were not strongly correlated. Since casein micelles have been reported with average radii between 100 and 120 nm in domains ranging from 30 to 300 nm [34], a better result was achieved using a projected correlation function $G_{\mathrm{LN}}(z;\mu,\sigma)$ (eq. 3.12) for a log-normal distribution of solid spheres. Results for both cases are listed in table 3.1.

The mean μ and standard deviation σ of the natural logarithm of the distribution, mostly determined the peak-position and the distribution-width respectively (see the appendix). Both parameters determined the width and decay of the measured polarization curve, whereas the height only depended on the saturation level P_{sat}. The three parameters in this model did not show strong correlations with one-another. A weak correlation was observed between μ and P_{sat}; presumably due to their dependency on the correlation length ξ, whereas

	Monodisperse solid spheres	Log-normal distribution	Log-normal NIZO sample
P_{sat} [%]	92.5 ± 0.3	92.1 ± 0.2	91.9 ± 0.2
R [nm]	75.7 ± 7.6	–	–
μ	–	4.38 ± 0.10	4.59 ± 0.06
σ	–	0.89 ± 0.20	0.57 ± 0.13
g.o.f.	${\chi_{48}}^2 = 2.61$	${\chi_{47}}^2 = 1.14$	${\chi_{20}}^2 = 0.80$
$\langle R \rangle$ [nm]	76	119 ± 24	116 ± 11
PDI [%]	0	48 ± 8	33 ± 7
ξ [nm]	114 ± 11	178 ± 36	174 ± 17
Σ [m^{-1}]	4.3 ± 0.2	4.6 ± 0.1	4.7 ± 0.1
$\langle \Delta\rho_{\mathrm{s}}^2 \rangle$ [nm^{-4}]	$8.7{\cdot}10^{-7}$	$5.9{\cdot}10^{-7}$	$6.1{\cdot}10^{-7}$

Table 3.1: Results obtained from describing the SESANS measurements of milk samples (see fig. 3.7) as dilute, solid spheres for the monodisperse and log-normal distribution cases. Goodness- of-fit indications are given by the reduced χ^2. To check reproducibility a log-normal distribution was fitted through SESANS data from another milk sample, prepared by NIZO. Log-normal parameters have been recalculated to an average radius and polydispersity to allow comparison with the solid sphere fit, yielding the correlation length $\xi = \frac{3}{2}\langle R \rangle$, the amount of scattering $\Sigma = -\ln P_{\mathrm{sat}}/\ell$ and the SLD variance $\langle \Delta\rho_{\mathrm{s}}^2 \rangle = \Sigma / (\lambda^2 \xi)$.

	Self-affine model
P_{sat} [%]	76.5 ± 0.8
a [nm]	1524 ± 445
H	-0.28 ± 0.03
g.o.f.	${\chi_{27}}^2 = 1.97$
Σ [m^{-1}]	14.9 ± 0.6
d_F	2.44 ± 0.07
ξ [nm]	577

Table 3.2: Parameters obtained from fitting the self-affine model to the SESANS measurement of yoghurt, see figure 3.7. Goodness-of-fit indications are given by the reduced χ^2. The amount of scattering Σ was calculated from P_{sat}, the fractal dimension from H and the correlation length from Σ using the SLD variance found for milk, see table 3.1. The correlation length ξ was 3.2 times larger for yoghurt than for milk.

σ purely contained information about the occurrence of all other lengths in the sample.

Self-affine fit of yoghurt measurements

The yoghurt measurement was described with the self-affine model of eq. 3.14. The resulting values for the parameters are listed in table 3.2. The substantial uncertainty of 29% in the length scale parameter a could be explained by the somewhat large correlation with dimensionality parameter H in this model, in combination with the relatively limited number of measured data points, especially in the very short and very long z-range. Nevertheless, the scattered fraction of 27% is close to the optimum condition for SESANS measurements, regarding the signal-to-noise ratio. As can be seen from eq. 3.1, extracting $G(z)$ from the polarization involves taking the logarithm from a number between 0 and 1. Too strong a signal would therefore blow up the error bars, whereas too weak a signal would be hidden in the noise.

3.4.2 USANS Results

Kinetic measurements

The structural change of deuterated milk during gelation was measured kinetically with USANS every 10 minutes; whereas the static initial and final states

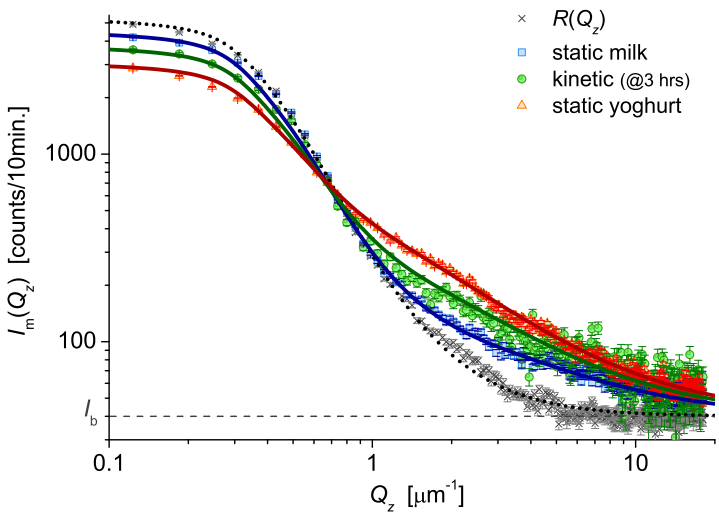

Figure 3.8: Kinetic USANS measurements on coagulation of milk to yoghurt, showing measured data and fitted curves for D_2O, the initial structure, a 10 minute scan of the structure halfway and the final structure. The static measurement times were 1.0, 1.0 and 1.5 hours respectively. The dotted line shows the resolution function $R(q)$ and the dashed line the background level I_b.

were measured for longer times to improve statistics, see figure 3.8. The USANS measurement data was reduced to a set of 92 kinetic curves and two static curves. Initially a length scale a, Hurst exponent H and scattered fraction $\Sigma\,\ell$ were fitted to these curves. However, since the amount of scattering is actually determined solely by the length scale and dimensionality of the sample, this parameter could be eliminated from fitting and $\Sigma\,\ell$ was subsequently calculated from a and H.

Self-affine fits of kinetic measurements

The USANS signals were described with the inverse space version of the self-affine model, see eq. 3.22. Curve fitting was performed using equations 3.24, 3.26, 3.25 and the resolution function $R(Q_z)$, see eq. A.9 and table A.1 in the appendix. Figures 3.9, 3.10 and 3.11 show fit results of all data sets for length scale a, Hurst exponent H and scattered fraction $\Sigma\,\ell$.

Results for a were noisy and no clear result for H was achieved for the initial data sets. The scattered fraction $\Sigma\,\ell$ was easily determined from the measurements, depending largely on the measured peak height. Data collected during the first few hours was not sensitive to the actual value of H and initial values were non-physical at $H < -\frac{1}{2}$, yielding negative scattered intensities in eq. 3.22, corresponding to negative correlations in real space, see eq. 3.14. After about 8 hours a final level of $H \approx -\frac{3}{8}$ could be reasonably well established

	static milk	kinetic (t=3 hrs)	static yoghurt
a [nm]	undetermined	543 ± 165	850 ± 100
H	undetermined	-0.39 ± 0.08	-0.38 ± 0.02
Σ [m^{-1}]	20 ± 11	33 ± 1	49 ± 1
g.o.f.	${\chi_{291}}^2 = 9.0$	${\chi_{291}}^2 = 2.4$	${\chi_{291}}^2 = 6.0$
a [nm]	276 ± 13	551 ± 18	837 ± 10
H	$-\frac{3}{8}$	$-\frac{3}{8}$	$-\frac{3}{8}$
Σ [m^{-1}]	16 ± 1	32 ± 1	49 ± 1
g.o.f.	${\chi_{293}}^2 = 9.2$	${\chi_{293}}^2 = 2.4$	${\chi_{293}}^2 = 6.0$

Table 3.3: Parameters a, H and Σ, i.e., the length scale and dimensionality of the self-affine model and the scattered fraction per unit of sample thickness, fitted to the static and kinetic USANS measurements before, during and after gelation (see fig. 3.8). Top half of the table shows results obtained by fitting with all three parameters free; the bottom half contains results fitting only for a, with fixed H and Σ expressed as a function of both. Goodness-of-fit indications are given in both cases by the reduced χ^2.

however, corresponding to a fractal dimension $d_F \approx 2\frac{1}{4}$. A much better result could be achieved by fitting with H fixed to its final value and using additional relations 3.6 and 3.15. Fitting all curves only for a with constrained H and calculated $\Sigma\,\ell$, produced the much less noisy result seen in black in figure 3.9, together with figures 3.10 and 3.11. The quality of the fits, as expressed by χ^2, was nearly identical for all 94 curves to the values found when all parameters were let free, thus demonstrating that the number of correlated parameters had been reduced with an insignificant influence on the outcome for a.

The final result was that the typical length scale a initially remained steady for two hours at 276 ± 13 nm, but increased by a factor 3.0 during the next six hours as the micelles aggregated, reaching a final value of 837 ± 10 nm.

3.4.3 Simulation Results

Structures

Runs were performed to examine the effect of different speeds for the increasing reactivity during simulation, starting with no initial stickiness. Three different cases were examined for the time-development of $\Psi_{\mathrm{bond}}(t)$: a very fast increase, a gradual increase and very little increase, corresponding to very low, medium and very high values of ϖ. In the first case, using $\varpi = 1$, the sticking probability increased quickly from 0% to 100%, rapidly moving the system from an RLCA to a DLCA regime. Medium values, such as $\varpi = 10^3$, caused a gradual increase towards 100% stickiness and the system developed from RLCA to DLCA over the entire run time. Only for very high values, such as $\varpi = 10^6$ or higher, the reactivity stayed close to 0% and the system developed well inside the RLCA domain.

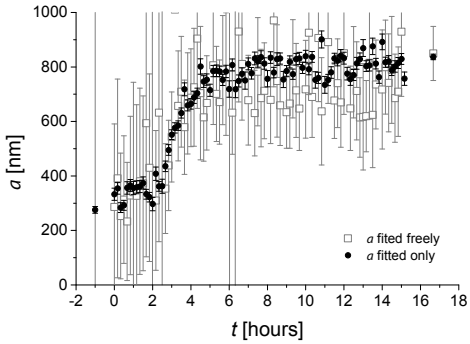

Figure 3.9: Fit results for USANS measurements showing the evolution of length scale a during aggregation. Fitting was performed for free a, H and $\Sigma\,\ell$, with a noisy result. Subsequently a was fitted with fixed $H = -\frac{3}{8}$ and $\Sigma\,\ell$ expressed as a function of a, shown in black.

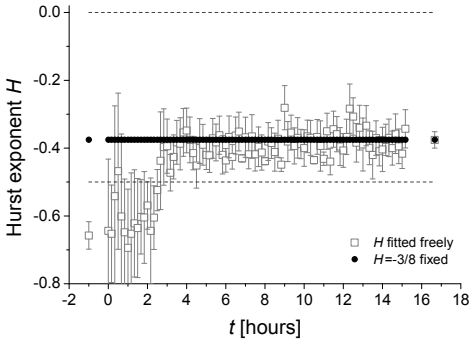

Figure 3.10: Fitted results for the dimensionality of the system during aggregation. Initial values are non-physical and fits are not sensitive to the actual value, as long as $-\frac{1}{2} \le H \le 0$. The final level at $-\frac{3}{8}$ could be quite well established however.

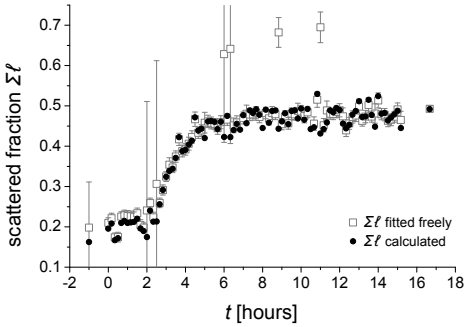

Figure 3.11: Fit results for USANS measurements showing the increase of the scattered fraction $\Sigma\ell$ of the direct beam, using a sample thickness $\ell = 1$ cm.

Figure 3.12 shows correlation functions obtained for one run with $\varpi = 1$ and one with $\varpi = 10^6$, see subplots **A** and **B**. The simulated aggregation caused an increase in both the largest contributing lengths z_{sat} and the correlation length ξ. Correlations between density fluctuations became negligible at lengths z_{sat}, the point at which a curve appeared to saturate, starting from a single monomer diameter D and growing up to at most 8 times during the simulation. The correlation length showed an increase during simulation by a factor 2.7 in the DLCA regime, but by a factor 3.2 in the RLCA domain, see table 3.4, indicating larger and denser structures for the latter. The slight broadening of the band around each consecutive curve signified an increased uncertainty in the value of $G(z)$ as the structure developed. This set of error bars was determined from the variation between three orthogonal projections of the correlation function.

	$\varpi = 1$	$\varpi = 10^6$
ξ(final)/ξ(initial)	2.7	3.2
z_{sat}(final)/z_{sat}(initial)	4	8
t_{stat} [−]	~ 50	~ 500

Table 3.4: Changes in main length scales and indication of simulation time scale from simulations in DLCA and RLCA regimes. Typical lengths are expressed by ξ, showing a vertical drop in saturation level. Longest lengths are expressed by z_{sat}, giving the distance beyond which correlations disappear.

The increase in these variations remained small however, and in this respect there was no noticeable difference between the DLCA and RLCA runs.

Time dependency

The aggregation process consisted of two stages. Initially clusters grew to larger, less mobile aggregates at the expense of small, mobile clusters. Toward the end of the simulation these large aggregates slowly formed a network by percolating the system. In order to track the evolution of correlations at different length scales, values of $G(z)$ at different z-values were plotted against simulated time t_{sim}, see subplots **C** and **D** in figure 3.12. Spin-echo lengths z/D of 0, 1, 2, 3 and 25 were selected to examine the time development of short range correlations and the longest correlation possible in a system of V = 50×50×50 D^3.

The $G_{z=0}(t_{\mathrm{sim}})$-curves showed constant monomer contributions for both regimes, because the amount of monomers did not change. Dimer ($z = D$) and trimer ($z = 2D$) correlations increased during aggregation. For four monomer correlations ($z = 3D$) a depletion effect was observed in DLCA, which was not seen in RLCA, as the curve dipped below the longest correlations ($z = 25D$) around $t_{\mathrm{sim}} = 10$. These correlations at $z = 3D$ disappeared due to initial clustering of dimers and trimers, creating more empty space around them, and reappeared as larger clusters were created, which contained all shorter range correlations from that point on. Five monomer correlations and higher ($z \geq 4D$) developed nearly equal to the largest correlations, corresponding also to the time development of the correlation length $\xi(t_{\mathrm{sim}})$. The time $t_{\mathrm{sim}} = t_{\mathrm{stat}}$ at which these $G_{z=25D}(t_{\mathrm{sim}})$ curves saturated, showed a stationary situation before actual gelation. Hence, any clustering after t_{stat} did not contribute significantly to the correlations of the system. In the DLCA regime little to no change was observed after $t_{\mathrm{stat}} \approx 50$ and for RLCA after $t_{\mathrm{stat}} \approx 500$.

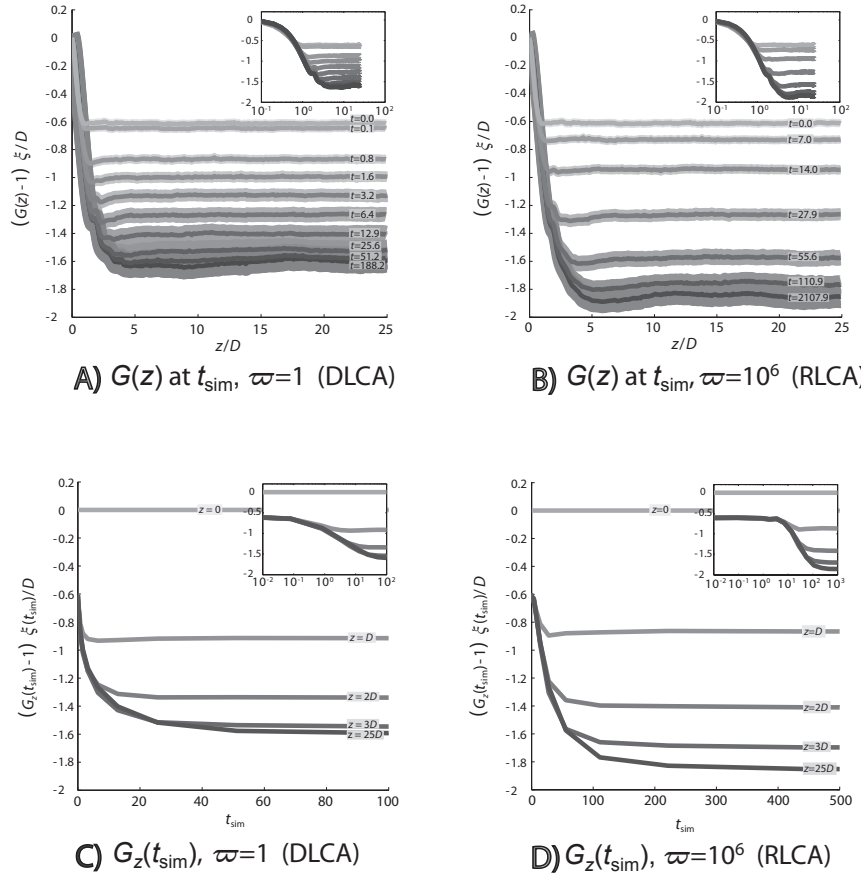

Figure 3.12: Time-evolution of $G(\mathcal{Z})$ from simulations quickly moving to a DLCA regime (left side) and staying well within the RLCA regime (right side), with insets on a semi-log scale. Top subplots show snapshots of $G(\mathcal{Z})$ labeled with the simulated time t_{sim}, which were selected for optimal clarity. Bottom subplots show the time dependency of $G(\mathcal{Z})$ for fixed values of the spin-echo length $\mathcal{Z}$. The errors in $G(\mathcal{Z})$ are presented as bands around the curves and the vertical axes show $(G-1)\ \xi/D$ to allow for easier comparison to the SESANS measurements (compare with the argument of the exponent in eq. 3.1).
Subplots **A** and **B** show how length scales develop during simulated time. Both the horizontal and vertical axes demonstrate that in RLCA larger structures develop, with larger long range correlations and a larger correlation length. Subplots **C** and **D** show the time-dependency of $G(\mathcal{Z})$ at fixed short range spin-echo lengths $\mathcal{Z}$ of 0, 1, 2, 3 D and at the longest possible correlations of $\mathcal{Z} = 25D$. Here $G_{\mathcal{Z}=25D}(t_{\mathrm{sim}})$ corresponds to $\xi(t_{\mathrm{sim}})$, shown by the dropping levels in the top row. The speed of development is expressed by the steepness of the curves in the bottom row and the time labels in the top row.

3.5 Discussion

3.5.1 Measurements

Reproducibility

Different SESANS measurements showed nearly identical results for several milk samples and similar results for yoghurt samples. The USANS measurements were performed at tenfold higher time resolution, producing results consistent with the SESANS experiments. This allowed for a kinetic investigation of the structural development during the gelation process. The consistency of SESANS with USANS results, validated the assumption made in the Theory section 3.2.1, that the correlation functions of semi-stable colloidal suspensions are independent of time.

The main issue in the reproducibility of all measurements, was the exactness of the sample preparation. Primarily, the quality of the milk powder determined both the milk and yoghurt structure. Storage under Argon-atmosphere in a glove box avoided exposure of the powder to moisture, which proved more important to prevent aging than cooling at 7°C. Of secondary importance was the sensitivity of the process to the addition and proper mixing of a precise amount of GDL and the influence of temperature on the reaction rate. Deviations within a few percent were deemed to have negligible effects on reproducibility, after comparing different samples and GDL concentrations.

SESANS on milk

Describing the SESANS measurement data for milk as a system of dilute, monodisperse solid spheres, produced a radius of about 75 nm, see table 3.1. By applying a log-normal distribution and fitting to μ and σ, an average radius of about 120 nm was achieved, with a polydispersity of almost 50%, showing that the system was far from monodisperse, see table 3.1. These results were in good quantitative agreement with literature on sedimentation field flow and dynamic light scattering [34, 35] and previous SESANS measurements [43], as well as a DLS experiment, which showed a wide distribution and a peak around 100 nm.

Previous SESANS measurements on NILAC samples prepared by NIZO [43] compared quite well, with approximately the same mean radius around 115 nm, but a narrower distribution with 33% polydispersity, most likely due to a difference in milk powder composition or sample preparation. A consistent SLD variance of $6{\cdot}10^{-7}$ nm^{-4}was found for the different milk samples. Any short-range interactions, such as an excluded volume effect for concentrations exceeding the dilute regime, would be smoothened by the the considerable polydispersity [59].

SESANS milk vs. yoghurt

Comparing the SESANS curves of milk and yoghurt, a factor 20 increase in the long length scale was observed, whereas the correlation length increased by a factor 3.2. From this it was inferred that aggregates were created about 20 micelles long, but with an average cross-section of about 3 micelles. The overall composition of these micelles was not affected by aggregation, as could be seen from the similar initial slopes of both curves, supporting the adhesive sphere model. The yoghurt was modeled as a network of fractal constituents with a density auto-correlation function $\gamma(r)$ of (eq. 3.14) containing a length scale and a dimensionality. Although for $r \ll a$ this correlation function diverges to infinity if $\frac{1}{2} \leq H \leq 0$, this small length domain is outside the SESANS resolution. More importantly, the projected correlation function $G(z)$ (eq. 3.17) does not diverge, but converges to 1 for $\lim_{r \downarrow 0}$.

SESANS vs. USANS

The milk particle size could be consistently determined with both SESANS and USANS. An average casein micelle diameter around 240 nm was observed with SESANS, with which the initial length scale found in the kinetic USANS measurements agreed reasonably well. Using the log-normal and self-affine models respectively, neither technique was able to establish the dimensionality of milk. USANS data produced unphysical values $H < -\frac{1}{2}$. However, the presumption that the density of milk particles propagates in a space-filling manner, was strengthened by fitting the self-affine model to the SESANS data, resulting in $d_F = 3$, see table 3.5.

With USANS the typical length scale of milk was observed to persist for about two hours after acidification, after which micelle coagulation caused it to increase, reaching a final size three times larger after about eight hours, see figure 3.9. After about 3 hours a constant value $d_F = 2\frac{1}{4}$ seemed to have been reached, right in between values expected for DLA and RLA clusters, as discussed in the section on self-affine materials. This indicated that the process for cluster-cluster aggregation is either somewhere in between the RLCA and DLCA regimes or that the gelation occurs in a combination of both, which was the starting hypothesis. The dimensionality of yoghurt was in good agreement with the range of values found by Vétier *et al.* for casein aggregates, in spite of their having used diluted systems [60].

However, SESANS measurements on yoghurt yielded a typical length scale two times larger with a significantly larger dimensionality, as described by the same model used for the USANS data. An alteration to this model was made, by replacing the modified Bessel function $K_H\left(\frac{r}{a}\right)$ of eq. 3.14 in section 3.2.1 with

MILK	SESANS Log-normal	SESANS Self-affine	USANS Self-Affine
a [nm]	238 ± 48	(88 ± 29)	276 ± 13
ξ [nm]	178 ± 36	(66 ± 22)	(3110 ± 146)
d_F [–]	–	3.0 ± 0.3	(2.25)
Σ/λ^2 [µm^{-3}]	105 ± 3	103 ± 3	71 ± 5
YOGHURT	Fractal Network	Self-affine	Self-affine
a [nm]	834 ± 283	(1524 ± 221)	837 ± 10
ξ [nm]	570	(211)	(9430 ± 113)
d_F [–]	2.29 ± 0.06	2.44 ± 0.07	2.25
$\Sigma/\lambda^2 2$ [µm^{-3}]	344 ± 15	341 ± 14	216 ± 4

Table 3.5: Comparison of length scale, dimensionality and scattering, before and after milk gelation as observed with SESANS and USANS, using different models. The amount of scattering is divided by squared wavelength to allow for direct comparison. Values in brackets are deemed unreliable and only shown for sake of completeness.

an exponential tail $\exp\left(-\frac{r}{2a}\right)$ to model the long-range interactions as those of a random inhomogeneous solid[I]. This new correlation function was dubbed a Fractal Network [32] and was in excellent agreement with USANS both in length scale and dimensionality, see table 3.5. Apparently, the self-affine model did not fit the SESANS data for milk and yoghurt as well, as it did the USANS data, indicating that both techniques, although very similar in many respects, are not interchangeable and have their own particular sensitivities. Due to the larger wavelength used in USANS, $(4.76/2.09)^2 \approx 5$ times more scattering was expected than with SESANS, but only about 3.5 times more was observed in milk and yoghurt; a factor of about 1.5 discrepancy, see table 3.5. In SESANS, the values for the scattered fraction $\Sigma\,\ell$ were established solely from the saturation level of the polarization and well-defined, whereas in USANS consistent values for $\Sigma\,\ell$ were obtained more indirectly, namely through calculating after fitting only for the length scale a.

Multiple scattering did not affect the results from the measurements. The SESANS technique is inherently not-sensitive to it, see eq. 3.1, and the USANS measurements on 10 mm samples were checked by comparing to signals from 18.0 mm samples, producing curves of similar shape. In spite of the high scattered fractions found in the USANS measurements, up to about half of the incident beam for yoghurt, multiple scattering did not seem to be an issue.

[I] as conjectured by Debye, Anderson and Bueche

3.5.2 Simulations

RLCA vs. DLCA

Cluster diffusion was modeled using parameter α and the increase of reactivity during simulated time with parameter ϖ. Higher values for α decreased mobility of large clusters (DLCA), and higher values for ϖ decreased reactivity (RLCA). Higher mobility favoured movement, especially of small clusters, causing the formation of locally denser structures, of globally equal density. Higher reactivity facilitated branching and caused the formation of more open structures. It played the more important role in the quick formation of a network from large aggregates. Reactivity depended on the stickiness, the sticking range and translational freedom for movement.

A higher overall probability for sticking with identical cluster mobility, would correspond to lower ϖ values at fixed α. For identical values of ϖ, increasing the sticking range effectively increased the reactivity, by allowing for more configurational freedom and decreasing correlations along grid lines, creating less-linear clusters. Higher values of the translational freedom also effectively increased reactivity, since more diverse configurations were explored, causing more collisions in the same number of steps and decreasing the number of steps before bonding occurred. The longest length scales z_{sat} and correlation lengths ξ were greatest in structures with high values for ϖ. By staying in the RLCA regime longer, denser aggregates were formed on the short length scale, leading to larger pores in the final network. Not surprisingly, the time needed for such a gelation was an order of magnitude larger than for DLCA. More results will be discussed at length in a future publication by this author.

Monte Carlo vs. Experiments

All measurements showed an increase of at least a factor of 3 in length scale after gelation, considering the typical and correlation lengths, with which RLCA findings agree well. However, the largest lengths observed in SESANS increased up to a factor 20, which could not be reproduced with this simulation model. Apparently, even more dense structures were created during actual gelation, than during simulation. It might be that the actual process stays even longer in RLCA. It is also possible that off-lattice simulations would produce longer aggregates, or that the log-normal distribution of casein micelles sizes contributes to more dense packings. Simulations in continuous space would require a much more elaborate approach. Polydispersity cannot be properly taken into account for particles on a grid, but would be easily incorporated in an off-lattice simulation. Likewise, the role of the medium was neglected in this simulation model. The spheres could only interact with each other, effectively simulating aggregation in a vacuum. Although any contribution of the medium was not expected

to influence the formation of individual aggregates much, it is quite possible that the formation of much larger pores in the gel would be favoured due to surface tension of water.

3.6 Conclusions

The casein micelle size distribution in fat-free milk was determined accurately with SESANS. Using a log-normal distribution of solid spheres, the most frequent milk particle size, the average particle size and the degree of polydispersity were easily determined. The average size concurred with USANS observations, described with a self-affine model. Overall an average milk casein micelle diameter of $D = 240$ nm was found, consistent with literature on other milk samples using different techniques, previous SESANS experiments and DLS measurements. The dimensionality of milk was expected to be $d_F = 3$, but proved hard to determine experimentally. Because the milk particles were small with respect to the sensitive ranges of SESANS and USANS, no information was acquired about their internal structure.

The structure of yoghurt contained length scales from half a micrometer up to 5 micrometers according to SESANS. A typical length scale of about 840 nm was established for yoghurt, corresponding to 3.5 milk micelles, on which SESANS and USANS were in excellent agreement with each other, whereas the longest length scale corresponded to 20 micelles, which could only be observed with SESANS. The dimensionality was determined to be $d_F = 2.3$ with SESANS and USANS, and agreed with literature values. However, both measurement methods only agreed well using different models. The fractal dimension indicated that the gelation mechanism is either somewhere between or a combination of the RLCA and DLCA regimes for cluster–cluster aggregation. This supported our hypothesis that the process was initially reaction limited, but became diffusion limited later on, due to a gradual increase of reactivity.

Reliable information about the kinetics of the milk to yoghurt coagulation were obtained with USANS. Since the aggregation of micelles was pD-driven in $D_2O$and pH-driven in H_2O, the onset of aggregation was determined by the dissociation of GDL. The cluster–aggregation kinetics relied both on acidity and cluster diffusion. It took about two hours before a change in lengths was observed, which became roughly stationary after eight hours, whereas the dimensionality of the system was determinable three hours into the process. However, the simulations showed that the formation of a network from large aggregates was a slow process, with little contribution to the measured signal. The actual gel time was therefore not extracted from the kinetic measurements. The overall structure of the casein micelles did not appear to be affected by the gelation. Therefore, all observed differences were due to a rearrangement

of their external structure, in support of the adhesive sphere model. Two mechanisms could be at work during formation of the final structure:

- the clustering of small aggregates out of mobile monomers, dimers and trimers, in a relatively low reactivity regime, where the acidity had started to increase slowly,
- and the formation of large, much less mobile structures from small aggregates, in an increasingly reactive regime, until gelation occurred.

The dimensionality of the system, would depend largely on the first mechanism. The typical length scale increase in the system would be largely due to the second mechanism. Therefore it was concluded, that the first mechanism continued during the first three hours and that the second mechanism started after two hours up to eight hours and beyond. The simulations showed a similar progression, where structures most comparable to the experimental findings were produced in an environment with initially very little and slowly increasing reactivity.

These mechanisms, which determine the structure and kinetics of acid-induced gel formation in milk, depend on temperature [61] and on the rate of acidification, which also depends on the temperature [62]. At constant temperature, we find that structure and kinetics of this gelation are best described by a transition from RLCA towards DLCA. The change from initial fast Brownian motion with low reactivity to a decreasing diffusion speed with increasing reactivity, determines the locally dense and globally more open structure. Low mobility, both from locally constrained motion of particles in the forming gel and the slow diffusion of large aggregates, causes the gel time to be significantly larger than the time required for the acidity to reach its final value. This combination of different mechanisms in colloidal gel formation are consistent with literature published during the last few years [63].

Acknowledgments

The author thanks Chris Duif, Jeroen Plomp, Robert Andersson and Ad van Well (all NPM^2/R^3/TU Delft, The Netherlands) for assisting with the SESANS measurements and their valuable discussions; Krishna Kowlgi (DCT/TU Delft, The Netherlands) for performing DLS measurements; Prof. D. Kearley (Ansto, Menai, Australia) for advising on simulation techniques and Peter Walter, Sven-Oliver Seidel and Robert Monka (all HCB, Berlin, Germany) for assisting with the USANS measurements.

This work is part of the research programme of the *Stichting voor Fundamenteel Onderzoek der Materie (FOM)*, which is financially supported by the *Nederlandse Organisatie voor Wetenschappelijk Onderzoek (NWO)*.

This research project has been supported by the European Commission under the 6$^{\text{th}}$ Framework Programme through the Key Action: Strengthening the European Research Infrastructures. Contract n°: RII3-CT-2003-505925 (NMI 3).

CHAPTER 4

From RLCA to DLCA in 3D Monte Carlo

Léon F. van Heijkamp, Jouke R. Heringa, Ignatz M. de Schepper and Wim G. Bouwman.
This chapter consists of an article to be submitted to the Journal of Colloid and Interface Science for publication under the title 'From Reaction to Diffusion Limited Cluster–cluster Aggregation in 3D Monte Carlo with increasing reactivity'.

Abstract

In a 3D Monte Carlo simulation study of cluster–cluster aggregation on a lattice with Periodic Boundary Conditions, we control the reaction rate of clusters diffusing and bonding on a grid, to study the transition from reaction limited cluster–cluster aggregation (RLCA) to diffusion limited cluster–cluster aggregation (DLCA). The aggregation of a destabilizing colloidal system is simulated using a time-dependent, global reactivity with a tunable relaxation time. For a volume fraction ϕ_{V} all neighboring monomers immediately form clusters with an average mass around $1/(1-3\phi_{\mathrm{V}})$ in DLCA with a broad size distribution in non-dilute systems.

A transition from RLCA to DLCA occurs when the reaction time is smaller than the monomer diffusion time, which occurs when the relaxation time is well below the maximum reactivity. The transition is analytical in non-concentrated systems and can only occur before the cluster mass distribution starts to collapse, which is independent of concentration. For reaction times far exceeding the monomer diffusion time, aggregation remains reaction limited and initial systems consist predominantly of monomers. RLCA occurs with long living, narrow distributions of primarily small clusters. Their diffusion leads to larger coordination numbers, more bond formation and lower dimensionality. The extended percolation and gelation time result in denser gels with larger cavities.

4.1 Introduction

Soft condensed matter systems can kinetically arrest, which is specifically significant for colloidal suspensions. Because of the much larger space and time scales, colloids are more readily studied than their atomic counterparts. At large packing fractions colloids can undergo a glass transition, which has been well described in recent years [64–66]. However at low densities the kinetic arrest is poorly understood. The sol–gel transition is a major field in physical chemistry, but with a disputed underlying mechanism. A lot of contradicting experimental results and conflicting models have been presented over the years [67], but no unifying theoretical framework exists. Predicting structural and dynamical properties of gels, requires an understanding of their formation.

A variety of gel materials are formed through the transition of the solid phase from discrete into continuous, which impedes the liquid phase from flowing and leads to a bi-continuous structure or even a phase inversion. Gelation creates materials with remarkable properties ranging from elastic like jelly to rigid like silica gel. Stable colloidal suspensions without long-range repulsive interactions behave like hard spheres. Many colloidal particles have a short-range attractive potential which is only exhibited when a short-range repulsive interaction is removed. This destabilization causes the particles to form aggregating clusters, frequently modeled as adhesive hard spheres forming a network [68, 69]. Insight into clustering of such randomly distributed components has many applications in science, industry and everyday life. A numerical model for lattice Monte Carlo simulations has been devised by Gimel *et al.* for diffusion limited cluster–cluster aggregation (DLCA) [45–48]. In DLCA the reactivity is constant and large with respect to diffusion, causing neighboring particles to bond immediately. Hence only moving clusters need be considered. Fig. 4.1 shows an example of two clusters in a late-intermediate stage of DLCA. In the initial stages of DLCA, systems with concentrations well below the critical volume fraction $\phi_V = 0.3116$ [70] will consist of many small clusters, which can move and grow quickly throughout the system. As the clusters become more massive during flocculation, their numbers drop and they lose mobility, causing the process to slow down. Eventually a

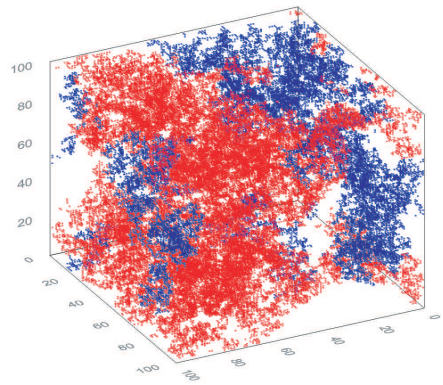

Figure 4.1: A snapshot of a DLCA simulation at 25% gel time. The two largest clusters of the total 269 clusters are shown, composed of 35,980 (red) and 16,604 (blue) monomers, with 100,000 monomers in total.

large percolating cluster forms, onto which the remaining material aggregates to form a fully gelated structure. Systems with concentrations above the critical volume fraction consist for a large part of neighboring particles, which bond immediately at high reactivity. Such concentrated DLCA systems are therefore very likely to contain a percolating structure from the start [71].

However, aggregation processes do not necessarily occur under high reactivity conditions. In reaction limited cluster–cluster aggregation (RLCA) the reactivity is very low compared to particle diffusion, requiring many particles to come into contact before a bond is formed. Comparing for equal mobility, RLCA requires much more time and results in denser structures than DLCA. These processes have been simulated using very low bonding probabilities [72], without explicitly securing the reactivity. It is also quite common for processes to show an increase in reactivity throughout aggregation. They may start as RLCA and finish as DLCA, having had similar timescales for bonding and diffusion somewhere in between. In the gelation of milk micelles to yogurt for example, the pH in milk starts roughly neutral and decreases as bacterial cultures convert lactose sugar into lactic acid, increasing the reactivity while the micelles aggregate until gelation [33, 55].

Previous work using lattice Monte Carlo and comparable techniques, such as off-lattice Monte Carlo and Brownian Dynamics simulations [47, 48, 73, 74] assumes percolation as the underlying mechanism for gelation, defining the gel point as the instant where a cluster connects to itself across the lattice. Percolation theory is a well-established branch of mathematics with many applications and for which a mean-field theory has been developed [75–77]. Lu *et al.* [78] argue that gelation of spherical particles with short-range attraction occurs through spinodal decomposition, where DLCA corresponds to formation of strong bonds and RLCA to weaker or reversible bonding. In this paper we investigate the similarities and differences between systems aggregating in DLCA and RLCA, using a 3D Monte Carlo model with increasing reactivity. We have modified the model by Gimel *et al.* to incorporate an explicitly defined global reactivity, decoupling bond formation from cluster movement. Bonds may form both intra- and inter-cluster at any time and bonding probabilities depend on the reactivity and the time step. To model the gelation of an initially stable colloidal suspension through acidification, we have chosen a convenient time-dependent reaction speed $k(t)$ to represent a generic acid-base titration curve. The rate of reactivity increase is controlled by a main parameter and can be varied from a step function (instantaneously selecting DLCA) to nearly zero increase (remaining in RLCA). This way the reactivity can model both quickly and slowly destabilizing colloidal suspensions. We show both analytically and numerically, that if the reactivity increases fast enough, initial RLCA processes can convert to DLCA.

4.2 Simulation

4.2.1 Chemistry

A sol is a suspension of discrete colloidal particles in a continuous liquid medium. A gel is a semi-solid, which has both solid and liquid characteristics. It consists of a continuous solid matrix encapsulating a liquid phase. If the liquid becomes fully segregated in the gel, the sol–gel phase transition is a phase inversion. The colloidal particles in suspension can be considered an ideal gas. At thermal equilibrium, all particles and clusters have the same average kinetic energy, equal to the thermal energy of the medium. Without rotational or vibrational degrees of freedom, the kinetic energy manifests as translations only. A cluster of mass m_c has a mean-squared velocity of $3k_\mathrm{B}T/m_\mathrm{c}$, with Boltzmann constant k_B and temperature T. The Einstein-Smoluchowski relation states that Brownian motion is characterized by a self-diffusion coefficient equal to half the mean-squared displacement per unit of time. To account for the inertia of the clusters, their random momentum has to be distributed according to a diffusion coefficient that depends on their mass. Clustering is the result of irreversible bonding reactions, which occur nearly exclusively between pairs of clusters at non-constant reaction speed $k(t)$:

$$\begin{aligned} \mathrm{A}_n + \mathrm{B}_m &\xrightarrow{k(t)} \mathrm{C}_{n+m} \\ \frac{[\mathrm{C}_{n+m}]}{\mathrm{d}t} &= k(t)\,[\mathrm{A}_n][\mathrm{B}_m], \end{aligned} \tag{4.1}$$

where any two clusters A and B of mass n and m form a new cluster C of mass $n+m$.

4.2.2 Model

The simulation model consists of an initial random configuration of N_0 monodisperse monomer particles, placed on separate lattice points. Each monomer is assigned mass m and diameter D. Simulation time is defined by monomer diffusion, as shown in section 4.2.3. Expressing length, mass and time in terms of monomer properties, gives dimensionless physical quantities for the whole simulation. The Brownian motion is modeled as random, mass-dependent movement. Particle interactions are those of adhesive, hard spheres. The dispersion medium has no properties and no interaction with the particles, i.e., it is described as a vacuum.

The layout of the simulation algorithm is shown schematically in fig. 4.2. The main problem is the simultaneous movements of many particles if it causes them to overlap in space. In Monte Carlo this is overcome by allowing at most

one cluster to move each cycle and adjusting the time-frame accordingly. The simulation box is a cubic grid of side L with lattice spacing D in all three directions and with Periodic Boundary Conditions (PBC). The system volume $V = L^3$ equals the number of lattice sites, so that the overall density is equal to the volume fraction $\phi_{\mathrm{V}} = \frac{N_0}{V}$ occupied by the monomers. A lattice poses severe restraints on cluster orientation and displacement, but has substantially less computational costs than off-lattice simulations, thus enabling runs of larger systems. The density distribution of the simulation box is

$$\rho(x,y,z) = \begin{cases} 1 & \text{if occupied (at } N_0 \text{ sites)} \\ 0 & \text{if empty (at } V - N_0 \text{ sites).} \end{cases} \tag{4.2}$$

The simulation starts at time $t = 0$ with $N_{\mathrm{c}}(0)$ initial clusters and $N_{\mathrm{b}}(0)$ initial bonds, which if zero gives N_0 clusters. A neighborhood list is constructed to store all bound and unbound particle pairs. Each cycle n_{step}, one out of the N_{c} clusters is randomly selected for movement. This cluster has a movement probability P_{move}, determined by its mass m_{c}. If this probability exceeds a random number, the cluster is translated by one monomer diameter in one randomly selected direction from a set of allowed directions, but only if no particle overlap will occur, i.e., if all the sites to be occupied are available. If a cluster movement is performed, the neighborhood list is updated accordingly.

Regardless of cluster movement, new bonds may then be irreversibly formed between all unbound adjacent particles. This happens according to the bonding probability $P_{\mathrm{bond}}(t)$, which is a global property of the system and depends on the reactivity $k(t)$ and variable time step Δt. A bond can be formed once between any pair of particles within bonding range and fixes their relative positions. Bond formation is evaluated for each particle pair individually, including pairs belonging to the same cluster. Aggregation occurs when particles of different clusters form a bond and one cluster assimilates the other. Thus aggrega-

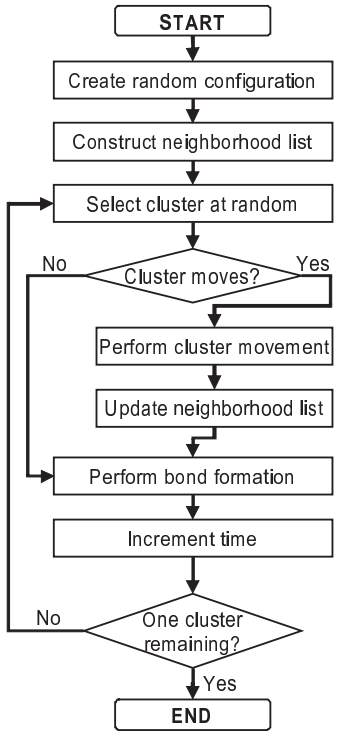

Figure 4.2: Flowsheet of the main simulation procedures.

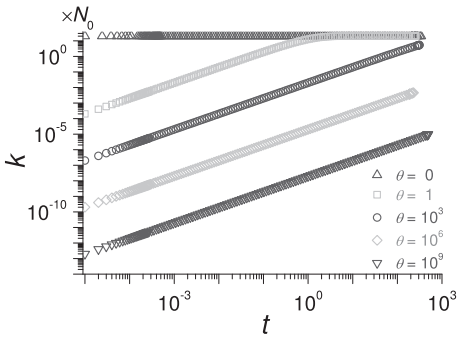

Figure 4.3: The reactivity k as a function of simulated time t for the θ-values shown in the legend. This main parameter controls the time required to reach maximum reactivity $k_{\max}$ at $20N_0$, using $N_0 = 10^5$ monomers and $\phi_{\mathrm{V}} = 0.1$.

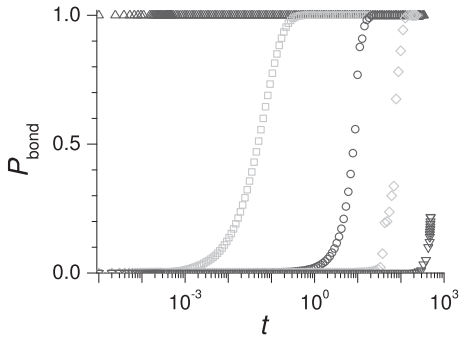

Figure 4.4: The bonding probability P_{bond} as a function of t (see eq. 4.8), for the runs shown in fig. 4.3. The dependency on increasing time-step and reactivity, causes the bonding probability to increase faster than $k(t)$ for equal θ.

tion causes the growth of clusters and reduces their number. Simulated time is then incremented by Δt and the cycle repeated until one aggregate remains.

For non-concentrated systems, clusters will initially grow as nucleation and diffuse. As clusters grow larger, they may connect or interpenetrate. When a cluster grows beyond the size of the box, it may connect to itself and percolate the system in one direction. The earliest instance is called the percolation time t_{perc}. All clusters ultimately connect to each other into a final aggregate, which in general will percolate isotropically. This continuous phase constitutes a 3D-network and its formation time is considered to correspond to the gelation time t_{gel}. The simulation is ended when $N_{\mathrm{c}} = 1$, since movement becomes meaningless, although some unbound particle pairs may remain.

4.2.3 Algorithm

As clusters are assimilated during simulation cycles, the ones remaining are selected more often. To ensure that the sampling frequencies remain equal, the simulation time is incremented each cycle by the probability for selection

$$\Delta t = \frac{1}{N_{\mathrm{c}}(t)} \in \left[\tfrac{1}{N_0}; \tfrac{1}{2}\right]. \tag{4.3}$$

The cluster dynamics are expressed as the probability P_{move} for a randomly selected cluster i of $m_{\mathrm{c,i}}$ monomers to move [45]. This probability models the diffusion coefficient of a cluster and is defined to scale as a negative powerlaw of the cluster mass with exponent α and given by

$$P_{\mathrm{move},i} = {m_{\mathrm{c,i}}}^{-\alpha}. \tag{4.4}$$

If its movement probability exceeds a random number between 0 and 1, a selected cluster will move. In total three random numbers are required for the movement procedure: selecting a cluster, deciding if it moves and selecting one of the allowed directions. Main parameter α is the inverse of the expected fractal dimension d_F of the final structures, which are expected to have a dimensionality somewhere around 2 [79]. Small variations of α in this range have nearly no influence on the kinetics [45, 46, 58]. A fixed value $\alpha = \frac{1}{2}$ is used.

The bonding probability P_bond depends on the global reaction speed k and the time interval Δt during which the particles are in contact. The time-dependent reaction speed $k(t)$ is chosen to be a smooth, monotonically growing function from 0 to k_max, resembling typical titration curves in acid-base reactions. Its rate of increase is controlled by the second main parameter θ, a relaxation time that scales the reaction time:

$$k(t) = k_\mathrm{max} \left(1 - \mathrm{e}^{-t/\theta}\right). \tag{4.5}$$

The relaxation time from zero to maximum reactivity is determined by θ. The maximum reaction speed is an arbitrarily large constant k_max above zero. The initial reaction acceleration $\frac{\mathrm{d}}{\mathrm{d}t}k(0)$ is given by the ratio k_max/θ. The reaction acceleration goes to zero for times much larger than θ.

For $\theta = 0$ the reactivity $k = k_\mathrm{max}$ at all times and clustering is diffusion limited, i.e., the regime is DLCA. Using any $\theta > 0$ causes the system to start with RLCA, as the reactivity starts at zero and continuously increases towards maximum. Fig. 4.3 shows the reaction speeds used in five runs with different rates of increase. The amount of bonds N_b formed over time is opposite to the change in unbound particle pairs N_u and is linear in k and N_u. For very large systems the time step becomes very small, which allows to write

$$\frac{\mathrm{d}N_\mathrm{b}(t)}{\mathrm{d}t} = -\frac{\mathrm{d}N_\mathrm{u}(t)}{\mathrm{d}t} = k(t)N_\mathrm{u}(t). \tag{4.6}$$

The reactivity is therefore equivalent to the relative change in unbound neighbors, which does not depend on concentration. The solution of eq. 4.6 is

$$N_\mathrm{u}(t) = N_\mathrm{u}(0)\ \mathrm{e}^{\theta\, k(t) - k_\mathrm{max}\, t}, \tag{4.7}$$

where $N_\mathrm{u}(0)$ is determined by the initial coordination number. Bond formation can be evaluated per particle or per pair, reducing the computational effort by half. Defining P_bond as the number of bonds N_b formed per unbound particle

pair N_u during interval Δt, makes P_bond equal to the relative decrease in N_u:

$$P_\mathrm{bond}(t) = \frac{N_\mathrm{u}(t-\Delta t) - N_\mathrm{u}(t)}{N_\mathrm{u}(t-\Delta t)} = 1 - \mathrm{e}^{\theta\,\Delta k(t) - k_\mathrm{max}\,\Delta t}, \tag{4.8}$$

where we have written $\Delta k(t) = k(t) - k(t-\Delta t)$. All *a priori* criteria for the bonding probability are satisfied, since it cannot be negative or exceed one, goes to zero when Δt, k_max or both go to zero and goes to one when θ approaches zero. Evaluating bonding per particle in stead of per pair would be equivalent to using double k_max, which follows from eq. 4.8 when evaluating $P_\mathrm{bond} + (1 - P_\mathrm{bond})\,P_\mathrm{bond}$. Since $P_\mathrm{bond}(t) = 1$ in DLCA, the minimum value for k_max follows from $\exp(-k_\mathrm{max}\Delta t) \downarrow 0$, which gives

$$k_\mathrm{max} \gg N_0, \tag{4.9}$$

where we have used $k_\mathrm{max} = 2 \cdot 10^6$ for all runs. Eq. 4.8 is global for all clusters and depends on the reactivity during the time interval Δt. Whether or not a pair of adjacent clusters will bond is determined by comparison of $P_\mathrm{bond}(t)$ at n_step with a random number between 0 and 1. Fig. 4.4 shows the resulting bonding probability for all unbound particle pairs obtained from runs with $N_0 = 10^5$ particles and $\phi_\mathrm{V} = 0.1$ volume fraction. The probability can increase substantially even at very low reactivity, when time steps become large enough near the end of the simulation.

4.2.4 Code speed-ups

Neighborhood list

A neighborhood list is used to keep track of the direct surroundings of each particle with respect to other particles and bonds formed. It is used to investigate site-occupancy and reduces computational time by one order of magnitude, by eliminating the need to loop over all particle pairs when moving and bonding. The neighborhood list is updated accordingly, requiring substantially less computational resources than rescanning the full configuration.

Scarce movement

Large clusters have a rather small probability to move. Thus, for a system with relatively large clusters, it may take many evaluated steps before any movement occurs, hence resulting in a large amount of dead time. To save another order of magnitude in computational time, we have devised an additional algorithm to calculate the probability $P_\mathrm{dead}(n)$ that in the next n steps no movements occur from the cluster-mass distribution. This procedure allows the system to skip many steps in which nothing happens. It is only applied when no clusters are in

contact with one another, since the number of clusters must remain unchanged. The probability that any cluster moves during a single step is $P_{\mathrm{move}}/N_{\mathrm{c}}$ and the probability that no cluster moves is therefore

$$P_{\mathrm{dead}}(1) = 1 - \sum_{i=1}^{N_{\mathrm{c}}} \frac{P_{\mathrm{move},i}}{N_{\mathrm{c}}} = 1 - \sum_{i=1}^{N_{\mathrm{c}}} \frac{{m_{\mathrm{c,i}}}^{-\alpha}}{N_{\mathrm{c}}}. \tag{4.10}$$

It follows that the probability that none have moved after n steps is

$$P_{\mathrm{dead}}(n) = \left(1 - \sum_{i=1}^{N_{\mathrm{c}}} \frac{{m_{\mathrm{c,i}}}^{-\alpha}}{N_{\mathrm{c}}}\right)^{n}. \tag{4.11}$$

Comparing $P_{\mathrm{dead}}(n)$ to a random number $0 \leqslant Q_1 \leqslant 1$ yields the number of steps n_{skip} to be skipped, after which the movement of a certain cluster is to be enforced:

$$\begin{aligned} P_{\mathrm{dead}}(n_{\mathrm{skip}}) &\geqslant Q_1 \Leftrightarrow \left(1 - \sum_{i=1}^{N_{\mathrm{c}}} \frac{{m_{\mathrm{c,i}}}^{-\alpha}}{N_{\mathrm{c}}}\right)^{n} \geqslant Q_1 \\ \Rightarrow n_{\mathrm{skip}} &= \left\lceil \log Q_1 / \log\left(1 - \sum_{i=1}^{N_{\mathrm{c}}} \frac{{m_{\mathrm{c,i}}}^{-\alpha}}{N_{\mathrm{c}}}\right) \right\rceil. \end{aligned} \tag{4.12}$$

We have imposed that, after skipping n_{skip} steps, the total probability is 100% that a cluster moves. The probability that cluster j moves at that moment, is equal to its probability of moving in a single step, normalized with the total probability of any cluster moving in a single step:

$$P_{\mathrm{move},j}(n_{\mathrm{skip}}) = \frac{{m_{\mathrm{c,j}}}^{-\alpha}}{\sum_{i=1}^{N_{\mathrm{c}}} {m_{\mathrm{c,i}}}^{-\alpha}} \tag{4.13}$$

The cluster j to be moved can now be determined by comparison of the cumulative probability over the set of clusters to a second random number $0 \leqslant Q_2 \leqslant 1$

$$\sum_{i=1}^{j} P_{\mathrm{move},i}(n_{\mathrm{skip}}) \geqslant Q_2 \Rightarrow j, \tag{4.14}$$

yielding cluster label j. Movement in a random direction requires a third random number, just as in the original cluster movement procedure. After skipping n_{skip} steps, clusters may have come into contact and P_{bond} between two different clusters has to be evaluated over $\Delta t = \frac{1}{N_{\mathrm{c}}}$ as before. However, the particle pairs inside a cluster were already in contact and therefore have a larger probability to form additional bonds amongst each other. For them P_{bond} is also evaluated after skipping, but using $\Delta t = \frac{n_{\mathrm{skip}}}{N_{\mathrm{c}}}$, where N_{c} has remained constant.

Sporadic bonding

The straight-forward approach to bond formation requires the comparison between a random number and the bonding probability for each unbound, neighboring particle-pair. In reaction limited aggregation the bonding probability is usually assumed lower than one per mill [73] and the formation of a bond requires many evaluations. At such extremely low probabilities, it becomes computationally advantageous to use an alternative algorithm in which bonds are distributed randomly between unbound pairs [80] with a frequency determined by the reactivity. This procedure is analogous to the procedure for scarce movement and avoids many evaluations for unlikely events. However, here the amount to skip may exceed the number of possibilities, in which case no bond is formed.

A random number determines at which particle i a bond may be formed, if there is an unbound neighboring particle j present. Each particle has three directions in which it may form a bond. When looping over all possible bonding positions b from 1 to $3N_0$, a random number Q determines how many to skip:

$$b_{\text{skip}} = b_{\text{start}} + \left\lfloor \frac{-\ln Q}{k(t)} \right\rfloor, \tag{4.15}$$

with $b_{\text{start}} = 1$ for the first cycle and $b_{\text{start}} = b_{\text{skip}} + 1$ every next cycle. A small value for $k(t)$ gives a large b_{skip}, resulting in few evaluations per cycle. The particle number is given by $i = \left\lceil \frac{1}{3} b_{\text{skip}} + \frac{1}{3} \right\rceil$ during the loop. Particle j follows from the neighborhood list, using $\left\lfloor b_{\text{skip}} - 3 \left\lfloor \frac{1}{3} b_{\text{skip}} \right\rfloor + 1 \right\rfloor$ to obtain one of the three bonding directions. Only if a neighbor j is present and has no bond with i, a bond is created between them. Next Q is assigned a new random number and the start is set to $b_{\text{start}} = b_{\text{skip}} + 1$. The loop is continued using eq. 4.15 until b_{skip} exceeds $3N_0$. Any remainder is then taken into account by multiplying Q with the inverse of $3N_0 - b_{\text{skip}}$:

$$Q_{\text{new}} = Q_{\text{old}} \cdot \mathrm{e}^{(3N_0 - b_{\text{start}})\, k(t)}, \tag{4.16}$$

to be used the next instance this procedure is called.

4.2.5 Predictions

The initial simulation behavior can be analytically predicted when allowing for two main assumptions. The first assumption is that *the initial coordination number is proportional to the monomer concentration*, which would be true were the grid independently filled. In reality, the available space for monomers diminishes during filling, since their total number is fixed and they are not allowed to overlap. All coordinates on a 3D grid with PBC have six nearest

positions and the probability for any arbitrary site to be occupied is ϕ_{V}. At $t=0$ there are approximately $6\,V\,{\phi_{\mathrm{V}}}^2$ adjacent occupied sites. The coordination number is the average number of neighbors each monomer has and therefore $\approx 6\phi_{\mathrm{V}}$. The expected initial number of neighbor-pairs N_{n} becomes

$$N_{\mathrm{n}}(0)^* = 3N_0\phi_{\mathrm{V}}, \tag{4.17}$$

where the asterix denotes the first assumption. Except in highly concentrated systems initial clustering consists nearly exclusively of dimer and trimer formation, which do not contain any internal bonds. The second assumption is that *every bond formed in the early stages of the simulation, lowers the number of clusters by one*, i.e., $N_{\mathrm{c}}(t)=N_0-N_{\mathrm{b}}(t)$.

Since the system is assumed to be composed of primarily monomers and a fraction of pairs, a limited number of particle movements will have almost no effect on the coordination number. Therefore, the third assumption is that *the coordination number remains constant during the initial stage*. The amount of bonds formed during this stage is equal to the change in the number of initial unbound particle pairs, or $N_{\mathrm{b}}(t)=N_{\mathrm{n}}(0)-N_{\mathrm{u}}(t)$. The values at which DLCA will start are therefore

$$N_{\mathrm{b}}^{\circ} \approx 3\phi_{\mathrm{V}}N_0 \tag{4.18}$$

$$N_{\mathrm{c}}^{\circ} \approx (1-3\phi_{\mathrm{V}})\,N_0 \tag{4.19}$$

for the amount of bonds and clusters, where the circle denotes $\theta=0$ under both assumptions. For $\theta>0$ the development of numbers of bonds from 0 to N_{b}° and clusters from N_0 to N_{c}° can be predicted using the same assumptions. All pairs will be unbound, or $N_{\mathrm{u}}(0)=N_{\mathrm{n}}(0)$, so eq. 4.7 gives

$$N_{\mathrm{b}}^{\bullet}(t) = N_{\mathrm{b}}^{\circ}\left(1-\mathrm{e}^{\theta\,k(t)-k_{\max}t}\right) \tag{4.20}$$

$$N_{\mathrm{c}}^{\bullet}(t) = N_0 - N_{\mathrm{b}}^{\circ}\left(1-\mathrm{e}^{\theta\,k(t)-k_{\max}t}\right). \tag{4.21}$$

The bullet denotes $\theta>0$ under both assumptions.

4.2.6 Approach

In total 96 simulation runs were performed on a Linux workstation. Cubic boxes of side L consisted of a simple cubic stacking of sites, occupied by a fraction ϕ_{V}. The boxes used PBC and all sites had six nearest neighbors. Initial configurations were randomly generated from $N_0=\phi_{\mathrm{V}}\,L^3$ sites on boxes of either $L=50\,D$ or $L=100\,D$ and varying ϕ_{V}. A maximum reactivity $k_{\max}=2\cdot10^6$ was used for all runs, which was 20 times larger than the largest N_0 used. No finite size effects were observed in trial runs when system sizes exceeded 10,000

monomers. Bonding and movement were performed along the three orthogonal grid directions and restricted to distances corresponding to particle diameter D.

Simulation runs were primarily characterized by cluster mass growth, bond formation and cluster movement. Other quantities under investigation were the percolation time t_{perc} and gelation time t_{gel}, as well as coordination number, radius of gyration and radial distribution function. To explore the effects of varying reactivity regimes, runs were performed with θ-values differing orders of magnitude, where $\theta = 0$ would corresponded to DLCA and very large θ to RLCA. The effect of lower reactivity on these quantities was studied for several large, semi-dilute systems and for many smaller boxes with a range of concentrations.

Boxes of $L = 100\,D$ were filled with 10^5 monomers in order to grow large clusters, and were run for $\theta \in \{0, 1, 10^3, 10^6, 10^9\}$. In these semi-dilute systems of $\phi_{\mathrm{V}} = 0.1$, the maximum reactivity was 20 times in excess of N_0, satisfying condition eq. 4.9. The large systems allowed analysis for a wide range of cluster masses and sizes and for large particle-particle distances. Typical computing times varied from weeks to months. Boxes of $L = 50\,D$ were filled with concentrations from very dilute to concentrated beyond the bulk critical percolation threshold [70], above which a random configuration is expected to percolate. Volume fractions $\phi_{\mathrm{V}} \in \{0.01, 0.02, 0.05, 0.1, 0.2, 0.3116, 0.5\}$ were each run for $\theta \in \{0,\ 1,\ 10,\ 10^2,\ 10^3,\ 10^4,\ 10^5,\ 10^6,\ 10^7,\ 10^8,\ 10^9,\ 10^{10},\ 10^{11}\}$. In these systems N_0 ranged from 1250 to 62500, so that $k_{\max}$ was factors 1600 to 32 larger.Run times were in the order of days.

4.3 Results

4.3.1 Aggregation

Percolation and gel time

Percolation and gelation time are known to depend only on ϕ_{V} in DLCA for sufficiently large L [46]. Table 4.1 gives percolation and gelation times of large runs for θ's of increasing orders of magnitude. Figure 4.3.1 shows how the decreasing reactivity influences these times. The percolation time is constant for θ's from 0 to 1000, but triples when $\theta = 10^9$. Gel times fluctuate around 250 when $\theta \leqslant 10^6$ and increase when $\theta = 10^9$. Table 4.2 gives DLCA gel times for volume fractions from 0.01 to 0.5, where the gel time seems to be approximately proportional to the inverse square of the concentration as shown in figure 4.6. Gelation becomes instantaneous when the volume fraction approaches one. When $\theta = 10^{11}$, the gel time of a system with $\phi_{\mathrm{V}} = 0.5$ is up to two orders of magnitude larger than for DLCA. For systems with $\phi_{\mathrm{V}} = 0.01$ the

gel time appears nearly constant. However, the large stochastic fluctuations in these results make a small increase in gel time difficult to ascertain.

Number of clusters

The decrease of the total amount of clusters during aggregation is given by the decay of $N_c(t)$. In fig. 4.7 plateaus are observed at N_c° in this decay for θ's from 0 to 1000 when $\phi_V = 0.1$. Increasing θ causes the drop from 1 to N_c° to shift to larger times. When $\theta = 10^6$ the decay does not coincide with the DLCA plateau, but is still in accordance with DLCA for the last 10% of clusters, ending at a similar gelation time. Gelation time is substantially larger for $\theta = 10^9$.

θ	t_{perc}	t_{gel}	t_{perc}/t_{gel}
0	49	340	14%
1	57	257	22%
10^3	47	313	15%
10^6	79	231	34%
10^9	155	489	32%

Table 4.1: Percolation time t_{perc}, gel time t_{gel} and their ratio with varying θ, in boxes of $L = 100\,D$ and semi-dilute concentration $\phi_V = 0.1$.

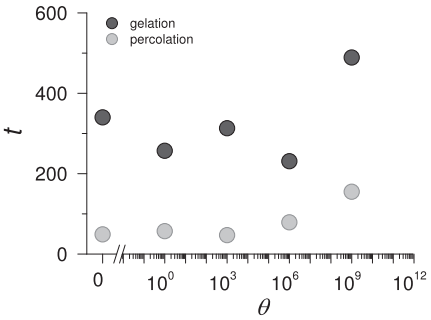

Figure 4.5: Percolation and gelation time as a function of θ, see table 4.1.

ϕ_V	t_{gel}
0.01	6435
0.02	3865
0.05	525
0.1	171
0.2	39
0.3116	24
0.5	14

Table 4.2: Gel times for DLCA at varying concentrations. Results are from boxes of $L = 50\,D$ for $\theta = 0$.

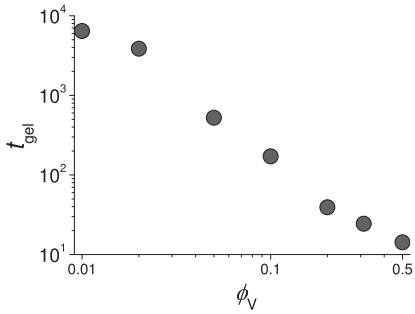

Figure 4.6: DLCA gel times at varying concentrations, see table 4.2.

Cluster mass

Fig. 4.8 shows the average cluster mass development for $\phi_{\mathrm{V}} = 0.1$. $\langle M_{\mathrm{c}} \rangle(t)$ is the average number of monomer constituents per cluster $N_0/N_{\mathrm{c}}(t)$. This gives the arithmetical mean over the population, as opposed to the also common mass-weighted number average. Systems which contain only monomers start at unit average mass and gel structures have mass N_0. For DLCA the cluster mass starts at $N_0/N_{\mathrm{c}}^{\circ}$, but when $\theta > 0$ there are no initial bonds. Runs with θ up to 10^4 coincide nearly perfectly with calculated $\langle M_{\mathrm{c}}^{\bullet} \rangle(t) = N_0/N_{\mathrm{c}}^{\bullet}(t)$ values. The average cluster grows at identical rates for any $\theta \leqslant 10^6$, once it is larger than about 10 monomers. Close to gelation, development is less smooth due to stochastics. These cluster mass results are generalized for a range of volume fractions in section 4.3.2.

Number of bonds and moves

Fig. 4.9 shows the amount of bonds formed per monomer $N_{\mathrm{b}}(t)/N_0$ at $\phi_{\mathrm{V}} = 0.1$. Initially each monomer has on average $N_{\mathrm{b}}^{\circ}/N_0 = 0.3$ monomers, corresponding to half the coordination number $6\phi_{\mathrm{V}}$. The number of bonds and clusters initially show equal opposite change, in agreement with the first assumption in section 4.2.5. However, non-linear clusters of more than three monomers can also form bonds internally without affecting the number of clusters. This ultimately allows N_{b} to increase faster than N_{c} decreases. The final number of bonds in the gel structure cannot be predicted *a priori* and is observed to be $N_{\mathrm{b}}(t_{\mathrm{gel}})/N_0 = 1.123 \pm 0.001$ at $\phi_{\mathrm{V}} = 0.1$ for $\theta \leqslant 10^6$. Using $\theta = 10^9$ increases the number of gel bonds by 13%, as shown in fig. 4.16 for $\phi_{\mathrm{V}} = 0.1$. The time-derivative of $N_{\mathrm{b}}(t)$ is plotted in fig. 4.10, showing at which times bonds are formed. The solid lines show the bond formation given by eq. 4.6, using eq. 4.7 for the number of unbound pairs and eq. 4.5 for the reactivity. Fig. 4.11 shows the cumulative number of performed moves $N_{\mathrm{m}}(t)$ for $\phi_{\mathrm{V}} = 0.1$. For $\theta \leqslant 10^6$ the number of moves is roughly equal to the simulation time up to $t \lesssim 1$, and for $\theta = 10^9$ this applies up to $t \gtrsim 50$. Beyond these times, the inertia of growing clusters begins to diminish movement. The systems comes to full arrest at t_{gel}.

Initial DLCA behavior

For DLCA, the reactivity is maximum from the beginning, causing all neighboring monomers to bond immediately. In fig. 4.7 and fig. 4.9 the initial numbers of clusters and bonds are at DLCA levels of approximately 0.7 and 0.3 per monomer, as predicted by N_{c}° (eq. 4.19) and N_{b}° (eq. 4.18). For any $\theta > 0$ the simulation starts at zero reactivity with only monomers and no bonds, which means that all pairs are unbound. For $0 < \theta \leqslant 10^6$ values, the number of clusters first decreases from N_0 to N_{c}° and the number of bonds first

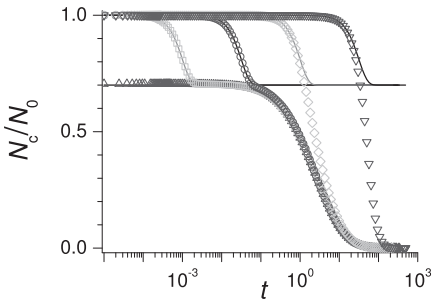

Figure 4.7: Decay of the number of clusters N_c per monomer for $N_0 = 10^5$ and $\phi_V = 0.1$, using $\theta = 0$ ($\triangle$), $\theta = 1$ ($\square$), $\theta = 10^3$ ($\bigcirc$), $\theta = 10^6$ ($\diamond$) and $\theta = 10^9$ ($\triangledown$). Solid lines show values for eq. 4.21.

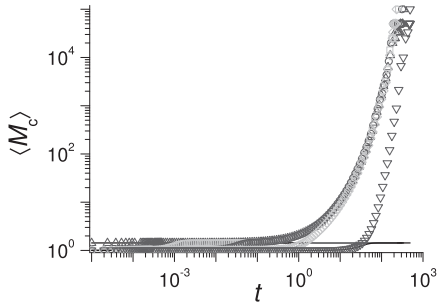

Figure 4.8: The average cluster mass $\langle M_c \rangle$ is inversely proportional to N_c. For small θ the initial $\langle M_c \rangle$ goes to $N_0/N_c^\circ = 1.43$, shown as solid lines.

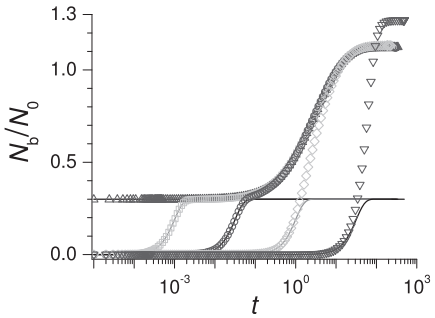

Figure 4.9: Average number of bonds N_b per monomer for the runs of fig. 4.7. Solid lines show values calculated with eq. 4.20.

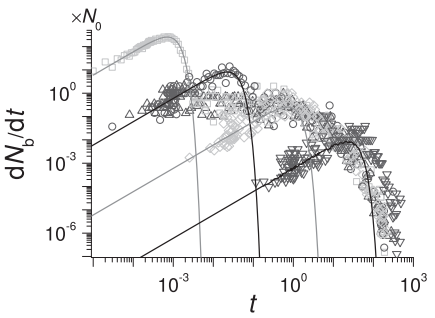

Figure 4.10: Momentary increase in the number of bonds dN_b/dt. Solid lines show bond formation calculated with eq. 4.6.

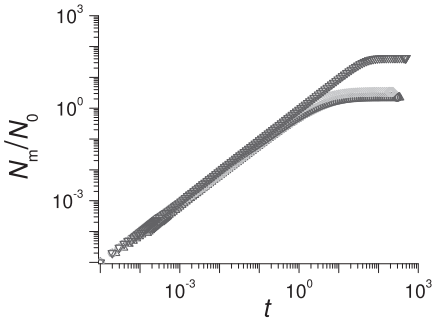

Figure 4.11: Average total number of moves N_m performed per monomer throughout the simulation, for the runs of fig. 4.7.

increases from 0 to N_{b}°, as shown in fig. 4.7 and fig. 4.9. The solid lines show that $N_{\mathrm{c}}^{\bullet}(t)$ (eq. 4.21) and $N_{\mathrm{b}}^{\bullet}(t)$ (eq. 4.20) accurately predict the transition from RLCA up to half the initial DLCA level for the investigated θ-range. Fig. 4.12 shows the reaction time $t_{1/2}$, which is defined as the time where half the initial amount of unbound neighbors has bonded. This means that $N_{\mathrm{b}}^{\bullet}(t_{1/2}) = \frac{1}{2}N_{\mathrm{b}}^{\circ}$, which can be rewritten to

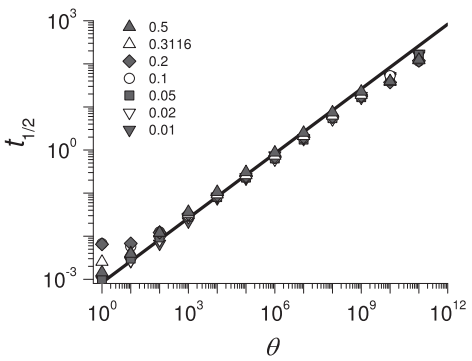

Figure 4.12: The transition time $t_{1/2}$ as a function of θ for a series of concentrations, giving nearly equal results. The legend shows ϕ_{v}-values and the solid line corresponds to eq. 4.23.

$$\theta\left(1-\mathrm{e}^{-t_{1/2}/\theta}\right)-t_{1/2} = \frac{\ln\frac{1}{2}}{k_{\max}}. \quad (4.22)$$

using equations 4.5 and 4.20. In a Taylor-expansion of the exponential term around $t_{1/2}=0$, the constant and linear terms cancel. Using $t_{1/2}>0$ gives for $\theta \gg t_{1/2}$ the square root relationship

$$t_{1/2} = \sqrt{2\ln 2\,\frac{\theta}{k_{\max}}}, \quad (4.23)$$

where $\theta/k_{\max} = \frac{\mathrm{d}}{\mathrm{d}t}k(0)$. Taking $t_{1/2}$ as a measure of typical reaction time and equating it to the diffusion time, a critical $\theta = 1.4\cdot 10^6$ follows. Below critical θ, the typical reaction time is less than the average movement time for monomers, which enables systems to develop from RLCA into DLCA. Above critical θ, aggregation is not diffusion limited and development is too slow to catch up with DLCA. For very large θ the coordination number does not remain constant and eq. 4.23 overestimates $t_{1/2}$ due to invalidity of our third assumption. The determined values for $t_{1/2}$ become less accurate at low θ, due to decreasing time resolution.

4.3.2 Cluster mass

Distribution

Average cluster mass does not disclose information on how the individual values are distributed. Figure 4.13 shows the mass fractions $\phi_{m_{\mathrm{u}}}(t)$ for several small and large masses m_{c}, each for a different $\theta \in \{0, 1, 10^3, 10^6, 10^9\}$. These were calculated from cluster mass histograms as $m_{\mathrm{c}} \cdot N_{\mathrm{c}}(t; m_{\mathrm{c}})/N_0$. The monomers (purple, dot), dimers (blue, dash) and trimers (cyan, dash-dot) are shown separately. Because of their smaller numbers, tetramers and pentamers (green,

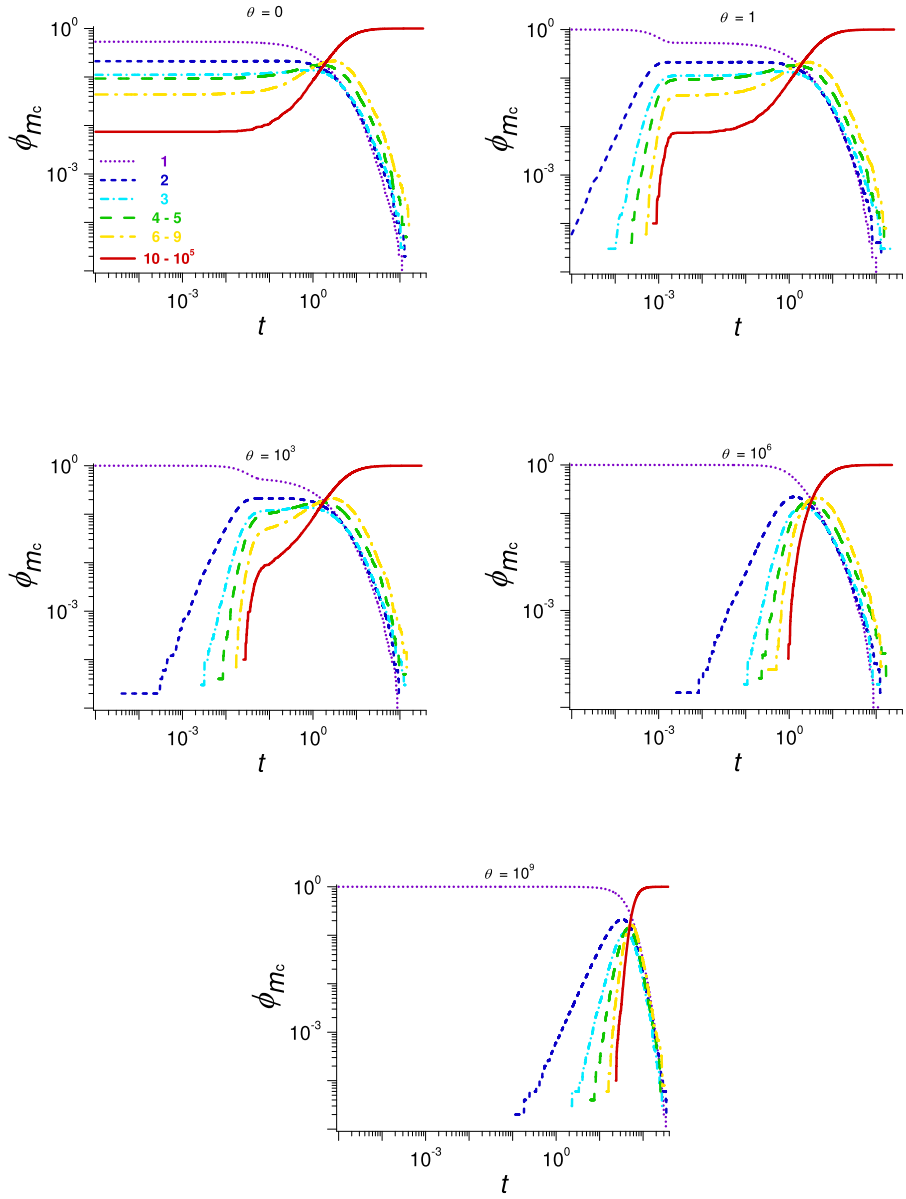

Figure 4.13: The evolution of cluster mass fraction ϕ_{m_u} from runs of $N_0 = 10^5$ monomers with $\phi_V = 0.1$ for a series of θ-values. The fractions were calculated from cluster mass histograms as the total mass present in clusters of m_c constituents divided by the total mass of the system N_0. Mass histograms were rebinned for clarity, using the cluster mass binsizes m_c shown in the legend in the top-left plot. The total cluster mass fraction sums to 100% over these bins at any time t.

wide dash) and $m_c = 6 - 9$ (yellow, wide dash-dot) were binned together. All higher cluster masses (red, solid) were stored in the final bin of $m_c = 10 - 10^5$.

For $\theta = 0$ fig. 4.13 shows that the DLCA plateau consists predominantly of monomers, dimers and trimers until $t \approx 0.02$. Around $t \approx 1$ the cluster mass distribution becomes increasingly wider, until it starts to collapse and after $t \approx 50$ only large clusters remain. When $\theta = 1$ initially only monomers and some dimers exist, but after $t \approx 0.002$ the system has caught up with DLCA and develops similarly. When $\theta = 10^3$ the system starts with monomers only and catches up to DLCA around $t \approx 0.07$. However, when increasing θ to 10^6, no dimers appear until $t \approx 0.002$ and no trimers until $t \approx 0.1$. The fractions of small clusters can no longer catch up to the DLCA levels, but the larger clusters still show the same rapid development. No aggregation is seen for $\theta = 10^9$ until $t \approx 0.1$ and rapid system development occurs much later. With only monomers much longer and the later creation of small clusters, the larger clusters appear too late to overlap with DLCA evolution.

Density series

In order to generalize gelation results with respect to bulk density, sets of runs have been performed with varying monomer concentrations ϕ_v from very dilute to concentrated for θ-values from DLCA to RLCA. Fig. 4.14 shows a selection of results with sets of number density $\phi_v \in \{0.01, 0.02, 0.05, 0.1, 0.2, 0.3116, 0.5\}$ for six selected values of $\theta \in \{10, 10^3, 10^5, 10^7, 10^9, 10^{11}\}$.

When $\theta = 0$ the initial average cluster mass is $\langle M_c^{\bullet} \rangle \approx 1/(1 - 3\phi_v)$. This DLCA plateau is visible for most densities when $\theta \leqslant 10^6$ and more pronounced for concentrated systems, since it is close to one for very dilute systems. Runs with the largest two densities show only slight humps for $\theta = 10^5$, whereas no trace of a plateau can be discerned when $\theta = 10^7$.

4.3.3 Reactivity

Cluster bonds

Different reactivity regimes cause different clustering behavior, expressed by differences in cluster mass development and bond formation. The initial amount of bonds in DLCA is approximately equal to half the coordination number and linear in ϕ_v, according to eq. 4.18. Fig. 4.15 shows $N_b(0)$ results for $\theta = 0$ from $L = 50\,D$ runs. The prediction is shown as a straight line with unitary slope in the log-log plot, and is very accurate, despite the finite size effects for dilute cases, which can cause strong fluctuations in initial coordination number. The

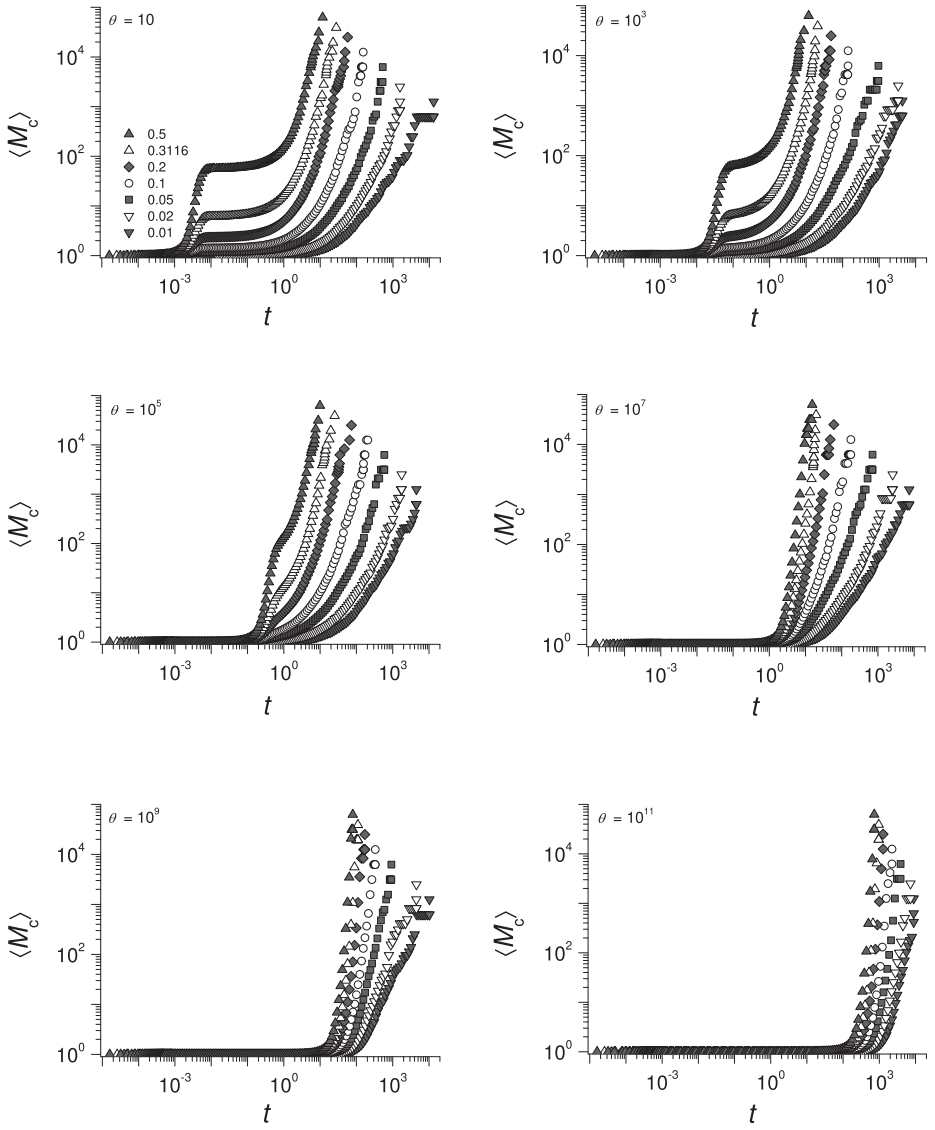

Figure 4.14: The average cluster mass $\langle M_c \rangle$ development for a series of densities from concentrated to dilute and the effect of increasing θ two orders of magnitude. Data for each θ is shown in a separate plot, containing seven volume fractions $\phi_V = 0.5$ (▲), $\phi_V = 0.3116$ (△), $\phi_V = 0.2$ (◆), $\phi_V = 0.1$ (○), $\phi_V = 0.05$ (■), $\phi_V = 0.02$ (▽) and $\phi_V = 0.01$ (▼), see top-left legend. Runs were performed in boxes with $L = 50\,D$ with $N_0 = L^3\phi_V$ monomers.

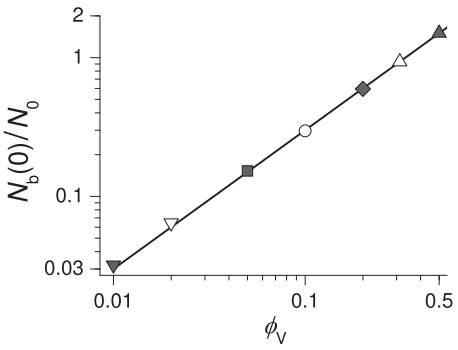

Figure 4.15: Average number of bonds N_b per monomer at $t=0$ for $\theta=0$ as a function of concentration ϕ_V. Results are in excellent agreement with $N_b^\circ(\phi_V)/N_0$ for DLCA (eq. 4.18), shown as a solid line.

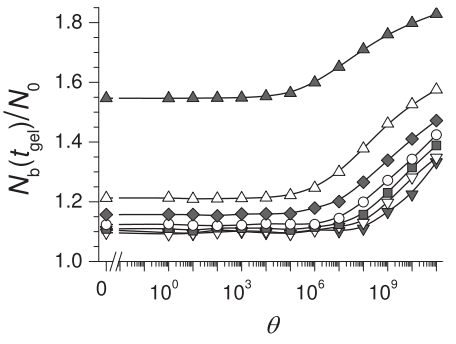

Figure 4.16: Average number of bonds N_b per monomer at $t=t_{gel}$ as a function of θ for concentrations ϕ_V of 0.01 (▼), 0.02 (▽), 0.05 (■), 0.1 (○), 0.2 (◆), 0.3116 (△) and 0.5 (▲). Lines are provided as a guide-to-eye.

number of bonds per monomer can vary between zero and three. The final number of bonds characterizes the gel structure. Fig. 4.16 shows the gel bonds as a function of θ for different concentrations. Higher densities give gels with more bonds. When decreasing reactivity, the gel structure seems unaffected up to $\theta = 10^6$. For larger values, the number of bonds increases in all cases. This increase seems to flatten for concentrated systems beyond $\theta \gg 10^{11}$.

Diffusion vs. reactivity

A common criterion to distinguish diffusion limited from reaction limited aggregation, is the number of moves required for a bond to form. Fig. 4.17 shows the average number of cluster bonds N_b/N_c at time t plotted against the number of cluster moves N_m/N_c at time t. For any $0 < \theta \leqslant 10^6$ bonding can still catch up to DLCA and continue as such, because the reactivity increases fast enough with respect to diffusion. For the investigated system sizes, a diagonal line separates the diffusion limited from the reaction limited regions, which develop in parallel beyond approximately 100 bonds per cluster. This represents the ratio of bonds versus moves that distinguishes DLCA from RLCA. For $\theta = 10^9$, N_m/N_b shows no overlap with ratios from lower θ's during any point of the simulation. It is reasonable to expect that N_m will become huge with respect to N_b for even higher values of θ.

In fig. 4.18 cluster bond formation is plotted as a function of cluster mass. Fits with straight lines through the origin give a linear relationship for $M_c \gtrsim 10$. When clusters are larger than about 10 monomers, their amount of bonds appears to scale linearly with their mass. The dashed line for θ's up to 10^6 has a slope of 1.13, whereas the dotted line for $\theta = 10^9$ has a slope of 1.27, both

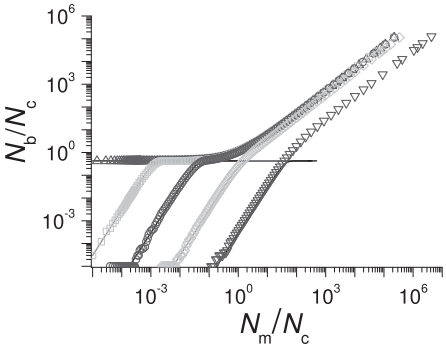

Figure 4.17: Average number of bonds per cluster $N_\mathrm{b}/N_\mathrm{c}$ plotted against the average number of moves per cluster $N_\mathrm{m}/N_\mathrm{c}$, for θ-values of 0 ($\triangle$), 1 ($\square$), 10^3 ($\bigcirc$), 10^6 ($\diamond$) and 10^9 ($\triangledown$). Results are at equal t for $N_0 = 10^5$ monomers with $\phi_\mathrm{V} = 0.1$. Values calculated with eq. 4.20 are shown as solid lines.

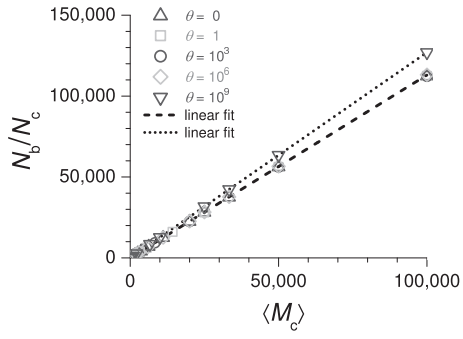

Figure 4.18: Average number of bonds per cluster $N_\mathrm{b}/N_\mathrm{c}$ plotted as a function of average cluster mass $\langle M_\mathrm{c} \rangle$ for the runs in fig. 4.17. Cluster bonds grow linearly for large masses, indicating stable coordination numbers in large clusters. More bonds are observed when $\theta = 10^9$ than for the lower θ's.

with an accuracy of ± 0.005. The slope has increased by 12%, which is in good agreement with the 13% increase in $N_\mathrm{b}(t_\mathrm{gel})$ seen in fig. 4.9.

4.3.4 Structure

Coordination number

The third assumption in section 4.2.5 states that the coordination number initially remains constant. The histograms in section 4.3.2 show that for any $\theta > 0$, semi-dilute systems consist almost entirely of monomers until clustering reaches DLCA-levels. Since Brownian diffusion on a grid cannot significantly affect the number of neighbors N_n in a large random configuration of monomers, the coordination number remains constant with some minor fluctuations. Fig. 4.19 shows that the number of neighbors indeed remains constant at first and then increases due to clustering. This development is similar to that of of the number of bonds in fig. 4.9, but without the transition to the DLCA-level. This shows that clustering beyond the DLCA-level occurs due to cluster diffusion causing increases in coordination number, which are subsequently fixed through bonding. For $0 \leqslant \theta \leqslant 10^3$, the evolution in coordination number cannot be distinguished from DLCA. For 10^6 the increase is delayed, but sharp enough to correspond to DLCA eventually. For 10^9 the coordination number increases much later and to larger values, creating more contact sites and thereby causing more bond formation.

The difference between half the coordination number and the number of bonds per monomer, is shown in fig. 4.20. For DLCA there is no difference, as

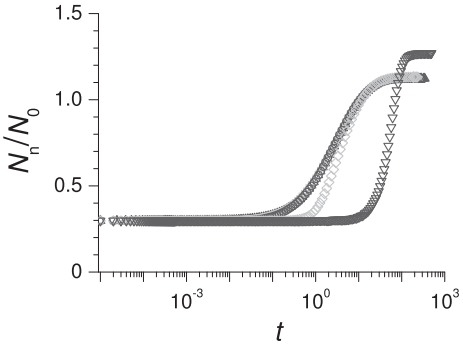

Figure 4.19: The average number of nearest neighbors N_n per monomer for $N_0 = 10^5$ monomers with $\phi_V = 0.1$. Results are for $\theta = 0$ ($\triangle$), $\theta = 1$ ($\square$), $\theta = 10^3$ ($\bigcirc$), $\theta = 10^6$ ($\diamond$) and $\theta = 10^9$ ($\triangledown$) and show the development of half the coordination number. These are similar to N_b (fig. 4.9) without the initial transition.

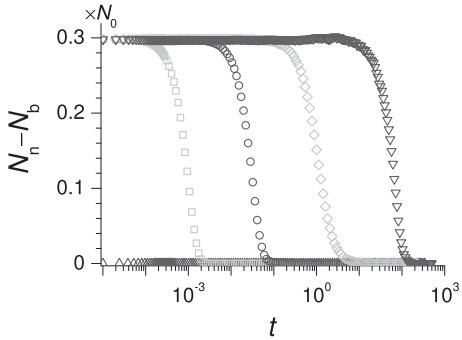

Figure 4.20: Difference between numbers of nearest neighbors N_n and bonds N_b, for results shown in fig. 4.19. For $\theta > 0$ initial values are $3\phi_V N_0$ as given by $N_n(0)^*$ (eq. 4.17).

any unbound neighbor will immediately bond. Increasing θ causes the system to start at the initial coordination number and reduce this difference later, as bonds are formed increasingly slower. For 10^9 there is actually a very slight increase in coordination number, before the major bond formation starts, showing how small, non-reactive clusters become surrounded by the more mobile monomers.

Radius of gyration

The density of clusters of mass m_c is determined by their size. The spatial dimensions of a cluster of random shape can be determined from the distribution of mass in space. The radius of gyration R_g in units of monomer diameter D is a measure for typical length and defined as the root-mean-squared-deviation of the m_c coordinates from the center of mass

$$R_g{}^2 = \frac{1}{m_c}\sum_{i=1}^{m_c}\left(x_i{}^2 + y_i{}^2 + z_i{}^2\right) - \frac{1}{m_c{}^2}\left[\left(\sum x_i\right)^2 + \left(\sum y_i\right)^2 + \left(\sum z_i\right)^2\right]. \quad (4.24)$$

In PBC clusters can extend outside the box, which requires them to be folded out. However, a percolating cluster has a gyration tensor with at least one infinite component [81], which makes it effectively infinitely large. Since the center-of-mass is then undetermined, the radius of gyration is undefined. Fig. 4.21 shows $\langle R_g \rangle$ as a function of $\langle M_c \rangle$ for varying θ, where $\langle R_g \rangle$ is the mean over the whole ensemble of non-percolating clusters. Percolation cause the growth of the mean to become erratic, since only the smaller, non-percolating clusters can be taken into account. Therefore, $\langle R_g \rangle$ loses meaning at t_{perc}. However, clusters formed for $\theta = 10^9$ are significantly smaller, down to about half the

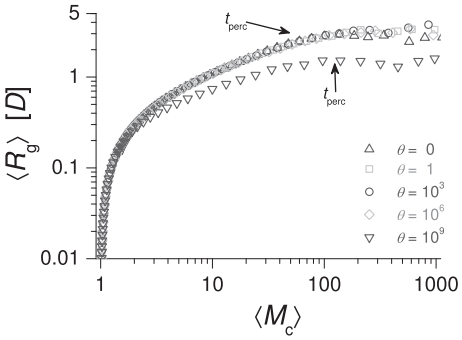

Figure 4.21: Average radius of gyration $\langle R_g \rangle$ as a function of average cluster mass $\langle M_c \rangle$ for $N_0 = 10^5$ monomers with $\phi_V = 0.1$. At $\theta = 10^9$ typical sizes are smaller thus clusters are more dense. The average is over non-percolating clusters.

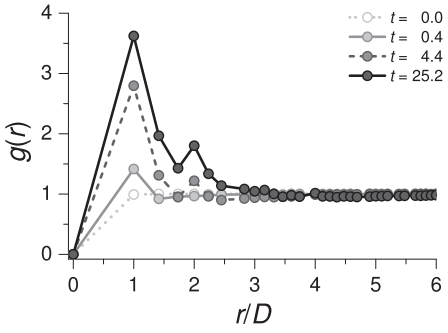

Figure 4.22: Radial distribution function $g(r)$ development for DLCA. Times are selected to show the intermediate change in short-range structure. Results are for $\theta = 0$ with $N_0 = 10^5$ monomers and volume fraction $\phi_V = 0.1$.

typical size at equal mass. Cluster size growth may follow a powerlaw after $\langle M_c \rangle \gtrsim 10$, as curves seem linear on a log-log scale before percolation.

Radial distribution function

The structure of isotropic systems has a radial density distribution $\rho(r)$ [73]. The pair-correlation function $g(r)$ gives the probability to find another particle in a spherical shell of radius r and width $\mathrm{d}r$ around any arbitrary center particle in the system, where $N_{\mathrm{shell}}(r)$ is the expected value. This radial distribution function (RDF) shows how the local number density of a system converts over distance into the mean number or bulk density ϕ_V, calculated from a normalized histogram of particle pair distances

$$g(r) = \frac{2}{N_0\, N_{\mathrm{shell}}(r)} \sum_{i=1}^{N_0-1} \sum_{j=i+1}^{N_0} \delta_{r,|\vec{r}_i - \vec{r}_j|}$$
$$N_{\mathrm{shell}}(r) = \phi_V \tfrac{4}{3}\pi \left[(r + \tfrac{1}{2}\mathrm{d}r)^3 - (r - \tfrac{1}{2}\mathrm{d}r)^3 \right] \tag{4.25}$$

where δ is the Kronecker delta, which is one when the distance between i and j equals r and is zero everywhere else. There is zero probability to find two particles overlapping, therefore $g(0) = 0$.

The aim is to see structure emerge from the initial configuration, which requires a normalization of the RDF for the number of integer squared lattice distances. The RDF of any initial box now shows the uniform distribution of monomers as a practically horizontal series of points around $g(r) = 1$ with minor fluctuations due to finite box size. This is shown as a series of dots in fig. 4.23 and its inset. However, $g(r)$ results in later stages of the simulation

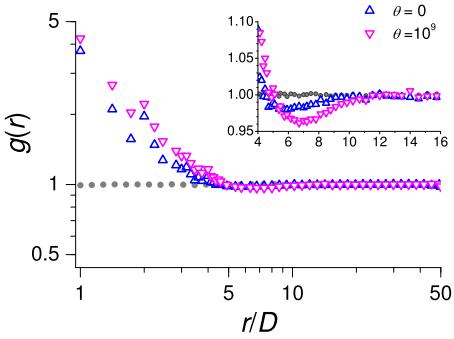

Figure 4.23: Radial distribution function $g(r)$ at t_{gel} for runs with $N_0 = 10^5$ monomers with $\phi_{\mathrm{V}} = 0.1$. Values at $t = 0$ are shown as gray dots. Results are given for lowest and highest θ-values since results at intermediate θ do not differ from DLCA. The inset shows a linear plot around the minimum.

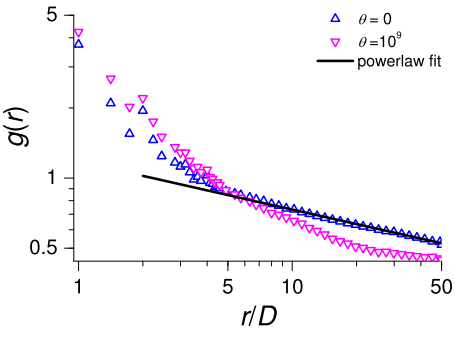

Figure 4.24: The RDF at t_{perc} of single, isolated percolating clusters for $\theta = 0$ and 10^9 for runs with $N_0 = 10^5$ and $\phi_{\mathrm{V}} = 0.1$. Short-range results are nearly identical to those at t_{gel} (see fig. 4.23). A powerlaw fit produced $g(r \geq 5) = 1.18 r^{-0.207}$ for the percolating DLCA cluster, shown as a solid line.

exhibit spikiness in the short range $r \lesssim 3D$, which can only be attributed to a grid effect, as the large number of these distances in the system diminishes the stochastics. This is supported by the smoothness of $g(r)$ at large r, which occur much less frequently.

Snapshots of the RDF at four different times are shown for $\theta = 0$ in fig. 4.22. The evolution of the RDF for different θ's shows initial clustering around $0 < t \lesssim 1$ for θ's 0, 1 and 10^3, whereas no clustering is observed for 10^6 and 10^9. At $r = D$ dimer formation produces a peak and a small dip between $\sqrt{2}D$ and $\sqrt{6}D$, due to a short-range depletion effect. Their magnitudes increase over time, slightly delayed for larger θ. The formation of larger clusters is observed around $1 \lesssim t \lesssim 10$ as both width and amplitude of the peak and dip roughly double. For low θ results become nearly identical. A similar RDF with less magnitude arises for 10^6, whereas it remains unchanged for 10^9. Short-range oscillations appear and disappear due to cluster movements, but are eventually dampened by aggregation, which fixes minimum values of $g(r)$. At times larger than $t \gtrsim 10$ differences become negligible between results for $\theta \in \{0, 1, 10^3, 10^6\}$ as the peak and dip grow towards their final widths and values, whereas for 10^9 only initial dimer formation becomes observable.

For any θ, the RDF evolution comes to a standstill during $t_{\mathrm{perc}} \leq t \leq t_{\mathrm{gel}}$, with a different result for 10^9 from the lower θ's. The gel structures for $\theta = 0$ and 10^9 are shown in fig. 4.23, where the inset shows that peak and dip are of larger magnitude and width. This indicates that this network is formed from denser clusters and has larger cavities. The values of $g(D)$ show a factor 13.0% increase and correspond to $N_{\mathrm{n}}(t_{\mathrm{gel}})/(3\phi_{\mathrm{V}})$ in concordance with fig. 4.19. In

both cases, the short-range gel structure $g(r \leq 5D)$ is determined mainly by the percolating cluster when compared to fig. 4.24, whereas the long-range gel structure is indistinguishable from the initial configuration. The long-range structure of the percolating DLCA cluster shows powerlaw behavior with an exponent of -0.2. For $\theta = 10^9$ the long-range structure $g(r > 5D)$ cannot be characterized by a single power, but seems to consist of multiple exponents ranging from -0.4 to -0.1. For DLCA the long-range structure would correspond to $d_{\mathrm{F}} = 1.81$ in two dimensional envelope space [58, 82], which is a frequently reported value in literature [47, 48, 73, 74]. However, no clear argument is supplied in literature why a two dimensional case should apply to a 3D system.

4.4 Discussion

Our model is based on a global, time-dependent reactivity $k(t; \theta, k_{\max})$, where particle bonding is decoupled from cluster movement and the rate of increase is controlled by θ for a given maximum reactivity $k_{\max}$. For $\theta = 0$ the reactivity is $k(t) = k_{\max}$ throughout the simulation and aggregation is diffusion limited. Using a $k_{\max} \ll N_0$ prohibits all pairs present at $t = 0$ to bond and does not give rise to an initial DLCA plateau, as seen in DLCA models which allow only moving clusters to bond [45]. If $k_{\max} \gg N_0$ the reaction time goes towards zero, causing immediate bonding of all initial pairs, which leads to an initial plateau in the number of clusters and bonds. The initial coordination number is approximately $3\phi_{\mathrm{V}}$ and all of these neighbors cause clustering, since the amount of internal cluster bonds is negligible in non-concentrated systems. Continued aggregation requires further increase of the coordination number, which occurs on the scale of typical monomer diffusion time.

For $\theta > 0$ there is negligible initial reactivity and the system starts reaction limited. If $k(t)$ increases fast enough with respect to diffusion, a transition from RLCA to DLCA is made and the system continues developing as DLCA. The typical reaction time determines the rate of this transition and is proportional to $\sqrt{\theta / k_{\max}}$. Gel times are independent of θ when $\theta < k_{\max}/(2 \ln 2)$, but increase radically for larger θ. When $\theta > k_{\max}/(2 \ln 2)$ a system of N_0 monomers cannot make the transition to DLCA, since the typical reaction time is larger than the typical diffusion time. The transition from RLCA to DLCA is analytical in dilute and semi-dilute systems, but large structures with internal bonds complicate the analytical description in highly concentrated systems.

Because of the very low reactivity, small clusters survive longer in RLCA. The coordination number in RLCA develops along a distinctively different trajectory from DLCA. Local fluctuations in coordination number are not locked immediately, but re-equilibrate. In RLCA the overall mobility remains longer be-

cause the rise in inertia occurs later. Exposed sites become surrounded by small clusters and the low reactivity also allows large clusters to inter-penetrate more deeply. The coordination number becomes substantially larger than in DLCA, resulting in more bond formation and more compact clusters. For $\theta = 10^9$ the average cluster size develops slower and stays smaller than at lower θ, as seen from the radius of gyration. Average R_g values as a function of cluster mass are also substantially smaller, evidence of the increased average denseness of the clusters.

Rottereau, Gimel and many others define the gel point as the first instance of a percolating cluster to occur [45, 46]. The underlying assumption seems to be that percolation in one direction represents a continuous phase, without clarifying how percolation in one direction would block the flow of the medium in a 3D system. In this model the percolating structure constitutes a part of the total mass and, depending on the initial concentration and reactivity, many clusters remain in its pores. We also see that the radial distribution function $g(r)$ does not significantly change after the formation of a percolating cluster, which determines the short-range gel structure, with a homogeneous long-range structure. Lu *et al.* [78] argue that gelation of spherical particles with short-range attraction occurs through spinodal decomposition. Their work shows that thermodynamic instability gives density fluctuations which ultimately lead to spanning clusters that dynamically arrest. They claim that it is phase separation and not percolation that corresponds to gelation in models for attractive spheres. We also interpret the sol–gel phase transition as the formation of a kinetically arrested structure from clustering monomers. A gel has a sponge-like, continuous matrix and the gel structure percolates isotropically, or at least in three orthogonal directions, so that its gyration tensor consists of three infinite components [81]. We therefore treat the percolating structure at t_perc as the skeleton of the gel and let all let moving clusters arrest onto it, and argue that this formation time t_gel corresponds better to the actual physical gelation time.

Our choice of model requires gelation for RLCA to occur before the reactivity increases too much. Despite the very low reactivity $k(t) < 5{\cdot}10^{-7}\, k_\mathrm{max}$ throughout for $\theta = 10^9$, the bonding probability does not stay below the commonly used $P_\mathrm{bond} \leq 0.001$ for RLCA [73] in the late stages. This is primarily due to the large time steps in the end. The increase in P_bond shortens gel time, causes bond-saturated structures and hinders deeper inter-penetration of the few large remaining clusters. This impedes further increase of the coordination number, preventing an even denser gel structure to arise. An improvement would be to run RLCA systems of $N_0 = 10^5$ monomers at $\theta \gg 10^9$. Possible other improvements on our model would involve rotational freedom, running off-lattice, incorporating monomer polydispersity and modeling particle-medium interac-

tions. The latter may realign clusters to create larger gel-pores and reduce the surface tension of the encapsulated medium.

4.5 Conclusions

In Monte Carlo models with constant diffusion speed, the regime in which clusters aggregate can be controlled from reaction limited to diffusion limited by varying the reaction speed. In systems without initial reactivity, an increasing reaction rate causes a transition from RLCA into DLCA when typical reaction time exceeds typical diffusion time. The clustering during this transition is analytical if the coordination number is moderate and unaffected by diffusion, which is true in non-concentrated systems during typical diffusion time. The transition has no effect on gel structure, shown by cluster mass distributions and coordination numbers.

Tuning the reaction time to be comparable to the diffusion time creates an aggregation regime of comparable reactivity and mobility. Despite initial aggregation being reaction limited, final gel structures still compare to those of DLCA. At much larger reaction times, systems stay in RLCA and produce gels with higher coordination numbers. The distribution of cluster masses is broad in DLCA, goes from narrow to broad when a transition occurs and is narrow in RLCA. Very low reactivity also decreases differences in aggregation behavior between different densities. The aggregation regime can be seen most clearly when comparing the number of moves required for bond formation.

In general we can conclude that for different reactivities clusters aggregate in similar fashion but on different time scales, as long as the coordination number remains unchanged. Compared to DLCA, gelation in RLCA occurs much slower, creates denser clusters and gels with larger cavities and of different fractal dimension. Regardless of reactivity, clusters of equal compactness are created up to the average cluster mass of a high-reactivity DLCA system, but not with the same distribution.

Acknowledgments

The author thanks Fred Naastenpad for his help with visualisation software.
This work is part of the research programme of the *Stichting voor Fundamenteel Onderzoek der Materie (FOM)*, which is financially supported by the *Nederlandse Organisatie voor Wetenschappelijk Onderzoek (NWO)*.

CHAPTER 5

Sample thickness optimization for SESANS

Léon F. van Heijkamp, Wim G. Bouwman and Ignatz M. de Schepper.

5.1 Introduction

SESANS measurement data is primarily characterized by the shape and the magnitude of the decaying polarization signal. The shape of the signal is determined by the projected density correlation function $G(z)$, expressing structure as spatial correlations between density fluctuations in a sample. The magnitude of the signal is the overall loss in polarization, which is determined by the thickness and scattering power of the sample. The quality of the signal is determined by the count rate in the detector; a product of the incident neutron flux and the transmission of the sample. Figure 5.1 shows a photo of a SESANS setup with two magnetic field regions, one before and one after the sample position. The spin-echo length z is set by the field strength. The length scales in a sample are probed by measuring the polarization for a range of spin-echo lengths. Length scales are measured from the width of a SESANS signal, of which the magnitude depends on the coherently scattered fraction of the neutron beam. The polarization can be observed to saturate at spin-echo lengths beyond the largest length scale present in the sample, if the scattering power is between 0.05 and 1.5. Measurements can therefore be performed with samples causing mostly single scattering up to a lot of multiple scattering.

Scattering is caused by inhomogeneities in the scattering length density (SLD) of a material. The likelihood for a neutron to scatter or be adsorbed when traversing a material increases for longer path lengths. Increasing the thickness of a sample causes more coherent scattering events, observed as less conservation of the polarization of the beam. Multiple scattering increases the polarization error, causing the relative error to blow up for strong signals and diminishing the sensitivity for $G(z)$. A thicker sample therefore results in a stronger, but less accurate signal.

The attenuation of the beam also increases when increasing sample thickness and the count rate at the detector drops. The optimal thickness is therefore

Figure 5.1: Photo of the SESANS setup at the Reactor Institute Delft, with the neutron guide exiting the reactor hall at the left. A crystal monochromator uses the Bragg condition to select a wavelength at a specific angle, after which a polarizer selects neutrons that have the same combination of their spin-eigenstates. Two magnets comprise the first magnetic region encoding the neutron spin, which can be described classically as Larmor precession or quantum-mechanically as the vertical separation of two neutron eigenstates. The selected magnetic field strength is proportional to the desired spin-echo length. A sample is placed on a translation table and moved in and out of the beam, in order to measure both empty beam and sample under equal conditions. Two magnets to the right form the second magnetic region decoding the neutron spin. This region has a geometry identical to the first, but with opposite field values. The echo condition is achieved by fine-tuning the four magnets with respect to each other. The polarization is measured by a combination of analyzer and detector.

a trade-off between signal strength and attenuation, giving an optimum in the signal-to-noise ratio. The signal strength and attenuation are characterized by the macroscopic coherent scattering cross section Σ and the linear attenuation coefficient μ, which both depend on the neutron wavelength and the neutron interaction with the materials in the sample. For a monochromatic beam of known wavelength, the amount of coherent scattering is determined by the average SLD-fluctuation and the typical separation between those fluctuations, and the attenuation is determined primarily by the incoherent scattering and absorption cross section.

Many samples contain H_2O D_2O and/or aluminum in SESANS. Table 5.2 shows the scattering length densities and attenuation factors for light water, heavy water and aluminum, which are calculated from the scattering lengths and nuclear bound cross sections of hydrogen, deuterium, oxygen and aluminum, shown in table 5.1. Light water, heavy water and aluminum all have different orders of magnitude of attenuation. The factor μ is the inverse of the $1/\mathrm{e}$-length, at which about 37% of the neutrons are transmitted. The neutron

Element	b_{coh} (fm)	b_{inc} (fm)	σ_{coh} (b)	σ_{inc} (b)	σ_{abs} (b)
$^{1}_{1}$H	–3.74	25.28	1.758	8.027	0.333
$^{2}_{1}$H (D)	6.67	4.04	5.592	2.050	0.001
$^{16}_{8}$O	5.81	0.00	4.232	0.000	0.000
$^{27}_{13}$Al	3.45	0.00	1.495	0.008	0.231

Table 5.1: Tabulated scattering lengths and cross sections of hydrogen, deuterium, oxygen and aluminum for thermal neutrons [26, 83]. Conventional units are the Fermi (1 fm = 10^{-13} cm) and the Barn (1 b = 10^{-24} cm^{-2}).

Substance	Mass density (kg/m^3)	SLD ρ_{s} (10^{10} cm^{-2})	Linear attenuation factor μ (cm^{-1})
H_2O	1.00	–0.56	5.392
D_2O	1.07	6.16	0.132
Aluminum	2.70	2.08	0.017

Table 5.2: Scattering length densities (SLD) and attenuation factors for three common substances, calculated using scattering lengths and cross sections listed in table 5.1, number densities obtained from mass densities and molecular weight. A neutron wavelength of λ = 2.09 Å was used to calculate the attenuation factor. See the website `http://www.ncnr.nist.gov` of the Center for Neutron Research of the National Institute of Standards and Technology for further details.

transmission of H_2O is limited primarily due to incoherent scattering, whereas aluminum is nearly transparent for neutrons. It is not a trivial issue to decide which range of sample thicknesses are suitable for a SESANS measurement. A relationship is desired to establish on forehand which thickness gives an optimal signal, given values for attenuation and scattering. In this chapter a criterion is established for the optimal SESANS signal as a function of sample thickness and apparatus parameters. This is reduced to a solvable problem, the solution of which yields the optimal sample thickness ℓ_{opt} in terms of μ and Σ.

5.2 Formalism

5.2.1 Relations

Intensity

A neutron wave function has two possible states of angular momentum, eigenstates with spin $+\frac{1}{2}$ and $-\frac{1}{2}$. A fully polarized neutron beam consists of neutrons with the same combination of eigenstates and has intensity $I_{\uparrow}$. In the SESANS technique an analyzer in front of the detector allows ↑- and ↓-intensities to be counted separately in order to measure the polarization of the beam after the

Sample	Volume fraction ϕ_V	Sample thickness ℓ [cm]	Macroscopic cross section Σ [cm^{-1}]
Liposomes	0.02	1.00	0.036
E. coli	0.09	1.00	0.124
Milk	0.10	1.80	0.046
Yoghurt	0.10	1.80	0.149

Table 5.3: Measured macroscopic coherent scattering cross sections Σ of sols suspended in D_2O. The liposomes and *E. coli* bacteria are biological colloids of which the lipid membranes are observed. Fat-free milk and yoghurt are colloidal food materials that consist of casein micelles. Measurements were performed at a wavelength $\lambda = 0.209 \pm 0.004$ nm, i.e., a monochromatic neutron beam with 2% spread. The systems and experiments are discussed in chapter 2 and chapter 3.

sample. Neutron counts are generally taken to follow a Poisson distribution, for which the count error is given by the square root of the counts. Intensities are calculated by normalizing detector counts with either counting time or monitor counts, which are used to take fluctuations in the neutron flux into account. The counting time can be controlled with very high accuracy and does not contribute to inaccuracy of the measured signal. The monitor counts exceed the number of detector counts by several orders of magnitude and have therefore no significant contribution to signal errors. For a fixed counting time and a constant neutron flux, the errors in intensity therefore become

$$\Delta I_\uparrow = \sqrt{I_\uparrow} \qquad \text{and} \qquad \Delta I_\downarrow = \sqrt{I_\downarrow}. \tag{5.1}$$

Transmission

The constant total transmitted intensity of both states $I_\uparrow + I_\downarrow$ as registered by the detector is I_{tot}. The neutron transmission of a sample is the ratio of this transmitted intensity and the incoming intensity

$$T_N = \frac{I_{\mathrm{tot}}}{I_0}, \tag{5.2}$$

where I_0 is the incoming intensity of the beam without a sample present. The transmission is the fraction of neutrons not attenuated by the sample, which decreases exponentially with sample thickness

$$T_N(\ell) = \mathrm{e}^{-\mu\ell}, \tag{5.3}$$

where μ is the linear attenuation coefficient, which depends on the material and the neutron wavelength (see table 5.2). Combining both relations gives

$$I_{\mathrm{tot}} = I_0\,\mathrm{e}^{-\mu\ell}. \tag{5.4}$$

Polarization

Despite being electrically neutral, neutrons posses a magnetic moment caused by their charged quarks and therefore interact with magnetic fields. The orientation of the magnetic moments is represented by the polarization tensor, of which the diagonal determines the coordinate system, i.e., the frame of reference. In an unpolarized beam of neutrons the magnetic moments are randomly oriented, whereas they all point the same way in a fully polarized neutron beam. The SESANS technique employs polarized neutrons to measure scattering through loss of polarization as a function of spin-echo length z. Very weak signals carry little depolarization and are difficult to distinguish from experimental noise, whereas very strong signals are in the region of full depolarization. When a beam retains only a small amount of polarization, it becomes difficult to measure this amount accurately, which causes an inflation of the measurement errors. The polarization of the beam after traversing a sample is given by

$$P_{\mathrm{S}} = \frac{I_{\uparrow} - I_{\downarrow}}{I_{\uparrow} + I_{\downarrow}} = \frac{I_{\uparrow} - I_{\downarrow}}{I_{\mathrm{tot}}}, \tag{5.5}$$

where the difference between the two intensities depends on z. To determine the error in the polarization, the two intensities can be considered independent of each other, which results in

$$\Delta P_{\mathrm{S}} = \sqrt{\left(\frac{\partial P_{\mathrm{S}}}{\partial I_{\uparrow}}\Delta I_{\uparrow}\right)^2 + \left(\frac{\partial P_{\mathrm{S}}}{\partial I_{\downarrow}}\Delta I_{\downarrow}\right)^2}. \tag{5.6}$$

The partial derivatives are

$$\frac{\partial P_{\mathrm{S}}}{\partial I_{\uparrow}} = \frac{2\,I_{\downarrow}}{{I_{\mathrm{tot}}}^2} \quad \text{and} \quad \frac{\partial P_{\mathrm{S}}}{\partial I_{\downarrow}} = \frac{-2\,I_{\uparrow}}{{I_{\mathrm{tot}}}^2}, \tag{5.7}$$

which gives

$$\Delta P_{\mathrm{S}} = \frac{2\,I_{\uparrow}I_{\downarrow}}{{I_{\mathrm{tot}}}^2}\sqrt{\left(\frac{\Delta I_{\uparrow}}{I_{\uparrow}}\right)^2 + \left(\frac{\Delta I_{\downarrow}}{I_{\downarrow}}\right)^2}. \tag{5.8}$$

The errors in intensity are given by eq. 5.1, resulting in

$$\Delta P_{\mathrm{S}} = \frac{2\,I_{\uparrow}I_{\downarrow}}{{I_{\mathrm{tot}}}^2}\sqrt{\frac{1}{I_{\uparrow}} + \frac{1}{I_{\downarrow}}} = \frac{2}{\sqrt[3]{I_{\mathrm{tot}}}}\sqrt{I_{\uparrow}I_{\downarrow}}. \tag{5.9}$$

Using $I_{\uparrow} = \frac{1}{2}I_{\mathrm{tot}}\,(1 + P_{\mathrm{S}})$ and $I_{\downarrow} = \frac{1}{2}I_{\mathrm{tot}}\,(1 - P_{\mathrm{S}})$ and substituting eq. 5.4 for the total intensity, reduces the error in the polarization to

$$\Delta P_{\mathrm{S}} = \frac{\mathrm{e}^{\frac{\mu}{2}\ell}}{\sqrt{I_0}}\sqrt{1 - {P_{\mathrm{S}}}^2}. \tag{5.10}$$

Projected correlation function

The projected density correlation function is given by

$$G(z) = \frac{\ln P_{\mathrm{N}}(z)}{\Sigma\,\ell} + 1. \tag{5.11}$$

with normalized polarization P_{N}, sample thickness ℓ and macroscopic scattering cross-section Σ. The projected correlation function decays from one to zero, so that $G(0) = 1$ and $G(z \geq z_{\mathrm{sat}}) = 0$. The resolution function of a SESANS setup is given by the polarization of the empty beam P_0, which is divided out of P_{S} to give P_{N}. This normalized polarization starts at one for $z = 0$ and saturates beyond z_{sat}. The fraction of the beam that scatters does not recover its original polarization. The part retaining polarization corresponds to the probability for a neutron not to scatter:

$$P_{\mathrm{sat}} = P_{\mathrm{N}}(z_{\mathrm{sat}}) = \mathrm{e}^{-\Sigma\,\ell}. \tag{5.12}$$

The product $\Sigma\,\ell$ is the scattering power of the sample and determines the strength of the polarization signal. The macroscopic scattering cross section Σ corresponds to the total number of scattering events per volume per time divided by the neutron beam flux in neutrons per area per time, which gives the number of scattering events per neutron per unit sample thickness. It is the product of the squared neutron wavelength λ and the variance and typical size of the SLD fluctuations.

$$\Sigma = \lambda^2 \left\langle \Delta\rho_{\mathrm{s}}^2 \right\rangle \xi \overset{\text{binary}}{=} \lambda^2\, \phi_{\mathrm{V}} (1-\phi_{\mathrm{V}})\, \overline{\Delta\rho_{\mathrm{s}}}^2\, \xi. \tag{5.13}$$

The variance $\left\langle \Delta\rho_{\mathrm{s}}^2 \right\rangle$ is the average squared magnitude of the fluctuations, i.e., the mean squared deviation. For a two phase system it is the product of the two volume fractions and the squared difference between the two scattering length densities present. The typical size of the inhomogeneities is determined by the separation between the SLD fluctuations and characterized by the correlation length ξ.

Assumptions

Although the polarization is in praxis recorded at each z-value for both the empty beam and the beam with a sample in it, the empty beam polarization can in principle also be determined on forehand with high accuracy. At low magnetic field strength the empty beam polarization remains roughly constant and decays towards zero at large z. For purposes of simplification, we consider a theoretical perfect SESANS machine with $P_0 = 1$ and $\Delta P_0 = 0$, which gives $P_{\mathrm{N}} = P_{\mathrm{S}}$ and $\Delta P_{\mathrm{N}} = \Delta P_{\mathrm{S}}$. Since Σ and ℓ are sample properties, the error

in $G(z)$ depends only on the measured polarization. Due to the logarithmic relationship in eq. 5.11, it is given by the relative error in P_S

$$\Delta G(z) = \frac{1}{\Sigma\,\ell}\,\frac{\Delta P_\mathrm{S}(z)}{P_\mathrm{S}(z)}. \tag{5.14}$$

Substitution of the polarization error with eq. 5.10 gives an expression for the error in $G(z)$:

$$\Delta G(z) = \frac{1}{\sqrt{I_0}}\,\frac{\mathrm{e}^{\frac{\mu}{2}\ell}}{\Sigma\,\ell}\,\frac{\sqrt{1-P_\mathrm{S}(z)^2}}{P_\mathrm{S}(z)} \tag{5.15}$$

The dependency of the error in $G(z)$ on the measured polarization is largest for smallest values of P_S. The smallest polarization is generally observed at the saturation level P_sat for large z-values, unless no saturation occurs. Applying eq. 5.12 with $P_\mathrm{S} = P_\mathrm{sat}$ reduces 5.15 to

$$\Delta G_{|z_\mathrm{sat}} = \frac{1}{\sqrt{I_0}}\,\frac{\mathrm{e}^{\frac{\mu}{2}\ell}}{\Sigma\,\ell}\,\sqrt{\mathrm{e}^{2\,\Sigma\,\ell}-1}, \tag{5.16}$$

in which I_0, μ and Σ are properties of machine and sample and can in principle be known *a priori*. This error has a broad minimum as a function of ℓ, which gives a range for the optimal sample thickness. For the case $\mu = 0$ an example is shown in figure 5.2 using a typical values for I_0. Such neutron transparent samples have the smallest measurement error at $\ell = \frac{1}{2}\left(2 + W(-2\mathrm{e}^{-2})\right)/\Sigma \approx 0.8/\Sigma$, where the Lambert W-function is defined as the inverse function for which it holds that $x = W(x)\mathrm{e}^{W(x)}$. The derivative of $\Delta G_{|z_\mathrm{sat}}$ with respect to ℓ is

$$\frac{\partial \Delta G_{|z_\mathrm{sat}}(\ell)}{\partial \ell} = \frac{1}{\sqrt{I_0}}\left[\frac{\Sigma\,\mathrm{e}^{2\,\Sigma\,\ell}}{(\mathrm{e}^{2\Sigma\,\ell}-1)} - \frac{1}{\ell} + \frac{\mu}{2}\right]\frac{\mathrm{e}^{\frac{\mu}{2}\ell}\sqrt{\mathrm{e}^{2\Sigma\,\ell}-1}}{\Sigma\,\ell}. \tag{5.17}$$

At the minimum error this derivative equals zero. The condition for the optimal sample thickness ℓ_opt is therefore

$$\frac{\partial \Delta G_{|z_\mathrm{sat}}(\ell)}{\partial \ell} = 0, \tag{5.18}$$

which needs to be solved for ℓ. This amounts to equating the square bracket term in eq. 5.17 to zero, which reduces to

$$\mu = 2\,\frac{\mathrm{e}^{2\,\Sigma\,\ell_\mathrm{opt}} - \Sigma\,\ell_\mathrm{opt}\,\mathrm{e}^{2\,\Sigma\,\ell_\mathrm{opt}} - 1}{\ell_\mathrm{opt}\left(\mathrm{e}^{2\,\ell_\mathrm{opt}\Sigma} - 1\right)}, \tag{5.19}$$

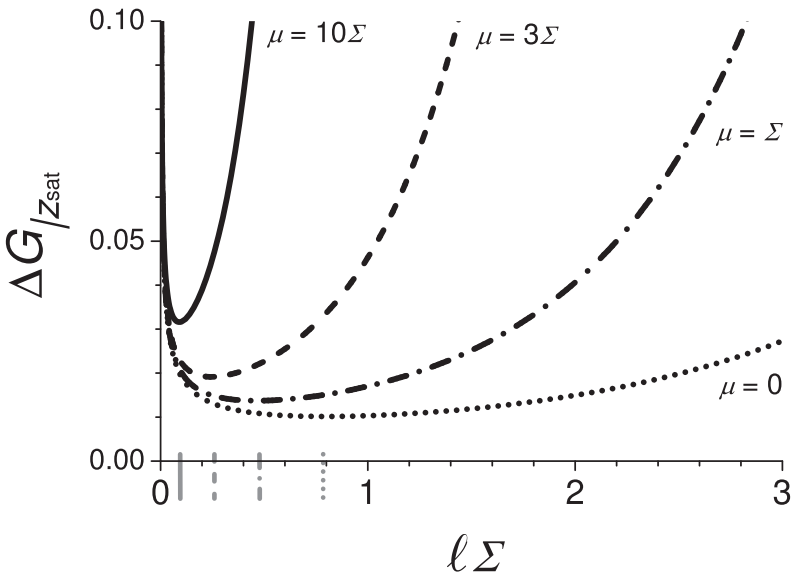

Figure 5.2: Example of the error in G at large z as a function of scattering power for samples with varying attenuation coefficient μ, using a typical empty beam intensity $I_0 = 6{\cdot}10^4$. The gray vertical lines show the position of the minima.

from which ℓ_{opt} cannot be isolated. This result is the inverse of the desired solution, where ℓ_{opt} is a function of μ and Σ. The inverse is easily achieved numerically, which is shown in figure 5.3. In order to find an analytical approximation of the desired result, the error in eq. 5.16 is squared and written as

$$\left(\Delta G_{|z_{\mathrm{sat}}}\right)^2 = \frac{1}{I_0}\,\frac{\mathrm{e}^{\alpha\, s}\left(\mathrm{e}^{2s}-1\right)}{s^2}, \tag{5.20}$$

where $s = \Sigma\,\ell$ and $\alpha = \mu/\Sigma$. The derivative with respect to s is

$$\frac{\partial\left(\Delta G(z)\right)^2}{\partial s} = -\frac{2}{I_0\, s^3}\,\mathrm{e}^{(\alpha+2)\,s}\left[1+\left(\frac{\alpha}{2}-1\right)s+\left(\frac{\alpha}{2}s-1\right)\mathrm{e}^{-2s}\right]. \tag{5.21}$$

Condition 5.18 needs to be solved for s, which amounts to equating the term in the square brackets to zero and expanding the exponential term. The Taylor expansion of e^{-2s} up to fourth order around $s = 0$ reads $1-2s+2s^2-\frac{4}{3}s^3+\frac{2}{3}s^4$, which gives

$$s-(\alpha+2)\;s^2+\left(\alpha+\tfrac{4}{3}\right)\;s^3-\tfrac{2}{3}\,(\alpha+1)\;s^4=0. \tag{5.22}$$

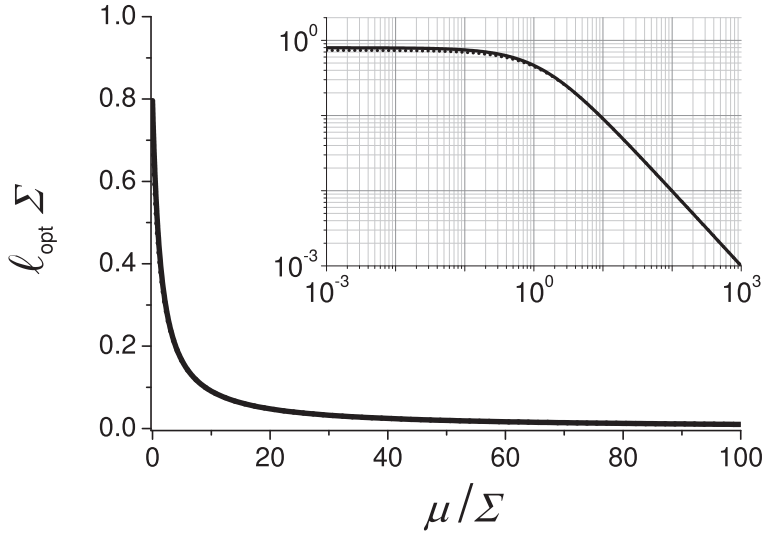

Figure 5.3: The dimensionless optimal sample thickness ℓ as a function of the ratio of the linear attenuation coefficient μ and the macroscopic scattering cross-section Σ. For neutron transparent materials the optimal thickness is roughly $0.8/\Sigma$, whereas it is approximately $1/\mu$ for neutron opaque materials. The approximate analytical expression eq. 5.23 is shown as a dotted line. A double logarithmic plot of the same data is shown in the inset.

The solution is

$$s(\alpha) = \frac{1}{\alpha+2} + \frac{\alpha+\frac{4}{3}}{(\alpha+2)^3} + 2\frac{\left(\alpha+\frac{4}{3}\right)^2}{(\alpha+2)^5} - \frac{2}{3}\frac{\alpha+1}{(\alpha+2)^4}. \tag{5.23}$$

which is also shown in figure 5.3. The optimal thickness is $\ell_{\mathrm{opt}} = s(\frac{\mu}{\Sigma})/\Sigma$. This expression is a good approximation for small μ and nearly exact when $\mu \gtrsim \Sigma$. When $\mu \gg \Sigma$ the material is relatively opaque for neutrons with respect to the amount of scattering. At such large α, the first term in eq. 5.23 is dominant, which gives $\frac{1}{\alpha+2} \Leftrightarrow \ell_{\mathrm{opt}} = \frac{1}{\mu+2\Sigma} \approx \frac{1}{\mu}$. The optimal sample thickness in opaque materials is therefore practically the $1/\mathrm{e}$-length.

5.3 Discussion and conclusions

Although the total transmitted intensity is constant, both ↑- and ↓-intensities are measured separately for increased accuracy, and $\Delta G(z)$ goes with $\sqrt{1-P_{\mathrm{S}}(z)^2}/P_{\mathrm{S}}(z)$ (eq. 5.15). When counting either only $I_{\downarrow}$ or $I_{\uparrow}$ for a known sum I_{tot}, this term changes into the larger terms $\sqrt{2-2P_{\mathrm{S}}(z)}/P_{\mathrm{S}}(z)$ or $\sqrt{2+2P_{\mathrm{S}}(z)}/P_{\mathrm{S}}(z)$ respectively. The error propagation of $G(z)$ has therefore been derived for two independent intensities. The empty beam polarization is in reality not equal to one, but is generally measured with higher accuracy than the sample. The inclusion of P_0 and its error into the error propagation leads to a more complicated and elaborate model, in which P_0 acts as a scaling factor without a large effect on the general conclusions.

The model presented in this chapter gives an estimate of the best thickness for a sample in a SESANS experiment with known attenuation and scattering power. This optimum is found at the minimum of the error in $G(z)$, at which the scattering power is at most 0.8 for any sample thickness. The optimal sample thickness ℓ_{opt} does not depend on the incoming flux, but is a function of the linear attenuation coefficient μ and the macroscopic coherent scattering cross section Σ. Neutron transparent samples have $\mu \ll \Sigma$, in which case only the scattering power is relevant and the optimal sample thickness $\ell_{\mathrm{opt}} \approx 0.8/\Sigma$. When attenuation and scattering power are within one order of magnitude, both make a significant contribution to the optimum. The optimal sample thickness then goes through a transition with ℓ_{opt} ranging from $0.8/\Sigma$ to $0.1/\Sigma$. For $\mu \gg \Sigma$ the sample material is opaque for neutrons and the optimal thickness is determined by attenuation only and given by $\ell_{\mathrm{opt}} \approx \frac{1}{\mu}$.

APPENDIX A

Appendix

A.1 $G(z)$ with a size distribution

Log-normal distribution

EVENTS can occur through a combination of random causes. The multiplicative central limit theorem states that the logarithm of a product of a sufficiently large number of non-negative, independent random variables approaches a normal distribution. Many physical quantities, which can only have positive values, are the products of different random factors. Since the logarithm of a product is equal to the sum of the logarithms of the factors, the product itself approaches a log-normal distribution. In a log-normal probability distribution function (pdf), the natural logarithm of sizes is normally distributed with mean μ and standard deviation σ:

$$\mathrm{pdf}(R;\mu,\sigma) = \frac{\exp\left[-\left(\frac{\ln R-\mu}{\sigma\sqrt{2}}\right)^2\right]}{R\,\sigma\sqrt{2\pi}}. \tag{A.1}$$

The mode is at the peak of the distribution, given by

$$\frac{\mathrm{d}}{\mathrm{d}R}\,\mathrm{pdf}(R;\mu,\sigma) = 0 \;\Rightarrow\; R_{\mathrm{mode}} = \mathrm{e}^{\mu-\sigma^2}. \tag{A.2}$$

The expectation value of an ensemble of sizes $\int_0^\infty R\,\mathrm{pdf}(R;\mu,\sigma)\mathrm{d}R$, is identical to the average radius

$$\langle R\rangle = R_0\,\mathrm{e}^{\sigma^2/2} = \mathrm{e}^{\mu+\sigma^2/2}. \tag{A.3}$$

with error $\langle R\rangle\sqrt{(\Delta\mu)^2+(\sigma\,\Delta\sigma)^2}$. Here R_0 is the median, or the radius separating the higher half of the probability distribution from the lower half. The polydispersity index (PDI) depends only on σ as can be calculated from the width

of the distributed $G(z)$ curve at half height, i.e., for $\frac{P}{P_0}(z_{\mathrm{HWHM}}) = 1 - \frac{1}{2}P_{\mathrm{sat}}$:

$$\mathrm{PDI} = \frac{z_{\mathrm{HWHM}}}{\langle R\rangle} = \frac{\frac{1}{2}\,R_0\,(\mathrm{e}^{\sigma}-1)}{\langle R\rangle} = \frac{1}{2}\,(\mathrm{e}^{\sigma}-1)\,\mathrm{e}^{-\sigma^2/2} \tag{A.4}$$

with error $\frac{1}{2}\left[(1-\sigma)\,\mathrm{e}^{\sigma}+\sigma\right]\mathrm{e}^{-\sigma^2/2}\,\Delta\sigma$. The total probability to find sizes up to radius R is $\int_0^R \mathrm{pdf}(R';\mu,\sigma)\,\mathrm{d}R'$, given by the cumulative distribution function (cdf), which gives

$$\mathrm{cdf}(R;\mu,\sigma) = \frac{1}{2} + \frac{1}{2}\,\mathrm{erf}\left(\frac{\ln R-\mu}{\sigma\sqrt{2}}\right) \tag{A.5}$$

for the log-normal distribution.

Log-normally distributed $G(z)$ – standard

The projected correlation function $G(z)$ can be distributed for a polydisperse system, if a distribution function is specified, such as the log-normal distribution in eq. A.1:

$$\begin{aligned} G_{\mathrm{LN}}(z;\mu,\sigma) &= \int_0^{\infty} G_{\mathrm{SS}}(z;R)\,\mathrm{pdf}(R;\mu,\sigma)\,\mathrm{d}R \\ &= \int_0^{R_{\max}} \frac{G_{\mathrm{SS}}(z;R)}{R\,\sigma\sqrt{2\pi}}\,\exp\left[-\left(\frac{\ln R-\mu}{\sigma\sqrt{2}}\right)^2\right]\mathrm{d}R, \end{aligned} \tag{A.6}$$

where it is evident that for numerical evaluation the upper integration limit cannot be infinity. In stead there should be a cut-off size $R_{\max}$, which should depend on the width of the distribution and for which $\mathrm{cdf}(R_{\max};\mu,\sigma)$ is close to one. Taking any very small, but finite number ε, this largest size can be established from the quantile

$$R_{\max} = \mathrm{e}^{\,\mu+\sigma\sqrt{2}\,\mathrm{inverf}(1-2\varepsilon)}, \tag{A.7}$$

so that $\mathrm{cdf}(R_{\max};\mu,\sigma)$ is close enough to 1 for all realistic values of μ and σ.

Log-normally distributed G(z) – alternate

Substitution of R with $\frac{z}{2\zeta}$ for fixed values of z in eq. A.6 gives $\lim_{R\downarrow 0} G_{\mathrm{LN}}(z) = \lim_{\zeta\to\infty} G_{\mathrm{LN}}(z)$ for small sizes and $\lim_{R\to\infty} G_{\mathrm{LN}}(z) = \lim_{\zeta\downarrow 0} G_{\mathrm{LN}}(z)$ for large sizes. Using

these relations, one may write equation A.6 as

$$\begin{aligned} G_{\mathrm{LN}}(z;\mu,\sigma) &= \int_{\infty}^{0} \frac{G_{\mathrm{SS}}\left(z;\frac{z}{2\zeta}\right)}{\frac{z}{2\zeta}\,\sigma\sqrt{2\pi}}\,\exp\left[-\left(\frac{\ln\frac{z}{2\zeta}-\mu}{\sigma\sqrt{2}}\right)^2\right]\mathrm{d}\left(\frac{z}{2\zeta}\right) \\ &= \frac{1}{\sigma\sqrt{2\pi}}\int_{\infty}^{0}\left(\frac{-z}{2\zeta^2}\right)\frac{2\zeta}{z}\,G_{\mathrm{SS}}\left(2R\zeta;\frac{z}{2\zeta}\right)\exp\left[-\left(\frac{\ln\frac{z}{2\zeta}-\mu}{\sigma\sqrt{2}}\right)^2\right]\mathrm{d}\zeta \\ &= \frac{1}{\sigma\sqrt{2\pi}}\int_{\zeta_{\min}}^{1} G_{\mathrm{SS}}(2\zeta;1)\,\exp\left\{-\left[\left(\frac{\ln\frac{z}{2\zeta}-\mu}{\sigma\sqrt{2}}\right)^2+\ln\zeta\right]\right\}\mathrm{d}\zeta. \end{aligned} \tag{A.8}$$

for which it is evident that the terms in the Kernel equal 0 for all $\zeta > 1$, since $G_{\mathrm{SS}}(z;R) = 0$ for $z > 2R$. Therefore the final result of eq. A.8 requires integration only up to $\zeta = 1$. The lower integration bound $\zeta_{\min}$ in eq. 3.12 can be taken extremely small (10^{-307}), but not zero, limited by the numerical accuracy of the computer and routines used for exponential and logarithm operations. Hence no analytical solution is available and $\zeta_{\min}$ must be established by numerical evaluation of $\lim_{\zeta\downarrow 0}(\mathrm{Kernel})$.

A.2 Determination of the USANS resolution function

The resolution function $R(Q_z)$ was acquired by fitting a sum of three Lorentzian-type functions (eq. A.9) to the reduced data from a reference sample measurement, for negative and positive Q_z-range separately (A.1).

$$R(Q_z) = \frac{R_0}{3}\sum_{i=1}^{3}\frac{1}{(c_i\,Q_z)^{2i}+1}. \tag{A.9}$$

	negative Q_z	positive Q_z
c_1 [nm]	2831 ± 180	3327 ± 109
c_2 [nm]	1483 ± 44	1996 ± 42
c_3 [nm]	3442 ± 155	3031 ± 71
g.o.f.	${\chi_{79}}^2 = 10.1$	${\chi_{294}}^2 = 3.5$

Table A.1: Coefficients for the fitted resolution function with a peak R_0 of 5208 counts per 10 minutes.

A.3 Simulation cycles

The only quantity that explicitly depends on the simulation cycle n_{step}, is the simulated time t. Inverting this relationship gives $n_{\mathrm{step}}(t)$, which is plotted in figure A.1, taken from runs with of $N_0 = 10^5$ monomers and $\phi_{\mathrm{v}} = 0.1$. The result is very similar to fiure 4.11. Plotting N_{m} versus n_{step} gives figure A.2, showing that $N_{\mathrm{m}} \approx n_{\mathrm{step}}/N_0$.

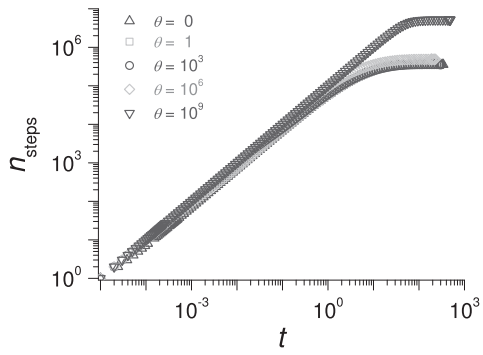

Figure A.1: Relation between simulation cycles n_{step} and simulated time t for varying θ.

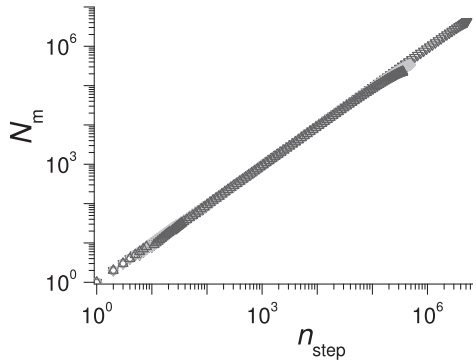

Figure A.2: Comparison between number of moves N_{m} and simulation cycles for varying θ.

Bibliography

1. Koning, G. A. & Krijger, G. C. Targeted Multifunctional Lipid-Based Nanocarriers for Image-Guided Drug Delivery. *Anti-Cancer Agents in Medicinal Chemistry* **7,** 425–440 (2007).
2. Park, J. Liposome-based drug delivery in breast cancer treatment. *Breast Cancer Res* **4,** 95–99 (2002).
3. Kong, G. *et al.* Efficacy of Liposomes and Hyperthermia in a Human Tumor Xenograft Model: Importance of Triggered Drug Release. *Cancer Research* **60,** 6950–6957 (2000).
4. Vasey, P. *et al.* Phase I Clinical and Pharmacokinetic Study of PK1 [N-(2-Hydroxypropyl)methacrylamide Copolymer Doxorubicin]: First Member of a New Class of Chemotherapeutic Agents–Drug-Polymer Conjugates. *Clinical Cancer Research* **5,** 83–94 (1999).
5. Copland, M. *et al.* Liposomal delivery of antigen to human dendritic cells. *Vaccine* **21,** 883–890 (2003).
6. Myhr, G. Multimodal ultrasound mediated drug release model in local cancer therapy. *Medical Hypotheses* **69,** 1325–1333 (2009).
7. Wang, X., Yang, L., Chen, Z. & Shin, D. M. Application of Nanotechnology in Cancer Therapy and Imaging. *CA: A Cancer Journal for Clinicians 58* **58,** 97–110 (2008).
8. Dreher, M. R. & Chilkoti, A. Toward a Systems Engineering Approach to Cancer Drug Delivery. *JNCI Journal of the National Cancer Institute* **99,** 983–985 (2007).
9. Ponce, A. M. *et al.* Magnetic Resonance Imaging of Temperature-Sensitive Liposome Release: Drug Dose Painting and Antitumor Effects. *JNCI Journal of the National Cancer Institute* **99,** 53–63 (2007).
10. Dromi, S. *et al.* Pulsed-High Intensity Focused Ultrasound and Low Temperature Sensitive Liposomes for Enhanced Targeted Drug Delivery and Antitumor Effect. *Clinical Cancer Research* **13,** 2722–2727 (2007).
11. McCabe, B. J. & Previs, S. F. Using isotope tracers to study metabolism: application in mouse models. *Metabolic Engineering* **6,** 25–35 (2004).
12. Briganti, G., R. Giordano AND, P. L. & Pedone, F. SANS measurements on sulfolobus solfataricus ribosome as a function of temperature and magnesium concentration. *Physica B: Condensed Matter* **234-236,** 225–227 (1997).

13. Hammermann, M. *et al.* The diameter of the DNA superhelix decreases with salt concentration: SANS measurements and Monte Carlo simulations. *Journal of Applied Crystallography* **33,** 526–529 (2000).

14. Thiyagarajan, P., Henderson, S. & Joachimiak, A. Solution structures of GroEL and its complex with rhodanese from small-angle neutron scattering. *Structure* **4,** 79–88 (1996).

15. Paganelli, C. & Solomon, A. The rate of exchange of tritiated water across the human red cell membrane. *The Journal of General Physiology* **41,** 259–277 (1957).

16. Mazur, P. Kinetics of Water Loss from Cells at Subzero Temperatures and the Likelihood of Intracellular Freezing. *The Journal of General Physiology* **47,** 347–369 (1963).

17. Herbst, M. & Goldstein, J. A review of water diffusion measurement by NMR in human red blood cells. *AJP - Cell Physiology* **256,** C1097–C1104 (1989).

18. Bu, Z., Wang, L. & Kendall, D. A. Nucleotide Binding Induces Changes in the Oligomeric State and Conformation of Sec A in a Lipid Environment: A Small-angle Neutron-scattering Study. *Journal of Molecular Biology* **332,** 23–30 (2003).

19. Labischinski, H., Goodell, E., Goodell, A. & Hochberg, M. Direct proof of a "more-than-single-layered" peptidoglycan architecture of Escherichia coli W7: a neutron small-angle scattering study. *The Journal of Bacteriology* **173,** 751–756 (1991).

20. Svergun, D. *et al.* Protein hydration in solution: Experimental observation by x-ray and neutron scattering. *Proceedings of the National Academy of Sciences of the United States of America* **95,** 2267–2272 (1998).

21. Czajka, D. M., Finkel, A. J., Fischer, C. S. & Katz, J. J. Physiological effects of deuterium on dogs. *AJP - Legacy* **201,** 357–362 (1961).

22. Schloerb, P. R., Friis-Hansen, B. J., Edelman, I. S., Solomon, A. & Moore, F. D. The measurement of total body water in the human subject by deuterium oxide dilution with a consideration of the dynamics of deuterium distribution. *The Journal of Clinical Investigation* **29,** 1296–1310 (1950).

23. Nagle, J. F. & Tristram-Nagle, S. Structure of lipid bilayers. *Biochimica et Biophysica Acta* **1469,** 159–195 (2000).

24. Takeuchi, S., DiLuzio, W. R., Weibel, D. B. & Whitesides, G. M. Controlling the Shape of Filamentous Cells of Escherichia coli. *Nano Letters* **5,** 1819–1823 (2005).

25. Pencer, J., Jackson, A., Kuèerka, N., Nieh, M.-P. & Katsaras, J. The influence of curvature on membrane domains. *Eur Biophys J* **37,** 665–671 (2008).

26. Sears, V. F. Neutron scattering lengths and cross sections. *Neutron News* **3,** 29–37 (1992).

27. Krouglov, T. *et al.* Structural transitions of hard-sphere colloids studied by spin-echo small-angle neutron scattering. *Journal of Applied Crystallography* **36,** 1417–1423 (2003).

28. Andersson, R., Bouwman, W., Luding, S. & de Schepper, I. Stress, strain and bulk microstructure in a cohesive powder. *Physical Review E* **77,** 051303 (2008).

29. Rekveldt, M. T. *et al.* Spin-echo small angle neutron scattering in Delft. *Review of Scientific Instruments* **76,** 033901 (2005).

30. Gähler, R., Golub, R., Habicht, K., Keller, T. & Felber, J. Space-time description of neutron spin echo spectrometry. *Physica B* **229,** 1–17 (1996).

31. Bouwman, W. G. *et al.* Real-space neutron scattering methods. *Nuclear Instruments and Methods in Physics Research A* **586,** 9–14 (2008).

32. Andersson, R. A., van Heijkamp, L. F., de Schepper, I. M. & Bouwman, W. G. Analysis of spin-echo small-angle neutron scattering measurements. *Journal of Applied Crystallography* **41,** 868–885 (2008).

33. van Heijkamp, L. F. *et al.* Milk Gelation Studied with Small Angle Neutron Scattering Techniques and Monte Carlo Simulations. *J, Phys. Chem. A* **114,** 2412–2426 (2010).

34. de Kruif, C. Supra-aggregates of Casein Micelles as a Prelude to Coagulation. *Journal of Dairy Science* **81,** 3019–3028 (1998).

35. de Kruif, C. Casein micelle interactions. *International Dairy Journal* **9,** 183–188 (1999).

36. Andersson, V. J. & Lekkerkerker, H. N. Insights into phase transition kinetics from colloid science. *Nature* **416,** 811–815 (2002).

37. Lagaude, A., Fernandez, L., Cuq, J.-L. & Marchesseau, S. Characterization of curd formation during the rennet coagulation of milk by an optical microscopic method. *International Dairy Journal* **14,** 1033–1039 (2004).

38. Lehner, D. *et al.* Characterization of Enzymatically Induced Aggregation of Casein Micelles in Natural Concentration by *in Situ* Static Light Scattering and Ultra Low Shear Viscosimetry. *J. Colloid Interface Sci.* **213,** 445–456 (1999).

39. de Campo, L. *et al.* Five Component Food-Grade Microemulsions: Structural Characterization by SANS. *J. Colloid Interface Sci.* **274,** 251–267 (2004).

40. Hemar, Y., Singh, H. & Horne, D. Determination of early stages of rennet-induced aggregation of casein micelles by diffusing wave spectroscopy AND rheological measurements. *Current Applied Physics* **4,** 362–365 (2003).

41. Krouglov, T., Kraan, W. H., Plomp, J., Rekveldt, M. T. & Bouwman, W. G. Spin-echo small-angle neutron scattering to study particle aggregates. *Journal of Applied Crystallography* **36,** 816–819 (2003).

42. Jericha, E. *et al.* Ultra-small-angle neutron scattering studies of artificial lattices. *Journal of Applied Crystallography* **36,** 778–782 (2003).

43. Tromp, R. H. & Bouwman, W. G. A novel application of neutron scattering on dairy products. *Food Hydrocolloids* **21,** 154–158 (2007).

44. Bouwman, W. G., Pynn, R. & Rekveldt, M. T. A Comparison of the Performance of SANS and SESANS. *Physica B* **350,** E787–E790 (2004).

45. Gimel, J., Durand, D. & Nicolai, T. Transition between flocculation and percolation of a Diffusion-Limited Cluster-cluster Aggregation process using three-dimensional Monte Carlo simulation. *Physical Review B* **51,** 11348–11358 (1995).

46. Gimel, J., Nicolai, T. & Durand, D. 3D Monte Carlo Simulations of Diffusion Limited Cluster Aggregation up to the Sol-Gel Transition: Structure AND Kinetics. *Journal of Sol-Gel Science and Technology* **15,** 129–136 (1999).

47. Rottereau, M., Gimel, J., Nicolai, T. & Durand, D. Monte Carlo simulation of particle aggregation and gelation: I. Growth, structure and size distribution of the clusters. *The European Physical Journal* **E,** 133–140 (2004).

48. Rottereau, M., Gimel, J., Nicolai, T. & Durand, D. Monte Carlo simulation of particle aggregation and gelation: II. Pair correlation function and structure factor. *The European Physical Journal* **E,** 141–148 (2004).

49. Krouglov, T., de Schepper, I. M., Bouwman, W. G. & Rekveldt, M. T. Real-space interpretation of spin-echo small-angle neutron scattering. *Journal of Applied Crystallography* **36,** 117–124 (2003).

50. van Hove, L. Correlations in Space and Time and Born Approximation Scattering in Systems of Interacting Particles. *Physical Review* **95,** 249–262 (1954).

51. Sapoval, B. *Universalités et fractales* (Flam-marion-Champs, France, 2001).

52. Meakin, P. & Family, F. Structure and dynamics of Reaction Limited Aggregation. *Physical Review A* **36,** 5498–5501 (1987).

53. Klimeš, L. Correlation Functions of Random Media. *Pure and Applied Geophysics* **159,** 1811–1831 (2002).

54. Klimeš, L. Estimating the Correlation Function of a Self-affine Random Medium. *Pure and Applied Geophysics* **159,** 1833–1853 (2002).

55. de Kruif, C. Skim Milk Acidification. *Journal of Colloid and Interface Science* **185,** 19–25 (1997).

56. *CRC Handbook of chemistry and physics* 80th (ed David R. Lide, E.-i.-C.) 1–2326 (CRC Press, Boca Raton, 1999, 1976).

57. Strobl, M. *et al.* The new V12 ultra-small-angle neutron scattering and tomography instrument at the Hahn-Meitner Institut. *Applied Crystallography* **40,** s463–s465 (2006).

58. Vicsek, T. in 1–495 (World Scientific, 1989).

59. Kruglov, T. Correlation function of the excluded volume. *Journal of Applied Crystallography* **38,** 716–720 (2005).

60. Vétier, N., Banon, S., Chardot, V. & Hardy, J. Effect of Temperature and Aggregation Rate on the Fractal Dimension of Renneted Casein Aggregates. *Journal of Dairy Science* **86,** 2504–2507 (2003).

61. Dickinson, E. Structure formation in casein-based gels, foams, and emulsions. *Colloids and Surfaces A: Physiochem. Eng. Aspects* **288,** 3–11 (2006).

62. Ruis, H. G., Venema, P. & van der Linden, E. Relation between pH-induced stickiness and gelation behaviour of sodium caseinate aggregates as determined by light scattering and rheology. *Food Hydrocolloids* **21,** 545–554 (2007).

63. Mezzenga, R., Schurtenburger, P., Burbidge, A. & Michel, M. Understanding foods as soft materials. *Nature Materials* **4,** 729–740 (2005).

64. Dawson, K. The glass paradigm for colloidal glasses, gels, and other arrested states driven by attractive interactions. *Current Opinion in Colloid & Interface Science* **7,** 218 (2002).

65. Sciortino, F. Disordered materials - One liquid, two glasses. *Nature Materials* **1,** 145–146 (2002).

66. Sciortino, F. & Tartaglia, P. Glassy colloidal systems. *Advances in Physics* **54,** 471–524 (2005).

67. Zaccarelli, E. Colloidal gels: equilibrium and non-equilibrium routes (Topical Review). *Journal of Physics: Condensed Matter* **19,** 323101 (50pp) (2007).

68. Taboada-Serrano, P., Chin, C.-J., Yiacoumi, S. & Tsouris, C. Modeling aggregation of colloidal particles. *Current Opinion in Colloid & Interface Science* **10,** 123–132 (2005).

69. Ettelaie, R. Computer simulation and modeling of food colloids. *Current Opinion in Colloid & Interface Science* **8,** 415–421 (2003).

70. Deng, Y. & Blöte, H. W. Monte Carlo study of the site-percolation model in two and three dimensions. *Phys. Rev. E* **72,** 016126 (2005).

71. Stauffer, D. & Aharony, A. in 2nd 1–181 (Taylor and Francis, 1992).

72. Meakin, P. A historical introduction to computer models for fractal aggregates. *Journal of Sol-Gel Science and Technology* **15,** 97–117 (1999).

73. Lattuada, M., Wu, H. & Morbidelli, M. Radial density distribution of fractal clusters. *Chemical Engineering* **59,** 4401–4413 (2004).

74. Hütter, M. Local structure in particle network formation studied by Brownian Dynamics simulation. *Journal of Colloid and Interface Science* **231,** 337–350 (2000).

75. Flory, P. J. Molecular Size Distribution in Three Dimensional Polymers. I. Gelation. *Journal of the American Chemical Society* **63,** 3083–3090 (1941).

76. Stockmayer, W. H. Theory of Molecular Size Distribution and Gel Formation in Branched-Chain Polymers I. *Journal of Chemical Physics* **11,** 45–55 (1943).

77. Stockmayer, W. H. Theory of Molecular Size Distribution and Gel Formation in Branched Polymers II. General Cross Linking. *Journal of Chemical Physics* **12,** 125–132 (1944).

78. Lu, P. J. *et al.* Gelation of particles with short-range attraction. *Nature* **453,** 499–504 (2008).

79. Lin, M. *et al.* The Structure of Fractal Colloidal Aggregates of Finite Extent. *Journal of Colloid and Interface Science* **137,** 263–280 (1990).

80. Luijten, E. & Blöte, H. W. Monte Carlo method for spin models with long-range interactions. *Int. J. Mod. Phys. C* **6,** 359–370 (1995).

81. Magee, J. E., Dutton, H. & Siperstein, F. R. CaSPA - an algorithm for calculation of the size of percolating aggregates. *Computer Physics Communications* **180,** 1503–1510 (2009).

82. Zhao, H. Radial distribution functions in liquids and fractal aggregates. *Chem. Eng. Comm.* **192,** 145–154 (2005).

83. *Landolt-B ornstein* New Series I/16 A (ed Schopper, H.) (Springer, Berlin, 2000).

List of publications

Main author:

- *From Reaction to Diffusion Limited Cluster-cluster Aggregation in 3D Monte Carlo with increasing reactivity,*
  Léon F. van Heijkamp, Jouke R. Heringa,
  Ignatz M. de Schepper, Wim G. Bouwman,
  to be submitted to the Journal of Colloid and Interface Science.

- *Spin-Echo Small Angle Neutron Scattering analysis of liposomes and bacteria,*
  Léon F. van Heijkamp, Ana-Maria Sevcenco, Diane Abou, Remko van Luik, Gerard C. Krijger, Peter-Leon Hagedoorn, Ignatz M. de Schepper, Bert Wolterbeek, Gerben A. Koning, Wim G. Bouwman,
  Journal of Physics Conference Series **247** (2010) 012016.

- *Milk gelation studied with SANS techniques and Monte Carlo simulations,*
  Léon F. van Heijkamp, Ignatz M. de Schepper, Markus Strobl, R. Hans Tromp, Jouke R. Heringa and Wim G. Bouwman,
  Journal of Physical Chemistry A **114** (2010) 2412-2426.

Co-author:

- *Modeling of worm-like micelle formation in oil-water-surfactant systems,*
  K. Kowlgi, L.F. van Heijkamp, G. Koper,
  under preparation.

- *Analysis of Spin-Echo Small Angle Neutron Scattering measurements,*
  R.A. Andersson, L.F. van Heijkamp, I.M. de Schepper, W.G. Bouwman,
  Journal of Applied Crystallography **41** (2008) 868-885.

Summary

REGULAR materials are composed of condensed phases, such as solids and liquids, with a huge number of constituents. Soft condensed matter systems are compact materials with structures that are much larger than molecular length scales and dynamics that are much slower, but still subject to thermal fluctuations. These substances are often sensitive to external fields such as electric fields, shear or gravity. These include colloids, such as sols, gels and foams, but also granular matter, polymers and a variety of biological materials. Since the wavelength range of the visible light spectrum exceeds the colloidal size range, optical microscopy generally does not have the resolution to observe colloidal materials. High-resolution imaging techniques like electron microscopy are usually unsuitable for sensitive materials like biological compounds. However, various non-invasive scattering techniques are able to probe colloidal length scales.

Many organic colloidal materials such as a lot of food products, are concentrated and opaque, which is a disadvantage for light scattering techniques. Such materials and biological compounds consist largely of hydrogen, carbon and oxygen atoms, and to a lesser extent of nitrogen, phosphor and sulfur atoms. The smallest functional biological units are cells, which have a high water content. These types of colloids therefore have relatively low electron densities, providing little contrast for X-rays. Neutron techniques are complementary to the more common X-ray techniques. Neutrons have atomic wavelengths like X-ray photons, but interact with atomic nuclei and have very different scattering properties. Free neutrons are matter waves with a wavelength inversely proportional to their speed and penetrate deeply into matter. A big advantage is the very different neutron interaction between hydrogen and deuterium, which allows control over the scattering power of biological samples. Measurements in this study have used varying amounts of light and heavy water (H_2O and D_2O), which is a facile method for tunable contrast. The colloidal structures under investigation are large compared to the neutron wavelength, causing scattering over small angles. The movement of the colloidal particles is extremely slow compared to neutron speeds. Therefore neutrons scatter elastically, changing direction but not momentum, resolving the static structure

factor. To measure the structure of materials under investigation in this work, such non-time-resolved techniques were used.

This thesis discusses two types of Small Angle Neutron Scattering (SANS) techniques, which have been used to investigate the structure of colloidal suspensions and gels. Spin-Echo Small Angle Neutron Scattering (SESANS) has been used as the main technique, and Ultra Small Angle Neutron Scattering (USANS) as the secondary. SESANS probes length scales by measuring the loss of polarization of a neutron beam as a gauge for scattering. The shape of a SESANS signal gives the Abel transform of the density-density correlation function of a sample. This is the projection in one spatial dimension of the inverse Fourier transform of the static structure factor. USANS measures a projection of the scattering function, performing an integration over one coordinate in momentum space. USANS measurements therefore yield the inverse-space equivalent of SESANS measurements, which is demonstrated in this thesis by comparison of measurements on the same samples.

SESANS resolves length scales over three orders of magnitude in size, which has been applied to spherical colloidal particles. For monodisperse solid particles, a SESANS signal is described by the particle diameter and the variance in scattering length densities (SLD) between colloid and medium. The particle size determines the width of the signal and the scattered intensity, through the correlation length. SESANS can distinguish between solid and hollow spheres. Hollow spheres are spherical particles with a homogeneous SLD throughout the shell and a core, which is identical to the medium. Filled spheres are hollow spheres with a third phase as a core, observable for sufficiently large contrast with both shell and medium. The hollow sphere correlation function exhibits features distinctly different from the solid sphere correlation function. Monodisperse hollow spheres can be distinguished from solid spheres for a range of shell thicknesses within the resolvable range of SESANS and well below the particle radius. The scattering contrast of hollow spheres is between shell and medium, whereas it is between core and medium for solid spheres. This has been used to establish hollow sphere nature of monodisperse biological colloids, prepared in H_2O, and resuspended D_2O, finding that SESANS measurement time exceeded the exchange time of light and heavy water across the membranes. Diameters around 160 nm have been found for two types of liposomes and around 800 nm for *E. coli* bacteria, all with shell thicknesses somewhere around 10 nm. These results are all in good agreement with literature, although SESANS cannot accurately measure the thickness of such thin membranes. Dynamic Light Scattering (DLS) has been used to confirm their narrow size distributions. Processes with slower exchange of H_2O and D_2O are in principle observable when on a timescale of hours. This makes SESANS an additional technique that can

be used as an alternative to tritium (T_2O) techniques in drug targeting studies for cancer treatment.

Size distributions of polydisperse spherical particles can be extracted from SESANS data. An optimized procedure is described for a log-normal size distribution, with which to fit the average size and distribution width. This procedure has been applied to measurements on fat-free milk samples as the casein micelles are polydisperse particles with a wide range of sizes. The destabilization of colloidal particles causes them to flocculate and gelate. Gelation occurs when a discrete solid phase suspended in a liquid phase, becomes continuous and forms a macroscopic network structure that encapsulates the liquid. This rearrangement of the particle configuration increases the scattered intensity and shifts it to smaller scattering angles. The kinetics of milk to yoghurt gelation have been studied from the changing SESANS and USANS signals and modeled as growing self-affine structures and fractal-like aggregates, characterized by typical length scales and a dimensionality. SESANS measurement data on casein micelles of milk have shown an average diameter around 250 nm with 50% polydispersity index, both in good agreement with literature, whereas without modeling data with a size distribution the diameter would be significantly smaller. Simulations of particles have been employed to create gelated structures using varying stickiness. The numerical density correlation functions and numerical correlation lengths have been calculated from these structures, for direct comparison with the measurement data. At low stickiness the correlation length increases more than three times, in good agreement with neutron scattering observations on milk gelation. However, the longest length scales in yoghurt as observed by SESANS, were not accurately simulated by the model.

This thesis also presents a more extensive study of gelation with 3D Monte Carlo (MC) simulations, using adhesive particles performing Brownian motion and using a global reactivity. The particles move randomly on a periodic grid and bond randomly, forming branched clusters, until one large structure remains. A changing reactivity is used for initially stable configurations of particles to model gradually destabilizing colloidal suspensions. The aggregation of particles into large clusters corresponds to flocculation in real systems, whereas the aggregation of clusters gives rise to a percolating fractal structure that extends throughout the whole system. After the remaining clusters have aggregated onto the percolating backbone, the solid phase is continuous in all directions. This corresponds to fully gelated real systems. Varying degrees of reactivity increase are used for different monomer concentrations to investigate the effects on aggregation, where the reaction rate determines the aggregation regime. At low reactivity the process is Reaction Limited Cluster–cluster Aggregation (RLCA), whereas at high reactivity the cluster mobility is the restricting factor and the process becomes Diffusion Limited Cluster–cluster Aggregation

(DLCA). The formation of large clusters slows aggregation down due to their inertia. In DLCA this causes a separation between percolation and gelation time, which is a multitude of the percolation time. At low reactivity aggregation occurs very slowly from the start, as particles move around with marginal bond formation, resulting in large increases in percolation and gelation time. Two MC algorithms are presented to speed up the simulation regardless of regime. One algorithm circumvents unnecessary evaluations for the scarce movement of heavy clusters and the other avoids needless computing of sporadic bond formation for low reactivities.

In this study a transition is seen from RLCA to DLCA if the typical reaction time is below typical monomer diffusion time. Simulation proceeds beyond percolation until all clusters have aggregated. Once typical reaction time exceeds typical diffusion time, lowering the reactivity increases percolation and gel time. At such low reactivities cluster mobility is prolonged and cluster mass distributions remain narrower. This allows the coordination number to increase more before bonding than in DLCA and results in denser gels with more bonds. The coordination number is the average number of nearest particles neighbors surrounding each particle. On a cubic lattice there are six nearest positions. Dilute systems start with coordination numbers equal to six times the volume fraction, whereas concentrated systems have slightly larger values. At high and quickly increasing reactivities, DLCA gel structures consistently reach coordination numbers between 2.2 and 3.1 for concentrations increasing from 0.01 to 0.5. When leaving the DLCA regime these values increase. The largest values have been observed at the lowest reactivity, which ranged from 2.7 to 3.6 for the same volume fraction range. A maximum coordination number has not yet been established. The theoretical maximum of six would give a crystal structure, which would require nucleation type simulations at extremely low reactivities. This will clearly never be reached in cluster–cluster aggregation, as cavities inside the branched structures will always occur due to the random nature of the process. The increased denseness is also demonstrated by the decreased radii of gyration and the development of the radial distribution function of gel structures, which show larger accumulation of mass and larger pore sizes. This confirms the larger increase in correlation length during reaction limited aggregation, as observed in the milk–yoghurt gelation study.

The polarization signal in a SESANS measurement is composed of the projected correlation function, where the strength of the signal is determined by the scattered fraction of the beam. The quality of the signal is determined by the incoming flux, the linear attenuation coefficient, the scattering cross section and the sample thickness. A relationship has been derived between the error in the correlation function and the sample thickness. The optimal sample thickness is found at the minimum error and does not depend on the incoming flux, but is

a function of scattering cross-section and attenuation coefficient. For samples with high neutron transparency, the minimum error is at an average number of close to 0.8 scattering events. When the attenuation coefficient comes to within one order of magnitude of the scattering cross section, the optimal number of scattering events drops to 0.1. When the attenuation coefficient is ten or more times the cross section, it becomes the dominant factor in signal quality. In samples with such relatively high neutron opacity, the optimal thickness is the $1/\mathrm{e}$-length.

Samenvatting

TYPISCHE vaste en vloeibare materialen bestaan uit dichte fases met een enorm aantal componenten. Zachte gecondenseerde materie is een groep dichte materialen met structuren groter dan de lengteschalen van moleculen, maar tragere dynamica en onderhevig aan thermische fluctuaties. Vaak is er sprake van een gevoeligheid voor externe velden, zoals elektrische velden, afschuifkrachten en zwaartekracht. Onder deze stoffen vallen colloïdale materialen in de hoedanigheid van bijvoorbeeld sol, gel of schuim, maar ook granulaire materialen, polymeren en een verscheidenheid aan biologische materialen. Het spectrum van zichtbaar licht bestaat uit golflengtes die overlappen met de colloïdale lengteschalen, zodat deze deeltjes niet met conventionele microscopie geobserveerd kunnen worden. Hoge resolutie technieken zoals elektronenmicroscopie zijn echter ongeschikt voor de vaak gevoelige biologische materialen. Verstrooiingstechnieken zijn niet-invasief en in staat om structuren op colloïdale schaal te meten.

Organische colloïden zijn dikwijls geconcentreerd en ondoorzichtig, zoals veel levensmiddelen, wat een belemmering is voor technieken met lichtverstrooiing. Dergelijke materialen en biologische verbindingen bestaan grotendeels uit waterstof, koolstof en zuurstof atomen en in mindere mate ook uit stikstof, fosfor en zwavel atomen. Cellen zijn de kleinste functionele biologische eenheden en bevatten veel water. Dit soort colloïden hebben derhalve een lage elektrondichtheid, wat weinig contrast voor röntgen-straling oplevert. Neutronenverstrooiing wordt daarom als complementaire techniek toegepast. Neutronen hebben net als röntgen-fotonen golflengtes op atomaire schaal, maar zijn gevoelig voor atoomkernen en verstrooien derhalve op geheel andere wijze. Vrije neutronen dringen diep door in materie en zijn massagolven met golflengtes omgekeerd evenredig aan de snelheid. Het grote verschil tussen de interactie met waterstof en met deuterium is een belangrijk voordeel, omdat het controle geeft over de mate waarin biologische materialen verstrooien. Voor dit onderzoek zijn wisselende hoeveelheden licht en zwaar water (H_2O en D_2O) gebruikt om het contrast van monsters in te stellen. De onderzochte colloïdale deelt-

jes zijn groot ten opzichte van de neutronengolflengte, waardoor de neutronen over kleine hoeken verstrooien. De colloïdale deeltjes bewegen met verwaarloosbare snelheid ten opzichte van de neutronen, zodat de neutronen alleen van richting en niet van snelheid veranderen. Deze elastische verstrooiing geeft tijdonafhankelijke informatie over de structuur van materialen. In dit onderzoek is elastische neutronenverstrooiing gebruikt om de statische structuurfactor te bepalen.

Dit proefschrift behandelt Spin-Echo SANS (SESANS) en Ultra-SANS (USANS), twee technieken waarbij neutronen over kleine hoeken worden verstrooid. Deze technieken zijn gebruikt om de structuren van colloïdale suspensies en gels te bestuderen. Lengteschalen worden geobserveerd met SESANS door het verlies van polarisatie van een neutronenbundel te bepalen als een maat voor de hoeveelheid verstrooiing. De vorm van een SESANS signaal levert de Abel transformatie van de dichtheid-correlatiefunctie van een materiaal op. Dit is gelijk aan de projectie op een vlak van de inverse Fourier-getransformeerde statische structuurfactor. Met USANS wordt een projectie van de verstrooide intensiteit gemeten, waarbij over één momentum-dimensie wordt geïntegreerd. USANS is derhalve het inverse-ruimte equivalent van SESANS, wat in dit proefschrift aangetoond wordt middels een vergelijking van beide type metingen aan dezelfde materialen.

SESANS kan drie ordes van grootte in lengteschaal onderscheiden, wat toegepast is op bolvormige colloïdale deeltjes. In het geval van monodisperse vaste deeltjes wordt een SESANS signaal beschreven aan de hand van de deeltjesdiameter en de variantie in verstrooiingslengte-dichtheid (SLD) tussen de colloïden en het medium. De deeltjesgrootte bepaalt de wijdte van het signaal, alsmede de intensiteit middels de correlatielengte. SESANS kan solide en holle bollen onderscheiden. Holle bollen zijn bolvormige deeltjes bestaande uit een schil met een homogene SLD en een kern gevuld met medium. Gevulde bollen zijn holle bollen waarvan de kern een derde fase bevat, wat bij voldoende contrast met zowel schil als medium tot uitdrukking komt. De correlatiefunctie voor holle bollen heeft kenmerken die duidelijk afsteken van de correlatiefunctie voor solide bollen. Monodisperse holle bollen kunnen worden onderscheiden voor schildiktes binnen het meetbereik van SESANS mits significant kleiner dan de bolradius. Het contrast is tussen schil en medium, waar het tussen kern en medium is in het geval van solide bollen. Dit is toegepast om het holle bolkarakter te bepalen van suspensies in D_2O van biologische colloïden bereid in H_2O. De uitwisseling van licht en zwaar water is sneller gebleken dan de benodigde meettijd voor SESANS. Voor twee soorten liposomen zijn diameters rond de 160 nm vastgesteld en rond de 800 nm voor *E. coli* bacteriën, allen met schildiktes rond de 10 nm. Deze resultaten stemmen overeen met literatuurwaarden, hoewel met SESANS de diktes van dergelijk dunne membranen niet

nauwkeurig kan worden bepaald. Middels dynamische lichtverstrooiing (DLS) is de deeltjesgrootteverdeling van de liposomen en bacteriën bepaald, hetgeen bevestigde dat de monsters nagenoeg monodispers waren. Tragere uitwisseling van H_2O en D_2O over biologische membranen kan worden waargenomen als deze processen enkele uren vergen. SESANS kan daarom worden gebruikt als een toevoeging op bestaande technieken en als een alternatief voor het gebruik van tritium in zogeheten drug-targeting studies voor kankerbehandeling.

De grootteverdeling van polydisperse deeltjes kan uit SESANS data bepaald worden. Een geoptimaliseerde procedure wordt beschreven voor een log-normaal distributie waarmee de gemiddelde grootte en de wijdte van de distributie vastgesteld kunnen worden. Dit is toegepast op meetdata van vetvrije melk, omdat de polydisperse caseïne micellen een groot bereik aan diameters kunnen aannemen. Door het destabiliseren van deze colloïdale deeltjes treden flocculatie en gelatie op. Een discrete vaste fase, die gesuspendeerd is in een vloeistof, wordt tijdens gelatie continu en vormt een macroscopische netwerkstructuur die de vloeistof inkapselt. Deze herschikking van de deeltjesconfiguratie vergroot de verstrooide intensiteit en verschuift deze naar kleinere hoeken. De kinetiek van melk-yoghurt gelatie is bestudeerd aan de hand van de verandering in SESANS en USANS signalen. Het gelatieproces is gemodelleerd als het groeien van zelf-affine structuren en fractale aggregaten, gekarakteriseerd door typische lengtes en dimensionaliteiten. SESANS meetdata van melk toonden dat caseïne micellen een gemiddelde diameter van rond de 250 nm hadden met een polydispersiteitsindex van 50%, in goede overeenstemming met literatuur, waar modelleren zonder deeltjesgroottedistributie een significant kleinere diameter opleverde. Simulaties met deeltjes met wisselende plakkerigheid zijn gebruikt om verschillende gelstructuren te creëren. De numerieke dichtheid-correlatiefunctie en numeriek correlatielengte van deze structuren zijn berekend om te vergelijken met de meetdata. Bij lage plakkerigheid wordt de correlatielengte meer dan drie maal zo groot tijdens gelatie, wat goed overeenkomt met de observaties van de neutronenverstrooiing aan de melk-gelatie. De langste lengteschalen waargenomen met SESANS in yoghurt, kunnen echter niet met dit model gereproduceerd worden.

Een grondigere studie van colloïdale gelatie via Monte Carlo simulaties (MC) in 3D komt in dit proefschrift ook aan bod, waarbij gebruik wordt gemaakt van deeltjes met Browniaanse diffusie en een globale reactiviteit. De deeltjes bewegen willekeurig op een periodiek rooster en vormen arbitrair bindingen met elkaar, zodat vertakte clusters ontstaan totdat uiteindelijk één grote structuur overblijft. Stabiele configuraties van deeltjes worden aan een veranderlijke reactiviteit blootgesteld om geleidelijk destabiliserende colloïdale suspensies na te bootsen. Het ontstaan van grote clusters van geaggregeerde deeltjes komt overeen met flocculatie in echte systemen, terwijl de aggregatie van clusters tot

de vorming van een percolerende fractale structuur leidt die het hele systeem bestrijkt. Nadat de overgebleven clusters op dit percolerende skelet zijn geaggregeerd, is de vaste fase continu geworden in alle richtingen. Dit komt overeen met volledig geleerde echte systemen. Het effect op de aggregatie van het variëren van de toename in reactiviteit in systemen met wisselende monomeer concentraties wordt bestudeerd, waar de reactiesnelheid het aggregatie regime bepaalt. Bij lage reactiviteit is het proces reactiegelimiteerde cluster–cluster aggregatie (RLCA), terwijl bij hoge reactiviteit the cluster mobiliteit de beperkende factor is en het proces diffusie gelimiteerde cluster–cluster aggregatie (DLCA) wordt. De formatie van grote clusters vertraagt de aggregatie vanwege hun inertie. In DLCA is de gelatietijd derhalve een veelvoud van de percolatietijd. Bij lage reactiviteit verloopt aggregatie vanaf het begin al langzaam, omdat de bewegende deeltjes maar beperkt bindingen vormen, wat zowel de percolatie als de gelatie vertraagt. Twee MC algoritmes worden besproken om de simulatie te versnellen ongeacht het aggregatie regime. Het eerste algoritme vermijdt onnodige evaluaties van de infrequente bewegingen van de zware clusters, het tweede voorkomt overtollige berekeningen als de formatie van bindingen schaars is door lage reactiviteit.

Deze studie laat een overgang zien van RLCA naar DLCA als de typische reactietijd kleiner is dan de typische diffusietijd. De simulatie gaat na percolatie door totdat alle clusters geaggregeerd zijn. Zodra de typische reactietijd de typische diffusietijd overstijgt, zal het verder verlagen van de reactiviteit percolatie en gelatie vertragen. Dergelijk lage reactiviteit verlengt de clustermobiliteit en vernauwt de clustermassadistributie. Hierdoor kan het coördinatiegetal verder toenemen voordat het door bindingen wordt vastgelegd, wat resulteert in dichtere gels met meer bindingen. Het coördinatiegetal is het gemiddeld aantal naburige deeltjes. Op een kubisch rooster kan een deeltje zes dichtstbijzijnde buren hebben. Verdunde systemen hebben initieel een coördinatiegetal van zes maal de volume fractie, wat bij hogere concentraties iets hoger komt te liggen. Bij hoge en snel-stijgende reactiviteit hebben DLCA gelstructuren stelselmatig coördinatiegetallen tussen de 2.2 en 3.1 voor concentraties met volumefracties van 0.01 tot 0.5. Buiten het DLCA regime worden deze waardes hoger. Bij de laagste reactiviteit zijn de hoogste coördinatiegetallen waargenomen, van 2.7 tot 3.6. Een maximale waarde is nog niet vastgesteld. Het theoretische maximum van zes zou een kristalstructuur geven, wat een nucleatie bij extreem lage reactiviteit zou vereisen. Dit zal duidelijk nooit het geval zijn bij cluster–cluster aggregatie, omdat altijd holtes gevormd zullen worden door de vertakte structuren inherent aan het kansgebonden proces. De toegenomen dichtheid wordt tevens aangetoond door een afname in de gyratiestraal en de ontwikkeling van de radiale distributiefunctie van de gelstructuren, waar een grotere accumulatie van massa en grotere holtes te zien zijn. Dit bevestigt de

grotere toename van de correlatielengte tijdens reactie-gelimiteerde aggregatie, zoals vastgesteld bij de melk–yoghurt gelatie.

Het polarisatiesignaal van een SESANS meting wordt gevormd door de geprojecteerde correlatiefunctie en de sterkte wordt gegeven door de verstrooide fractie van de bundel. De kwaliteit van het signaal wordt bepaald door de invallende flux, de lineaire attenuatie coëfficiënt, de verstrooiingsdoorsnede en de dikte van het te meten materiaal. Een verband is afgeleid tussen de onzekerheid in de correlatiefunctie en de materiaaldikte. De optimale dikte geeft een minimale onzekerheid en hangt niet af van de inkomende flux, maar is een functie van verstrooiingsdoorsnede en attenuatie coëfficiënt. Voor materialen die zeer transparant zijn voor neutronen, is de onzekerheid minimaal rond een gemiddelde van 0.8 verstrooiingen per neutron. Zodra de attenuatie coëfficiënt binnen een order van grootte komt van de verstrooiingsdoorsnede, zakt het optimale aantal verstrooiingen naar 0.1. Zodra de attenuatie coëfficiënt tien of meer keer de verstrooiingsdoorsnede bedraagt, wordt dit de dominante factor die de kwaliteit van het signaal bepaalt. In materialen die zo relatief ondoorzichtig zijn voor neutronen, wordt de optimale dikte gegeven door de $1/\mathrm{e}$-lengte.

Words of gratitude

Many days spent preparing samples in laboratories, many weeks of carrying out experiments in experimental halls, months of debugging computer code and years of trying to make sense of it all; the common trajectory for a PhD on collision course with a doctorate. What remains is to write down the essentials as intelligibly as possible. I want to thank my wife Li Mei, my parents Mr. Fred van Heijkamp and Margriet van Heijkamp-Goenee, my sister Caroline van Heijkamp MSc and her partner Bas Gilissen BSc, and my friend Niels Geurts BSc and his brother Roel Geurts BA.

The research objective of this thesis was proposed by my supervisor dr. Wim Bouwman and my promoter prof. Ignatz de Schepper from the Neutron and Positron Methods in Materials (NPM^2) group. I want to thank them for giving me an opportunity to become acquainted with the field of neutron scattering and their guidance during the PhD project. Because of them, I have gained a lot of experience and developed a lot of skills, that will definitely prove useful in the future. Dr. Robert Andersson and dr. Jeroen Plomp from NPM^2 have been invaluable in helping me out as colleagues, as well as in being good friends. It has been a pleasure to work with Chris Duif MSc in NPM^2, who has helped me with many measurements and I have learned a lot about the SESANS setup from him. I also want to thank dr. Jouke Heringa from Fundamental Aspects of Materials and Energy (FAME) for all his help with the simulations and for the discussions about how to interpret the collected data. I am also grateful for the friendships with WingKee Chan MSc, Lucas Haverkate MSc, dr. Wouter Borghols, dr. Sarita Singh, Deepak Singh MSc, Zhiqiang Ou MSc, Nicole Banga, ing. Fred Naastenpad and ing. Michel Steenvoorden from FAME as well as Karoly Nagy MSc from Physics of Nuclear Reactors (PNR), who made work much more enjoyable. Dr. Diane Abou, Ana Sevcenco MSc and Ula Woroniecka from Radiation & Isotopes for Health (RIH) have helped me a lot. A special thanks must go to prof. Bert Wolterbeek and Astrid van der Meer for their hospitability and overall friendliness. Last but not least, Krishna Kowlgi MSc and dr. Ger Koper from DCT for the nice collaboration and all the pizza's.

Curriculum vitæ

Photo by Li Mei, 2007, Guangdong, China.

Léon F. van Heijkamp was born on the 10^{th} of November (♏) in 1976 in Amersfoort, near the geographical center of The Netherlands. He finished catholic primary school in 1989 and went to a protestant Gymnasium for a pre-university education in Amersfoort, which has the classical languages Latin and Greek in the curriculum. Despite his interest in languages, especially English, the exact sciences were more alluring. Sticking with only English and Latin, Léon focused on math, physics and chemistry and graduated in 1995.

Despite higher grades in math and physics, he found chemistry the most interesting and chose to study Chemical Engineering at the University of Twente, in the rural east of The Netherlands. After a first year of studying and a weekend library job, the subsequent years his social focus shifted to more cultural and social activities on the student campus, at the sports facilities and playing guitar. Léon became involved with pool, snooker and carambole billiards, playing competition and tournaments. After a merger between the university's snooker and carambole billiards associations and the addition of two pool tables, he made 'B.S.V. De Stoottroepen' his second home and served his club as Master of Treasury and as Chairman. In spite of enjoying life's finer things, science was not neglected. His interest shifted however from the applied chemistry of process engineering to the more fundamental aspects of nature.

An internship of four months in Sweden at Uppsala University, doing *ab initio* calculations on acetonitryl-water-ion complexes, made him develop a great interest in using computers to calculate and predict physical interactions and processes. Léon spent his master thesis project on Molecular Dynamics simulations of sheared, linear alkanes. This combination of physics and chemistry was continued when he started a PhD at the Delft University of Technology, dealing with neutron scattering and simulations on soft condensed matter, culminating in this thesis.

In this study non-invasive neutron scattering techniques are used on soft condensed matter, probing colloidal length scales. Neutrons penetrate deeply into matter and have a different interaction with hydrogen and deuterium, allowing for tunable contrast using light and heavy water as solvents. The mesoscopic structure of materials is determined by measuring the elastic scattering of neutrons over small angles. Spin-echo small angle neutron scattering (SESANS) and the reciprocal-space equivalent ultra small angle neutron scattering (USANS) have been used to investigate the structure of colloidal suspensions and gels by measuring the projections of the density-density correlation function and of the scattering function. A hollow sphere model is developed and used to investigate liposomes and *E. coli* bacteria. The sizes of liposomes and *E. coli* and their hollow sphere nature were confirmed. Particle size and size distribution have been measured for milk, and the change in typical length scale during gelation into yoghurt was measured kinetically.

3D Monte Carlo simulations of colloidal aggregation have been performed using a varying reactivity, ranging from reaction limited (RLCA) to diffusion limited cluster–cluster aggregation (DLCA), to study the effect on structure and formation. A comparison is made between simulated structures and SESANS measurements by calculating the density correlation function. A relaxation time is introduced into the simulated reactivity to control aggregation speed. The increase of typical sizes during gelation at low reactivity was consistently observed in measurements and simulations, but longest length scales could not be accurately simulated. A transition from RLCA to DLCA occurs if the typical reaction time is below typical monomer diffusion time. The increase in coordination number becomes larger when aggregation remains reaction limited.

The optimal sample thickness for a SESANS measurement is derived as a function of scattering cross-section and linear attenuation coefficient. The optimal sample thickness is at about 0.8 scattering events for neutron transparent samples, whereas it is the $1/\mathrm{e}$-length when samples are neutron opaque.